2012

Validation of 3'-deoxy-3'-[18F]-fluorothymidine positron emission tomography for image-guidance in biologically adaptive radiotherapy

Marian Axente
Virginia Commonwealth University

Validation of 3´-deoxy-3´-^{18}F-fluorothymidine positron emission tomography for image-guidance in biologically adaptive radiotherapy

A Dissertation submitted in partial fulfillment of the requirements for the degree of Doctor of Philosophy at Virginia Commonwealth University.

by

MARIAN AXENTE
Bachelor of Science in Physics,
University of Tennessee at Chattanooga, May 2007

Director: Andrei Pugachev
Assistant Professor, Department of Radiation Oncology, Medical Physics division,
Virginia Commonwealth University

Virginia Commonwealth University
Richmond, Virginia
May 2012

Acknowledgment

To my wife, my best friend, Betsy. Thank you for all your support, love, and patience.

Table of Contents

List of Figures

List of Abbreviations

For clarity, the abbreviations used throughout the text are provided here.

CT Computed Tomography

DNA deoxyribonucleic acid

FDG 2´-Deoxy-2´-^{18}F-fluoroglucose

FLT 3´-Deoxy-3´-^{18}F-fluorothymidine

FWHM Full width at half maximum

FWTM Full width at tenth maximum

MRI Magnetic Resonance Imaging

PET Positron Emission Tomography

TK1 thymidine kinase 1

SUV standard uptake value

DAR digital autoradiography

IFM immuno-fluorescent microscopy

BrdU bromodeoxyuridine

H&E Hematoxylin and eosin

ROC Receiver operating characteristic

AUC area under *ROC* curve

Abstract

VALIDATION OF 3´-DEOXY-3´-^{18}F-FLUOROTHYMIDINE POSITRON EMISSION TOMOGRAPHY FOR IMAGE-GUIDANCE IN BIOLOGICALLY ADAPTIVE RADIOTHERAPY

By Marian Axente

A Dissertation submitted in partial fulfillment of the requirements for the degree of Doctor of Philosophy at Virginia Commonwealth University.

Virginia Commonwealth University, 2012

Director: Andrei Pugachev
Assistant Professor, Department of Radiation Oncology, Medical Physics division, Virginia Commonwealth University

Accelerated tumor cell repopulation during radiation therapy is one of the leading causes for low survival rates of head-and-neck cancer patients. The therapeutic effectiveness of radiotherapy could be improved by selectively targeting proliferating

tumor subvolumes with higher doses of radiation. Positron emission tomography (PET) imaging with 3´-deoxy-3´-^{18}F-fluorothymidine (FLT) has shown great potential as a non-invasive approach to characterizing the proliferation status of tumors. This thesis focuses on histopathological validation of FLT PET imaging specifically for image-guidance applications in biologically adaptive radiotherapy. The lack of experimental data supporting the use of FLT PET imaging for radiotherapy guidance is addressed by developing a novel methodology for histopathological validation of PET imaging. Using this new approach, the spatial concordance between the intratumoral pattern of FLT uptake and the spatial distribution of cell proliferation is demonstrated in animal tumors. First, a two-dimensional analysis is conducted comparing the microscopic FLT uptake as imaged with autoradiography and the distribution of active cell proliferation markers imaged with immunofluorescent microscopy. It was observed that when tumors present a pattern of cell proliferation that is highly dispersed throughout the tumor, even high-resolution imaging modalities such as autoradiography could not accurately determine the extent and spatial distribution of proliferative tumor subvolumes. While microscopic spatial coincidence between high FLT uptake regions and actively proliferative subvolumes was demonstrated in tumors with highly compartmentalized/aggregated features of cell proliferation, there were no conclusive results across the entire set of utilized tumor specimens. This emphasized the need for addressing the limited resolution of FLT PET when imaging microscopic patterns of cell proliferation. This issue was emphasized in the second part of the thesis where the spatial concordance between volumes segmented on FLT simulated FLT PET images and the three dimensional spatial distribution of cell proliferation markers was analyzed.

1. Introduction

1.1 Biologically adaptive radiotherapy

According to the National Institute of Health, half of all cancer patients receive some type of radiation therapy during the course of their treatment. Radiotherapy is therefore standard care for many cancer patients. It uses different methods of delivering ionizing radiation to reduce the size or eradicate tumors. This is done by radiation induced tumor cell death, a complex biochemical process initialized by DNA damage produced during cell irradiation. However, all living cells are susceptible to radiation induced cell death. Therefore, the universal goal in radiotherapy is to maximize tumor cell kill while limiting the normal tissue irradiation and potential treatment-induced secondary effects. This can be partially achieved by utilizing complex spatial arrangements of radiation beams/sources that create optimal deliverable dose distributions, which focus the majority of the radiation dose in the tumor while sparing the normal tissue. However, the concept of “optimal” dose distributions is a paradigm that is continually evolving.

Solid tumors are characterized by highly complex microenvironments (Figure 1), which create spatially heterogeneous populations of tumor cells with varying sensitivity to ionizing radiation[1]. It has been observed that most disease recurrences in locally advanced cancers occur in regions of the tumor that are either poorly vascularized (hypoxic)[2, 3], or have a large fraction of actively proliferating cells[4-6]. Therefore, the radiation dose could be modulated such that the resulting optimal deliverable dose distribution would account for the spatially variable levels of radiosensitivity found within

a defined target[7, 8]. Computer simulation studies indicate that radiation treatments that are selectively targeting 'high-risk' tumor subvolumes with increased doses of radiation could potentially have better outcomes than treatments that deliver uniform doses to the entire tumor[9-12].

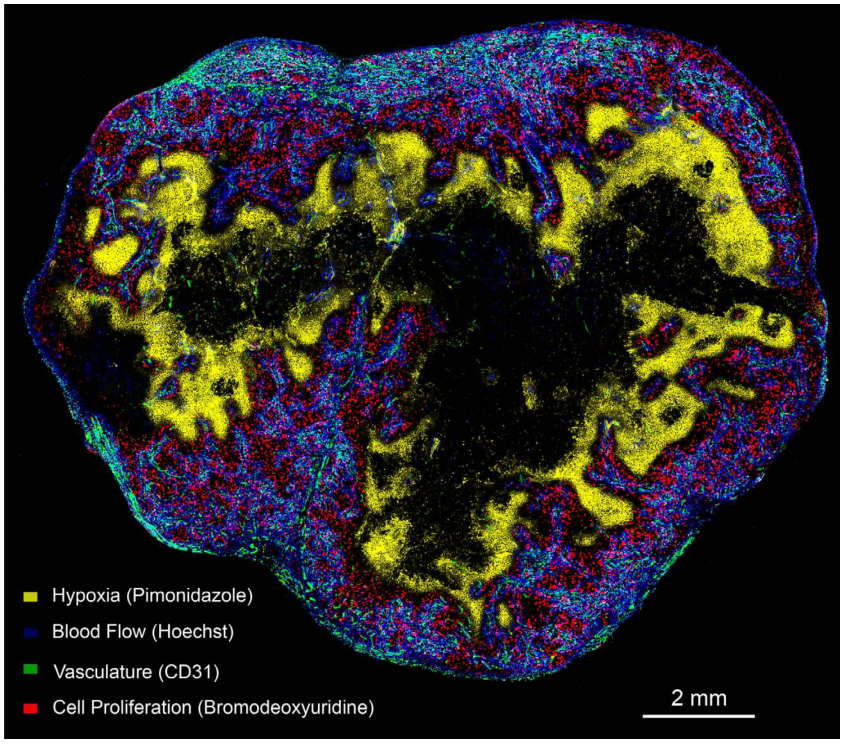

Figure 1. Overlaid immunofluorescence microscopy images from thin adjacent tissue sections (FaDu tumor xenograft), presenting different functional aspects of tumor microenvironment surrounding a necrotic core.

For selective dose escalation treatments to be efficacious, different tumor regions need to be accurately characterized in terms of aggressiveness and/or risk of recurrence based on local biological features, prior to the initiation of treatment. However, the majority of radiation treatments are currently planned based on x-ray computed tomography (CT) imaging studies (Figure 2A). Due to the physics of image acquisition, CT images cannot provide a detailed spatial description of the tumor content or heterogeneity, hence no pertinent information about the biological status of

different tumor subvolumes is used to plan radiation treatments. The current status quo in CT-based treatment planning is that tumors can be regarded as masses of identical cells uniformly distributed within a physician-defined target volume. Under this assumption, it was shown that the tumor control probability is correlated with the minimum dose delivered to the whole tumor[13], and that the maximum therapeutic ratio of a treatment can be achieved by maximizing the degree of uniformity in the dose distribution covering the target volume[14, 15]. After decades of clinical utilization, the uniform dose "optimal" distribution has become a powerful dogma in radiation oncology since it simplifies dose prescription and reporting, creating a robust approach to computing tumor control probabilities, and streamlining the accumulation of clinical data[16]. As a result, treatment planning with intentionally non-uniform dose distributions is not a common practice in conventional external beam radiotherapy, even if it may present better curative strategies[10, 12].

Until recently, clinical in vivo exploration of tumor biology has been limited to invasive techniques (e.g. image-guided biopsy). However, the developing field of molecular imaging enables non-invasive visualization of different functional or pathological aspects of tumor biology. Biomarker probes can be administered via systemic circulation. Their specific binding to tumor cells enables the visualization of tumor biology with high contrast using functional imaging modalities such as positron emission tomography (PET) among others (Figure 2B). This highly sensitive and quantitative imaging modality can provide the information necessary in establishing a direct correlation between pretreatment imaging parameters, the delivered dose distribution and treatment outcome[17]. Once specific tumor regions can be identified as

being at-risk of recurrence based on individual patient PET imaging data[18], the treatment can be customized, the clinical decision consisting in properly assigning dose to these tumor subvolumes for treatment delivery (Figure 2C). Currently, this remains a subjective issue, with physicians prescribing an empirical dose boost to high-risk tumor regions, based on clinical experience and/or patient population data[9, 19-21].

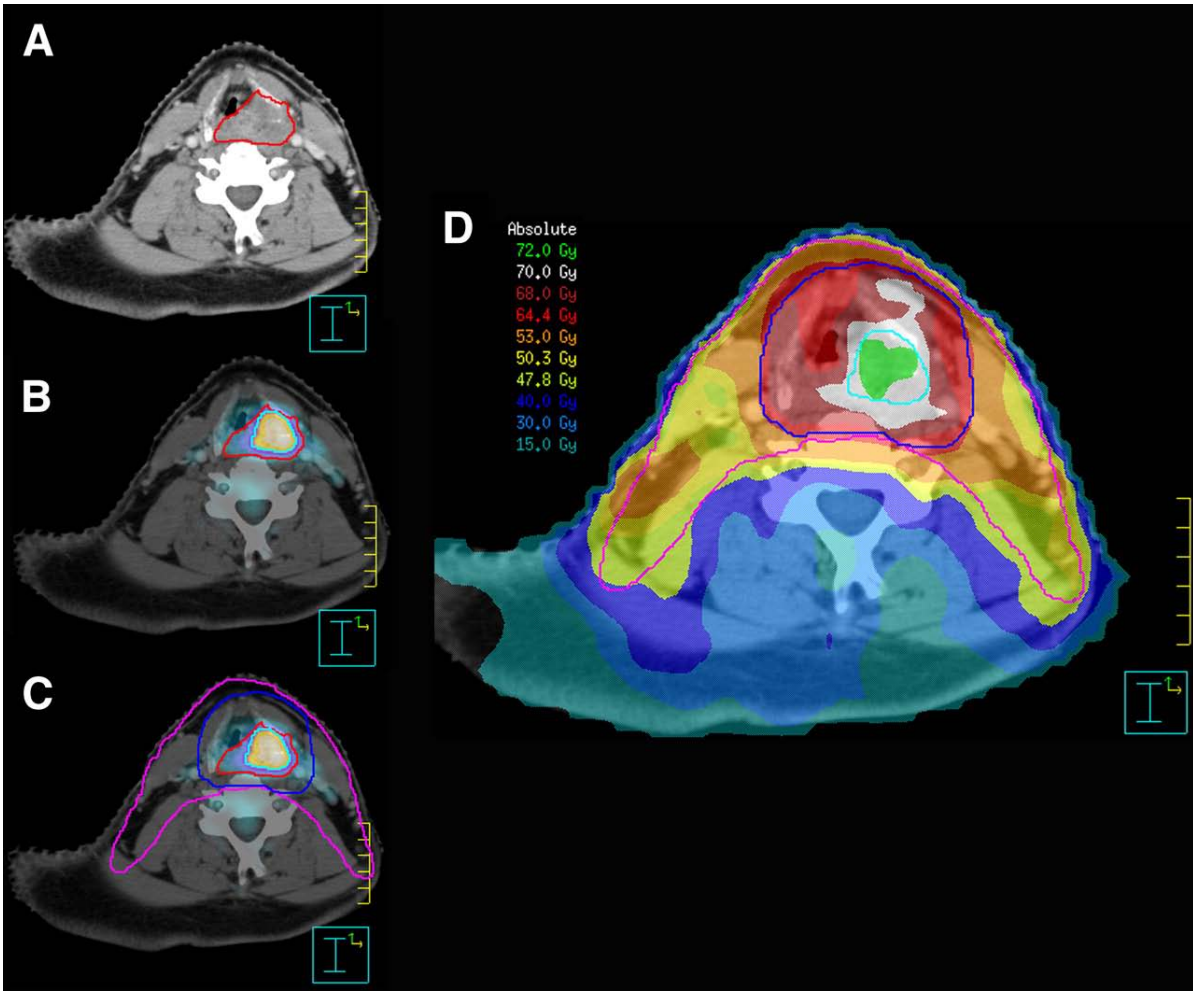

Figure 2. A. Planning CT with CT-delineated gross tumor volume. B. Fusion of planning CT and corresponding ^{18}F-FDG PET image with PET-delineated gross tumor volume. C. Planning contours of target volumes: pink – 50.3 Gy; blue – 68 Gy; light blue – 72 Gy. D. Overlaid calculated heterogeneous dose distribution targeting the PET-delineated gross tumor volume with higher doses. Figure replicated from Troost et al.[21]

The concept of biologically adaptive radiotherapy as understood in this work refers to external beam radiotherapy strategies where the delivered treatment is

customized based on individual patient biology, including but not limited to tailoring an optimal dose distribution that accounts for radioresistant tumor subvolumes identified by functional imaging (specifically PET imaging). While many of the validation steps involved in the clinical implementation of biologically adaptive radiotherapy are yet to be taken, many clinical trials have been developed in order to make this type of individualized therapy available to cancer patients[20, 22]. As research in this particular aspect of radiotherapy is very active, one concept remains unchanged. In biologically adaptive radiotherapy using PET imaging, the spatial pattern of the tracer uptake observed in PET images will be utilized to derive inhomogeneous dose distributions delivering higher doses to regions with high tracer uptake. This strategy is based on the hypothesis that planning PET images are accurate spatial representations of the underlying targeted biology.

In biologically adaptive radiotherapy using PET imaging, the spatial pattern of tracer uptake recorded in PET images will be utilized to derive inhomogeneous dose distributions delivering higher doses to regions with high tracer uptake.

1.2 Head and neck cancer: biology and radiation therapy

Head and neck cancer patients include those who have tumor growths in the nasal cavity, sinuses, lips, mouth, salivary glands, throat, or larynx. Most head and neck cancer patients are diagnosed in advanced stages[23]. Because of that, aggressive

treatments including radiation therapy fail to improve the 20-50% five-year survival rate[24, 25]. In a multicenter randomized trial comparing radiotherapy with concomitant radio-chemotherapy for advanced-stage oropharynx carcinoma, Denis et al. have observed that only 16% of patients receiving radiotherapy alone survived 5 years or more, added chemotherapy slightly improving survival (22%)[25]. The introduction and technological advancement of intensity-modulated radiotherapy (IMRT) have significantly improved treatment conformity for head and neck patients, increasing normal tissue sparing and concomitantly raising the patient quality of life post-treatment[26]. In the cited study, the patients in the IMRT arm presented with better salivary function of the parotid glands. Only 44% of the patients were diagnosed with grade 2 or worse xerostomia when compared with 76% of the patients that received conventional radiotherapy[26]. However, to date, IMRT has not improved survival of advanced head and neck cancer patients. A need for dose escalation was emphasized by the fact that most treatment failures are local, occurring within the treated volume. For example in a study by Studer et al. 45 out of 46 patients (16% of patient population) that presented with local failures at two years the recurrence was inside the treatment field[27].

Accelerated repopulation of tumor cells during radiotherapy is defined either based on direct measurement of doubling time of clonogenic cells obtained from biopsy specimens or indirectly by recording the extra dose necessary to control 50% of tumors when prolonged treatments are utilized. Many classic studies have established that the rate of cell proliferation in untreated solid tumors decreases with increasing distance from sources of nutrients and oxygen. As cells proximal to vessels are killed by

radiotherapy, the levels of nutrients and oxygen available of remaining cells are significantly improved. This activates cell proliferation in previously quiescent cancerous cells, increasing the fraction of cells that are repopulating the tumor mass. Furthermore, it has been proposed that tumor cells that are differentiating during radiotherapy have a higher probability of retaining clonogenic status than cells that differentiate in normal conditions, and their rate of proliferation may be faster with fewer aborted cell divisions. Furthermore, the radiation cellular damage has been shown to activate proliferation mechanisms in human squamous cell carcinoma[134]. The treatment failures in head and neck cancers seem to be associated with accelerated repopulation of tumor cells during radiotherapy[5, 28-30]. Uniform dose escalation trials have shown promising results regarding tumor control, but also an increase of severe toxicities associated with irradiation of organs in close proximity of the head and neck tumors (oral mucosa, parotid glands, etc.)[31, 32]. Furthermore, the incidence of treatment-associated toxicity greatly depends on the volume of irradiated normal tissue[26, 33]. In terms of biologically adaptive radiotherapy, the effectiveness of the treatments can be increased at the same time while limiting toxicities associated with escalating the radiation doses to the entire tumor volume[30, 34-38], by delivering escalated doses only to higher-risk tumor subvolumes characterized by active cell proliferation. No dose-escalation trials have been conducted utilizing FLT PET to guide the delivered dose distributions. However, FDG-based trials have shown the feasibility of such an approach[20].

By delivering inhomogeneous dose distributions targeting actively proliferating tumor subvolumes with increased doses, the therapeutic ratio of IMRT for head-and-neck patients could be significantly increased.

1.3 Fluorothymidine – imaging cell proliferation in head and neck cancer

Multiple non-invasive imaging methods have been proposed for in vivo imaging of cell proliferation including magnetic resonance imaging (MRI) spectroscopy[39], and PET utilizing tracers that are incorporated into DNA: [^{11}C-methyl] thymidine, 1-(2'-Deoxy-2'-[^{18}F]-fluoro-1-β-D-arabinofuranosyl)-thymine, 1-(2'-Deoxy-2'-[^{18}F]-fluoro-1-β-D-arabinofuranosyl-uracyl)-bromouracil, and tracers that are indirectly related to cell proliferation. One of these latter, 3´-Deoxy-3´-[^{18}F]-fluorothymidine (FLT). PET with ^{18}F labeled FLT has proved to be the most promising imaging modality for identifying proliferative areas of the tumors[40].

FLT is currently produced only for research purposes and is under investigation for clinical implementation as a PET tracer for cell proliferation[41]. FLT is a synthetic thymidine analog (Figure 3). Extensive validation efforts have been devoted to determining the biological mechanism of FLT specific uptake in proliferating cells. Currently it is assumed that FLT uptake in solid tumors is determined by the enzymatic activity of thymidine kinase 1 (TK1), a cytosolic enzyme, with high phosphorylating activity during the DNA synthetic phase of the cell cycle[42].

Once incorporated in the cell, FLT can serve as substrate for TK1. Thymidine phosphorylation is the first step in the thymidine salvage pathway for DNA synthesis.

While thymidine phosphates are incorporated in DNA, FLT phosphates are not due to a missing hydroxyl group in their structure (Figure 3). Therefore, FLT phosphates remain trapped intracellularly[43], providing specific high uptake in cells where TK1 is upregulated[44, 45], such as actively proliferating tumor cells.

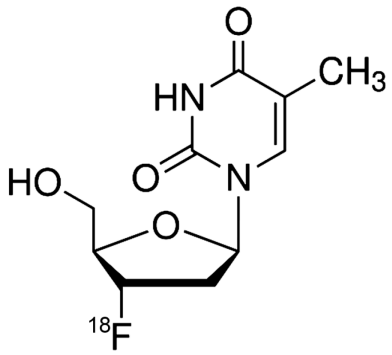

Figure 3. 3′-Deoxy-3′-^{18}F-fluorothymidine chemical structure. The only difference from the pyrimidinic nucleotide is the ^{18}F isotope replacing a hydroxyl group at the 3´ position on the ribose ring.

However, recent studies involving correlation of in vivo FLT uptake values (static and dynamic PET imaging) and TK1 expression/activity assays in patients, provided no direct evidence of the stated hypothesis about TK1 phosphorylation being the rate-limiting step in FLT accumulation[46, 47]. New evidence suggests that the FLT uptake mechanism is a complex interplay between membrane nucleoside transporters expression and activity[48-50], competitive binding of nucleoside transporters between FLT and endogenous thymidine[51-53], and relative metabolic equilibrium between FLT influx/efflux and activity of TK1 and enzymes that dephosphorylate FLT[43, 54]. Nevertheless, ex vivo assays of cell proliferation obtained from surgical resection tumor specimens (e.g. Ki-67 labeling index) correlate with in vivo tumor uptake of FLT in a

wide variety of human tumors, empirically confirming FLT as a tracer of cell proliferation[46, 47, 55, 56].

Currently under investigation, FLT is a promising tracer for non-invasive imaging of cancer cell proliferation and could be used to identify the location and extent of tumor subvolumes that are actively proliferating.

1.4 Current status of validation efforts

Validation of any biomarker assay requires demonstration that the performance of the assay is suitable and reliable for the intended analytical application[57]. As mentioned in section 1.1, in biologically adaptive radiotherapy, the spatial pattern of tracer uptake identified on PET determines the inhomogeneous dose distribution giving higher doses to tumor regions with high risk of recurrence of disease. Therefore, by demonstrating the spatial concordance between the pattern of FLT uptake and the intratumoral distribution of cell proliferation, FLT PET images can be safely and effectively used to identify and delineate tumor subvolumes characterized by active cell proliferation to be used in biologically adaptive radiotherapy. Validating spatial concordance between the FLT uptake pattern and the distribution of actively proliferating cells is equivalent to demonstrating that the tumor regions that contain tumor cells that are actively proliferating are the same tumor regions which present higher tracer uptake on FLT PET images (or autoradiography images).

Currently, FLT PET imaging is being proposed for utilization mainly for diagnostic purposes[38]. Specifically, its suggested uses include indication of early treatment response[35, 56, 58, 59], and prediction of long-term treatment response to radiotherapy[60, 61]. In these diagnostic applications of PET imaging in oncology, PET data is used to extract metrics such as average, and/or maximum standard uptake values (SUV), that allow to test for the presence of the disease or to predict certain characteristics of the tumor as a whole. Validation of such PET imaging applications is currently conducted by establishing correlations between single-value SUV-based metrics characterizing in vivo PET tracer uptake and ex vivo pathological indices representative of the target biology (e.g. proliferation index) over a population of patients[46, 54, 55, 62-64]. Since these studies utilize single-value metrics, no spatial information about the pattern of FLT uptake is retained in the analysis. Therefore, the spatial co-localization between the heterogeneous PET tracer uptake and that of biological markers of cell proliferation is not demonstrated. Up to date, there are no published data verifying the spatial concordance between intratumoral distribution of FLT uptake and the pattern of tumor cell proliferation.

There is no validation data demonstrating the spatial coincidence between areas of high uptake FLT in PET images and regions of intratumoral active cell proliferation.

1.5 Study goal

FLT was described as a novel PET tracer specifically designed to non-invasively image active cell proliferation. Its specific high uptake in proliferating cells has been demonstrated in vitro, but up to date there is no study validating that areas of high in vivo FLT uptake are spatially co-localized with areas of active proliferation in individual tumor specimens. In proposed scenarios where FLT PET would be used in biologically adaptive radiotherapy for image-guidance, validation of spatial concordance with cell proliferation is necessary. Many factors can affect the in vivo intratumoral uptake of FLT. For example, the irregularities of tumor vascular system and its structural deficiencies[65-67] can potentially modulate the levels of FLT uptake by limiting the regional supply of the tracer to individual cells. Furthermore, by analyzing PET imaging from first principles, it is well known that there are inherent limitations to the size of the smallest object that this imaging modality can accurately resolve[68-71]. Tumor microenvironment presents a spatially heterogeneous distribution of viable and necrotic tissue, well-oxygenated and hypoxic regions, proliferative and non-proliferative subvolumes. The variation of these biological spatial characteristics spans distances that are usually smaller than current inherent resolution of clinical PET scanners (Figure 4). When using PET imaging to guide the delivery of radiotherapy, inherent averaging effects can significantly alter the resulting images, making it necessary to demonstrate the spatial coincidence between the pattern of tracer uptake as seen in PET images and the pattern of the underlying biological parameter of interest. Specifically, this type of analysis of can provide important information about the clinical situations where PET

imaging provide enough spatial information about the underlying targeted biology, and how can this information may be safely and efficaciously used for treatment planning for head and neck patients.

The research work presented herein is an attempt to address a major gap in the data supporting FLT PET imaging for the specific task of radiation therapy target volume definition, by establishing a methodology for in vivo validation of FLT PET for indentifying the extent and spatial distribution of cancer cell proliferation. This proposed study will also provide the first available sets of experimental data demonstrating the spatial co-localization of the intratumoral distribution of FLT uptake and cell proliferation markers.

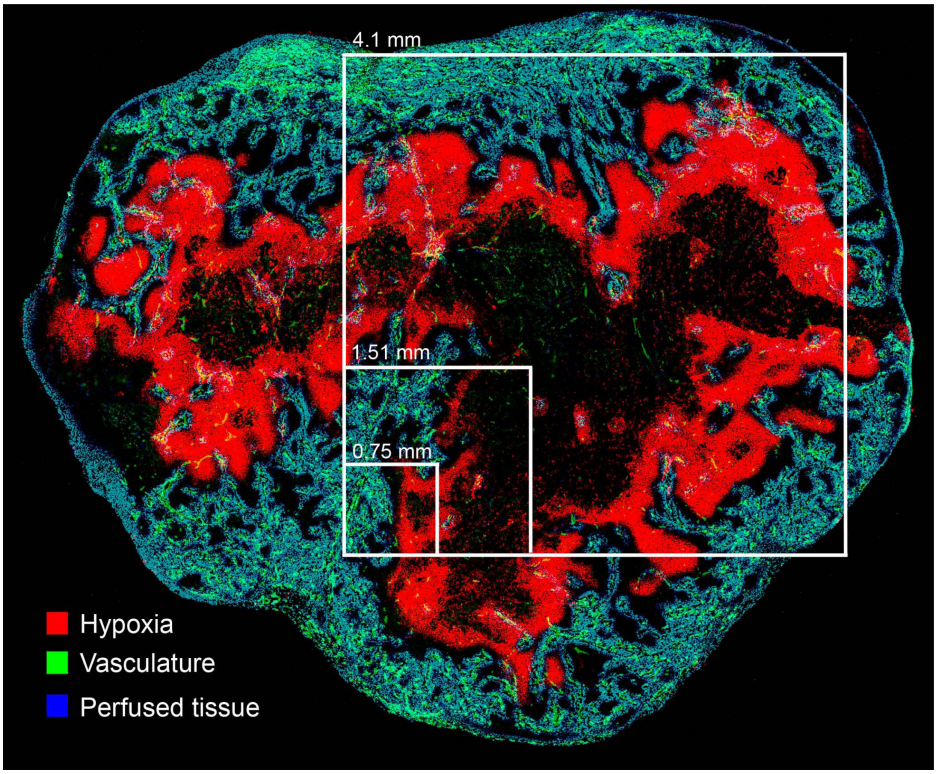

Figure 4. Immunofluorescence microscopy image of tumor microenvironment. Squares are representative of different PET resolution: submillimiter resolution (750 μm) for small aperture preclinical systems; 1.5 mm resolution of current preclinical system Siemens Inveon; 4.1 mm resolution of current time-of-flight clinical system Siemens Biograph mCT.

1.7 Research questions

The registration of in vivo PET images with histological samples has been shown to necessitate a technically complex methodology[72, 73], that still does not always provide the accuracy needed for analysis between in vivo PET images and ex vivo pathological images[69, 74, 75]. An alternative way to evaluate the concordance between the PET tracer intratumoral distribution and that of its intended target is to use thin tissue sections obtained from a surgically excised whole tumor specimen from a patient or an animal injected with the tracer before the surgery.

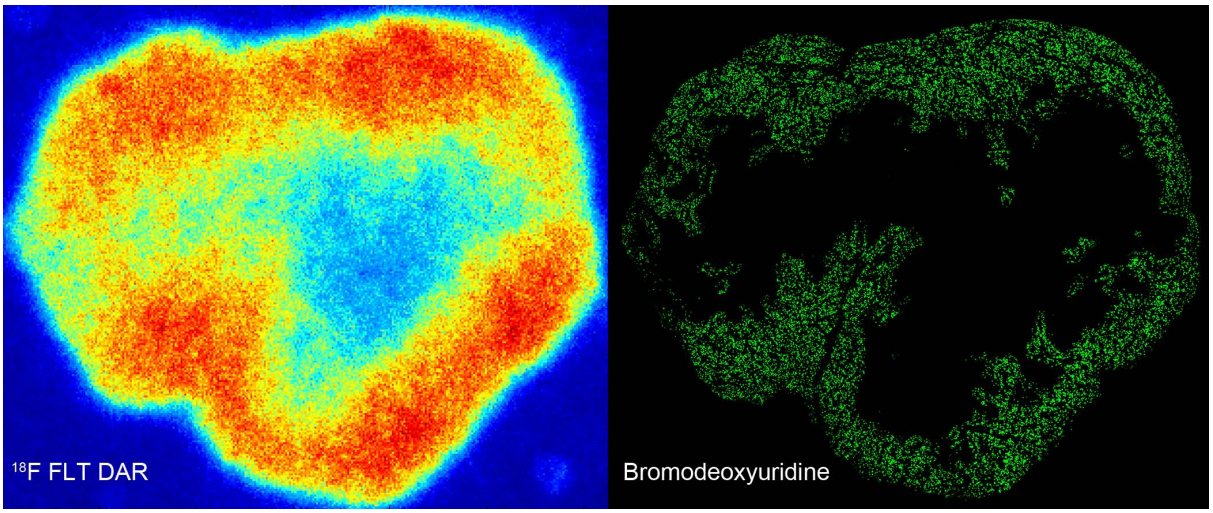

Figure 5. Comparison between spatial pattern of intratumoral uptake of FLT (DAR image, left) and spatial distribution of cell proliferation markers (uptake of bromodeoxyuridine on IFM image, right). Images were obtained from adjacent tissue sections.

Using these tissue sections, it is possible to visualize the two-dimensional microscopic distribution of the PET tracer distribution using digital autoradiography (DAR) and the spatial distribution of relevant biological markers using immuno-fluorescent microscopy (IFM). These high-resolution imaging modalities are described in detail in Chapter 2. By co-registering these data and performing statistical analysis, it

is possible to evaluate how well the PET tracer distribution depicts the spatial pattern of the tracer's intended biological target (Figure 5).

This direct spatial comparison was utilized throughout this thesis with two specific goals. First, to demonstrate that at a microscopic level, there is spatial concordance between the intratumoral FLT pattern of uptake and the spatial distribution of cell proliferation markers. Confirming this spatial coincidence is an important clinical goal of the study, since it provides direct evidence that the tracer specifically targets actively proliferating cells in vivo.

Specific Aim #1

Analyze the spatial concordance between the intratumoral pattern of FLT uptake and the spatial distribution of cell proliferation markers at a microscopic level

In order to realize the potential of FLT PET for image-guidance in biologically adaptive radiotherapy, it is necessary to analyze the spatial coincidence between the regions of interest contoured from macroscopic FLT PET images and underlying tumor subvolumes, segmented from microscopic cell proliferation images. Therefore, the second aim of this thesis involved developing and demonstrating utilization for a set of validation tools that will eventually enable comparing FLT PET synthetic images obtained from stacked DAR images, to the three-dimensional spatial distribution of cell proliferation markers. This was done as to observe the effects that the limited resolution

of PET induces on the FLT images' ability to determine the spatial extent and spatial distribution of proliferative tumor subvolumes.

Specific Aim #2

Develop histopathologic validation tools for spatial concordance analysis between volumes segmented on FLT simulated PET images and the three dimensional spatial distribution of cell proliferation markers

1.8 Summary of thesis

Specific aim #1 is covered in chapters 2 and 3. Chapter 2 describes the basic experimental methods utilized throughout the study involving tumor models, tissue processing, tumor microenvironment imaging and image processing techniques. More important, this chapter introduces a co-registration workflow that was developed for aligning DAR and IFM images throughout the projects presented in this thesis. The utilized image registration tools and an evaluation of the registration error were presented in detail. In chapter 3, a novel spatial concordance analysis methodology is introduced. Spatial concordance between intratumoral FLT uptake pattern and cell proliferation at a microscopic level are presented and discussed.

Specific aim #2 is covered in chapters 4 and 5. A method to create synthetic PET images from DAR images is presented in chapter 4. Chapter 5 presents a methodology for spatial concordance analysis between simulated FLT PET images and images of

tumor cell proliferation. A limited set of results are presented for head-and-neck tumor xenograft synthetic PET images as an illustration of the method.

The conclusions of the thesis are presented in chapter 6.

2. Comprehensive approach to co-registration of autoradiography and microscopy images acquired from a set of sequential tissue sections

2.1 Introduction

Using thin tissue sections from tumor specimens that were injected with various tracers, it is possible to visualize the two-dimensional microscopic distribution of the PET tracer distribution using digital autoradiography (DAR) and the spatial distribution of relevant biological markers using immuno-fluorescent microscopy (IFM). Comparison between these imaging sets is an often-utilized validation method showing that the investigated PET tracer specifically binds a targeted biological molecule/pathway.

Autoradiography is a two-dimensional imaging modality that records the pattern of interactions of charged particles (or photons) emitted during decay of a distribution of radioactive sources. In the case of DAR, phosphor plates are the detection and recording medium. DAR images of the distribution of radiotracer within a thin tissue sample (Figure 5), is an example of “in vivo autoradiography” because the tracer was administered and allowed to diffuse and bind while the animal was still alive. DAR is a highly sensitive imaging modality, with a wide dynamic range (5 orders of magnitude), and presents a linear response to the activity concentration present in a sample. Furthermore, the tissue sample is in close proximity with the imaging plate (<20 μm). This is of particular importance since this study uses *β*-particle autoradiography. Energetic *β* decay particles present non-negligible ranges before interaction with the detectors. By minimizing the tissue section thickness and the distance between tissue and detecting media, the DAR setup ensures that the image captured by the imaging

plate is a high-resolution representation of the radiotracer uptake distribution in that particular tissue section.

Immuno-fluorescence microscopy is a light microscopy technique that utilizes a fluorescent microscope to visualize the distribution of specific target molecules within a biological sample (Figure 5). Specific fluorescent antibodies are used to the tumor-specific molecules/biological pathways that are investigated. By stimulating the fluorescent tags of the bound antibodies, a fluorescent signal is obtained and recorded by high-resolution digital cameras. The spatial distribution of the recorded specific markers is representative of the distribution of the targeted molecule or pathway in that particular tissue section. In this study, IFM images are utilized to obtain the spatial distribution of specified cell proliferation markers, among other functional aspects of the tumor microenvironment.

As mentioned in the previous chapter, the first specific aim of the thesis is to evaluate the spatial concordance between the FLT PET tracer intratumoral distribution and the spatial distribution of cell proliferation markers at a microscopic level. Before any statistical analysis is conducted, it is important to minimize the geometrical misalignments between the two images obtained from different modalities, which can introduce unaccounted confounding effects.

To ensure the most accurate analysis results, all images (acquired through DAR and IFM techniques) should be acquired from a single tissue section. Most often, this is not feasible due to different technical aspects of the image acquisition process. Consequently, several studies investigating the co-localization of a PET tracer with its biological target used a set of sequential tissue sections to perform DAR and

immunohistochemical staining/imaging to reveal multiple aspects of the tumor biology[76-78]. Therefore, beyond the difficulties of registering data from different imaging modalities, such data acquisition methods pose the additional challenge of co-registration of all the images acquired from different, albeit adjacent tissue sections. Even though the tissue sections used are thin enough (several microns) to insure minimum variation of the microenvironmental parameters of interest between adjacent sections, tissue cutting, mounting on glass slides and chemical processing can introduce non-linear deformations that prevent precise co-registration of the images acquired from adjacent tissue sections by only using rigid affine transformations (those allowing only translation, rotation, and scaling) . When DAR images are part of the image dataset, objective co-registration of the images becomes even more difficult, as the information content in DAR images is drastically different from microscopy images. For this reason, the standard of manual affine co-registration of DAR with IFM images tends to be highly subjective, when based on the tissue outline.

The purpose of the study presented here is to develop and evaluate a methodology for objective co-registration of histopathological and DAR images acquired from a set of sequential thin tumor tissue sections. The details of this study have been previously published in the Journal of Nuclear Medicine[79].

2.2 Experimental methods

Animals and tumor models

Human cancer cells were used to establish tumor xenografts in male athymic mice (NCr-nu/nu, National Cancer Institute), by bilateral flank subcutaneous inoculation

of 5×10^5 cells/site. This technique of heterotransplantation of human cancer cells into immunodeficient rodents is a widely accepted protocol for development of preclinical tumor models representative of the molecular characteristics of given human cancers. Head and neck squamous cancer cells were used: a human hypopharyngeal cancer line (FaDu) was utilized for four animals, and a laryngeal cancer line with an activating mutation for EGFR (SQ-20B) was utilized for another four animals. Tumor growth was assessed by caliper measurements and recorded every other day. Animal maintenance and all experimental procedures were carried out according to the protocol approved by the local Institutional Animal Care and Use Committee at Virginia Commonwealth University.

Radiotracers

For this study, autoradiography was utilized to reveal the intratumoral distribution ^{18}F-FLT PET tracer. ^{18}F-FLT was produced by the Center of Molecular Imaging, Virginia Commonwealth University (Richmond, VA). The synthesis followed an established protocol, utilizing 5´-benzoyl-2,3´-anhydrothymidine as a precursor[80, 81]. ^{14}C-FDG (American Radiolabeled Chemicals, Inc.) was also injected to evaluate the difference in the intratumoral distribution between FLT and FDG for a different study.

Tumor tissue collection

When the tumors reached 10-15 mm in diameter, the animals were anesthetized by inhalation of a mixture of oxygen and Isofluorane. At 80 minutes before planned animal euthanasia a bolus injection containing pimonidazole hydrochloride

(Hypoxyprobe, HPI, Inc., Burlington, MA) 2.5 mg/20 g mouse, Hoechst 33342 (Sigma-Aldrich, St. Louis, MO) 0.4 mg/20 g mouse, 37 MBq ^{18}F-FLT, and 185 kBq of ^{14}C-FDG, was administered by tail-vein injection, followed by two consecutive intraperitoneal injections of bromodeoxyuridine (Sigma-Aldrich) 15 mg/20g mouse, at 50 and at 30 minutes before the animal sacrifice. After animal sacrifice, tumors were immediately excised, embedded in Tissue-Tek OCT (Sakura Finetek), and frozen on dry ice. The tumor specimens were sectioned with a Leica CM1850 UV cryostat (Leica Microsystems) at 8 μm thickness. From each tumor, three stacks of at least 15 consecutive sections were obtained from the top, the middle, and the bottom of the tumor specimen (≥45 sections per tumor). Each section was affixed onto a glass slide for staining and visualization.

Autoradiography

One section (referred to as reference section below) was selected from each stack of consecutive sections and used for phosphor plate autoradiography. On these reference sections, registration marker dots were manually placed on the glass slide around the tissue section, utilizing a mixture of 1 μl ^{14}C ink (Moravek Biochemicals), 50 μg Hoechst, and all-purpose glue. The slides selected for DAR imaging were covered with a layer of saran wrap to avoid contamination of the imaging plates with long-lived radionuclide and exposed to phosphor plate for 4 hr. All exposures were conducted at room temperature. ^{14}C standards (American Radiolabeled Chemicals, Inc.) were simultaneously exposed with the tissue sections. The imaging plate was read with Fujifilm BAS-5000 Bio-Imaging Analyzer to obtain the image of ^{18}F-FLT distribution.

After the first exposure, ^{18}F activity was allowed to decay for 1 day. Thereafter, a 4-day exposure was initiated, as to obtain the image of distribution for the ^{14}C-FDG tracer. In the last step, another 4 hr exposure was performed to confirm the insignificant contribution of ^{14}C-FDG activity to the ^{18}F-FLT image. The resulting images were exported in TIFF format, at 25 μm/pixel resolution and 16-bit depth. The DAR images of individual tumor sections (Figure 6 A-B) were cropped from a large image of the whole phosphor plate containing multiple sections. The typical size of individual tissue section image was on average 500 by 600 pixels, at 25 μm/pixel. The DAR images were digitized and image intensity values were converted to actual activity (Bq/mm^2). Prior to registration, these individual tumor section DAR images were up-sampled to 2.5 μm/pixel using nearest-neighbor interpolation, preserving the original intensity values. For ^{18}F DAR, a scaling factor was experimentally derived to calibrate the image of the 4-hour exposure to activity concentration (Bq/mm^2), based on the ^{14}C standards.

Tumor microenvironment imaging

In order to visualize different aspects of the tumor biology, such as cell proliferation, hypoxia, blood flow patterns, a combination of previously described immunohistochemical techniques were used[77, 82-84]. All types of acquired IFM images are presented in Figure 6. For imaging of cell proliferation, two different staining techniques were used, tracking proliferation from different perspectives. First, the distribution of bromodeoxyuridine (BrdU) was investigated. The intratumoral uptake of BrdU, revealed the density of dividing cells (in DNA synthetic phase of mitotic cycle) in the investigated tissue sample. Since BrdU was injected before animal sacrifice, it was distributed via

systemic circulation to the tumor tissue, and was made available to the cells through the same pathways as the radiotracers. Therefore, BrdU was considered an exogenous marker of cell proliferation. The second marker of cell proliferation was the endogenous Ki-67 protein, upregulated in proliferating cells[85]. As Ki-67 is absent in quiescent cells (G_0 phase), it can provide an estimate of the density of actively cycling cells[86]. Furthermore, the correlation between anti-BrdU and anti-Ki-67 labeling indices was found to be statistically significant[87].

Pimonidazole hydrochloride was used as a marker of hypoxia. Hoechst 33342 (Sigma-Aldrich) was utilized to track the tumor blood flow and diffusion, as this fluorescent dye is transported through the tumor's vasculature and preferentially binds to nuclear regions rich in A-T base pairs in its diffusion path. DAPI (Sigma-Aldrich) is a DNA specific fluorescent probe, specifically binding to nuclear regions rich in A-T base pairs. This stain is applied after slide preparation, and it is aimed at revealing all nuclear material present in the investigated tissue sample. Therefore, the resulting staining distribution is indicative of the extent of the viable tissue on the respective tumor section. Furthermore, the distribution of viable tissue vs. necrosis is verified by obtaining Meyer's hematoxylin and eosin (H&E) stain on an adjacent section. The microenvironmental map is completed by the distribution of the vasculature. For this purpose, the CD31 endothelial marker was utilized, a surface protein found on endothelial cells of blood vessels, also known as platelet endothelial adhesion molecule or PECAM-1. The immunofluorescent histochemical processing of the tissue sections was automated utilizing the Ventana Discovery XT system (Ventana Medical Systems, Inc., Tucson, AZ). H&E staining was performed manually.

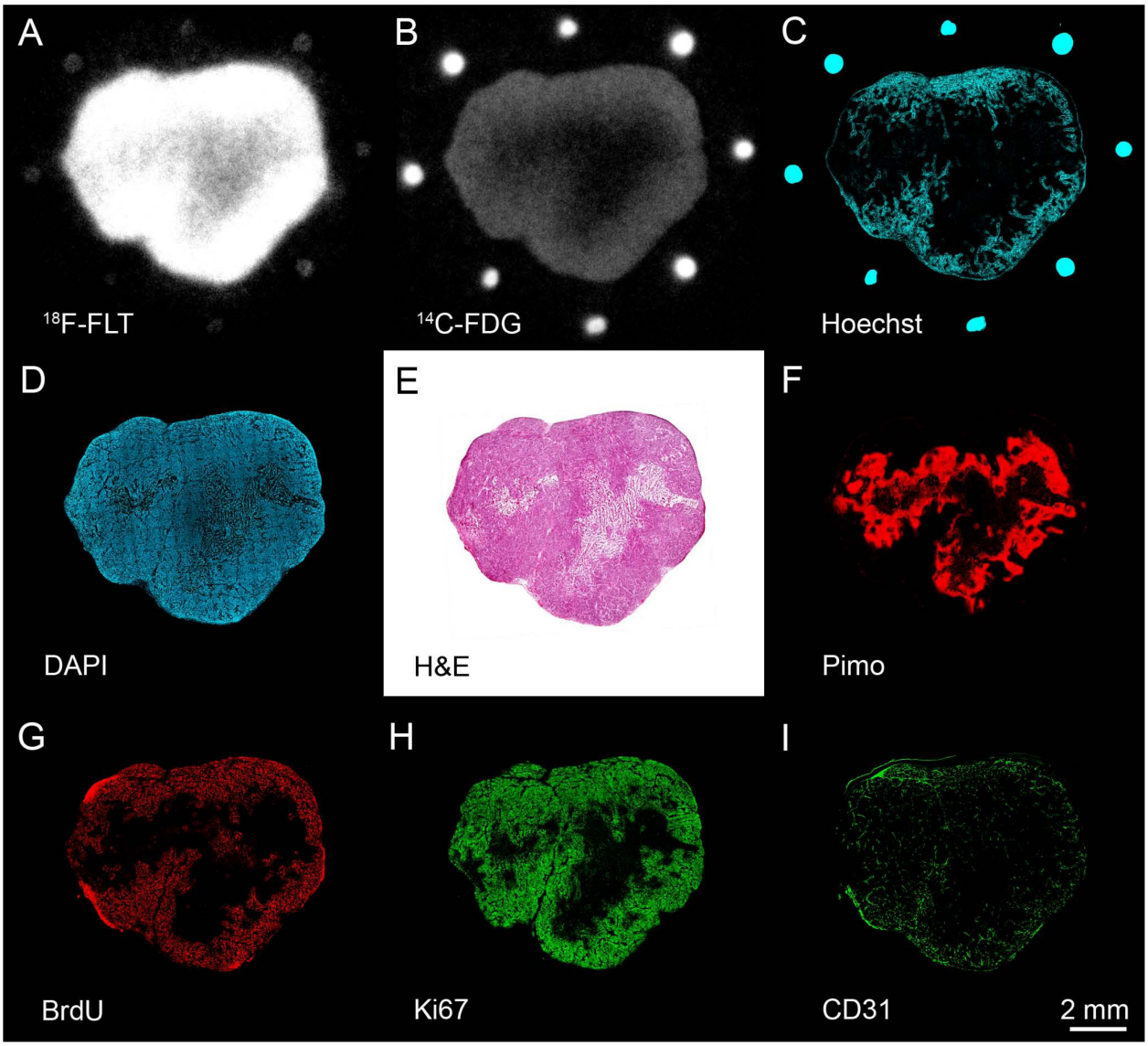

Figure 6. Complete coregistered image dataset for one stack of sequential tissue sections of a FaDu xenograft tumor.

Because of the long exposure times necessary for autoradiography and because of the contact with the plastic film that can damage the tissue upon removal, the tissue sections used for DAR were deemed unsuitable for any further immunohistochemical processing. Therefore, the strategy depicted in Figure 7 was adopted: obtain DAR from the reference section and microenvironment information from adjacent sections. All

microscopy images were acquired at 20X magnification using a motorized research Olympus BX61 microscope, connected to X-Cite 120PC fluorescence illumination system for IFM imaging, and an Applied Imaging SL50 automatic microscope slide loader. The automated tiled image acquisition and reconstruction process was controlled through the Ariol software (Genetix, San Jose, CA). All images were acquired at 8-bit depth and had a 2.5 μm pixel size. The typical physical size of the image was on average 5000 by 6000 pixels, varying with the extent of the tumor tissue.

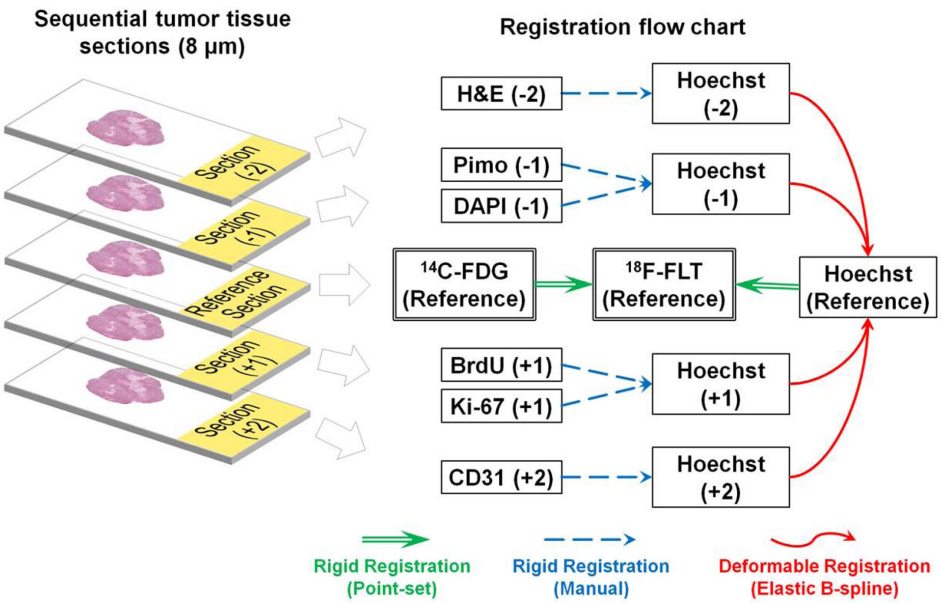

Figure 7. Image acquisition and registration scheme. Green double arrows represent rigid point-set registration used for the autoradiography and Hoechst images from the reference section. Blue dashed arrows represent manual rigid registration of microscopy images from non-reference sections. Red solid arrows correspond to Hoechst-based deformable registration.

2.3 Image registration methods and validation

A two-step registration approach was used as depicted in Figure 7. For each individual tissue section used for data acquisition, all images obtained from this section

were initially rigidly co-registered. Thereafter, these independent sets of rigidly registered images representing individual tissue sections were registered together using deformable registration.

Rigid Image Registration – Images Acquired from the Same Section

For the microscopy images obtained from the same tumor section, the adjustments needed for registration were minor, as all tissue deformations induced during section cutting and mounting would affect all of these images in the same way. Misalignments could only be induced by the automated slide placement on the microscope tray and, potentially, tissue shrinkage during subsequent immunohistochemical processing.

To correct for these misalignments, manual rigid registration of these images was performed in Photoshop CS4 Extended (Adobe), based on aligning tissue boundaries (always visible due to the tissue auto-fluorescence or non-specific binding). Automated image content-based registration was avoided since the microscopy images obtained from the same tissue section represented radically different characteristics and features.

Registration of DAR with IFM images poses a different problem, as the former are characterized by lower resolution and lack microscopic landmarks useful for co-registration and verification. Therefore, for the autoradiography and the Hoechst image acquired from the reference tissue section a different registration method was used. Instead of relying on the tissue outlines, a set of regular landmarks was created by placing 8-12 dots of ^{14}C ink mixed with Hoechst dye, around the tissue section on the

glass slide. These dots (with the typical diameter of ~0.2 - 0.5 mm) were visible on both autoradiography and Hoechst images (Figure 6 A-C).

For each marker dot, a weighted center of mass was obtained for the autoradiography and microscopy images. Using at least six marker dots (selected interactively), the rigid transformation needed to align the centers of mass of these dots in the Hoechst image with those in the autoradiogram was obtained. The rigid transform of the point coordinates was calculated using a MATLAB R2010a (MathWorks) implementation of coherent point drift (CPD) algorithm[88]. The algorithm is available for free download for research use at: https://sites.google.com/site/myronenko/research/cpd. The resulting transformed image intensity values were calculated using linear interpolation.

The coherent point drift algorithm is a probabilistic point set registration algorithm, where the alignment of two distinct point sets is solved as a probability density estimation problem. Specifically, the primary (stationary) point set is one of the data sets, while the other point set (moving) is represented as the locations of the centroids of a Gaussian mixture model. A mixture model is a probabilistic model utilized to characterize the existence of sub-populations within an overall population, without requiring a apriori identification of the sub-population to which an individual observation belongs[89]. A Gaussian mixture model is a parametric mixture model represented as a weighted sum of Gaussian component probability densities. The Gaussian mixture model of the moving point set is fit to the primary data in an iterative fashion by maximizing the likelihood (expectation-maximization algorithm). The specific characteristic of this algorithm is that, for every iteration, the Gaussian mixture model

centroids are forced to move coherently as a group, which preserves the topological structure of the moving data set. The coherent point drift algorithm is accurate and robust in case of missing data, initialization, and presence of noise. No specific correspondences need to be defined between the point data sets[88].

Deformable Image Registration – Images Acquired From Multiple Sections

As previously reported in histopathological image registration studies[90, 91], tissue cutting and slide preparation induce in each collected tissue section characteristic non-linear deformations (tissue stretching, warping, etc.). Thus, deformable image registration is needed to correctly align the images obtained from adjacent or spatially proximate tissue sections.

As represented schematically in Figure 7, Hoechst IFM images were obtained from all tumor sections. The typical diffusion distance of Hoechst in tissue is approximately 100-250 μm[84], significantly larger than the tissue section thickness (8 μm). Therefore, it was assumed that the majority of the Hoechst image features observed in a set of consecutive tumor tissue sections are spatially constant, as illustrated in Figure 8.

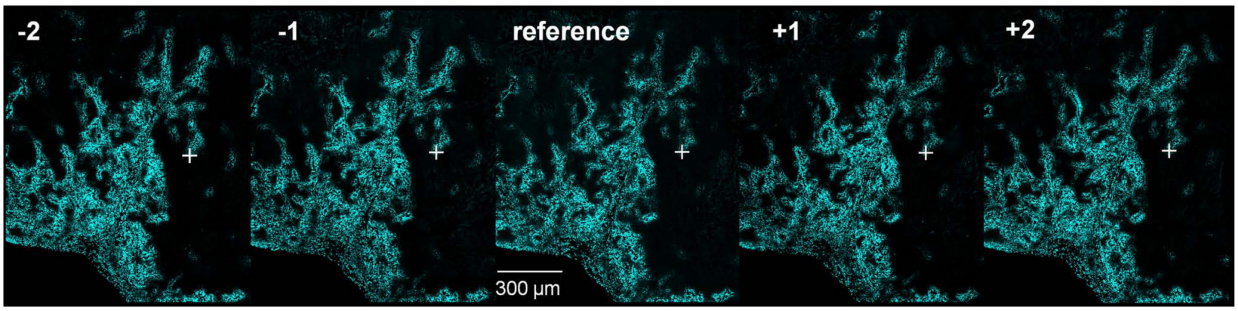

Figure 8. Fragments of Hoechst images acquired from five consecutive sections showing corresponding landmark indicated with the white cross.

Correspondingly, this spatial correspondence of Hoechst staining features can be used to establish the deformations needed to register Hoechst images acquired from non-reference sections to the Hoechst image of the reference section.

To perform deformable registration of Hoechst images acquired from sequential tissue sections, the open source Java-based Fiji plugin bundle (implemented in the NIH ImageJ platform) was utilized. The Hoechst images were first rigidly registered employing the Register Virtual Stack Slices plugin. For the reference Hoechst image (acquired from the section used for autoradiography acquisition) and each of the non-reference Hoechst images (representing adjacent tissue sections), a set of corresponding invariant features distributed through the area of the section was identified using the Feature Extraction plugin employing a multi-scale oriented patch feature extraction algorithm[92]. Using these features as soft registration landmarks, a deformable image registration plugin, UnwarpJ, was employed[93]. This elastic registration algorithm was specifically designed to handle the alignment of biological images. The deformation field was expressed as a B-spline model. The registered image smoothness was ensured by way of vector-spline regularization. The registration field was estimated each time through the minimization of a three parameter objective function containing a data term (the mean squared error between images), the error in mapping corresponding landmarks (soft constrain), and a regularization term.

The derived deformable transformation was then applied to the Hoechst image for which it was calculated, and to all other images obtained from that particular tumor section. By repeating this procedure for the rest of non-reference tissue sections, all the microscopy images obtained from a stack of sequential tissue sections were registered

to the Hoechst image of the reference section. As the latter was also registered to the ^{18}F-FLT and ^{14}C-FDG autoradiography images, all microscopy and autoradiography images were registered together by the combination of rigid and deformable registration techniques as shown in the flow chart presented in Figure 7, and had a resulting pixel size of 2.5 μm.

Image Registration Error Analysis

Rigid Registration – Images Acquired From the Same Section

The minor misalignments between the microscopy images coming from the same image were resolved by manual registration as described above. Preliminary tests utilizing difference images have indicated that visual inspection of the overlap was a sensitive method to detect misregistrations. Misalignments as small as one pixel size could be detected without difficulty. Therefore, the registration error of this alignment process was considered to be under the observable limit of one pixel (2.5 μm), thus negligible.

The accuracy of the microscopy to autoradiography image rigid registration that was evaluated using the marker dots created around each tumor section. Specifically, for each image pair, the total number of marker dots visible around the tissue was randomly split into a registration landmark set and a measurement landmark set. The rigid transformation was obtained based on the optimal alignment of the registration set, which always contained only four points, while the rest of the landmarks served as a measurement point set[94]. To evaluate the rigid registration error, the displacements between the weighted centers of mass of corresponding points in the measurement

point set were recorded after registration, for all of the utilized sets of images (8 tumor models). Multiple repetitions of the registration procedure (n=30) were performed for each tumor model, each time using different subsets of landmarks for registration and for measurement. Mean registration error and the standard deviation were calculated and reported for all the measurements (N = 960).

Deformable Registration – Images Acquired From Multiple Sections

To evaluate the registration accuracy of the deformable registration for the images acquired from adjacent tissue sections, sets of corresponding landmarks were established for the Hoechst image pairs to be registered (measurement landmark sets)[95]. To ensure objective evaluation, these landmarks had to be different from those utilized for the registration. Therefore, a different feature extraction algorithm, SIFT (Scale Invariant Feature Transform), was used to establish corresponding points in the two images[96]. To obtain a set of measurement landmarks to be used for registration accuracy evaluation, these initial sets of points were manually processed as to assure proper correspondence between the landmarks, and also their uniform distribution across the section area. For each of the eight tumor models, there were 3-5 different pairs of Hoechst images. For each Hoechst non-reference and Hoechst reference image pair, a minimum of 30 corresponding landmarks were defined.

To obtain the registration error distribution after deformable registration of the Hoechst image pairs, the distances between corresponding measurement landmarks in the target image and the registered image were recorded. The average distance between the landmarks after deformable registration was reported as the deformable

registration error. In order to calculate a combined registration error, it was assumed that the observed displacement values between corresponding points after image registration were random and normally distributed over all measurements. The total registration error was represented by its two components: rigid registration error (autoradiography to microscopy from the same tissue section) and deformable registration error (for microscopy images acquired from sequential tissue sections). The total registration error was defined as the convolution of the two error components approximated by Gaussian distributions.

2.4 Results

The initial step in the presented co-registration procedure was the rigid registration of DAR and IFM images obtained from the reference section. Figure 9 shows image overlays representative of the point-set rigid registration results. Following the same procedure, the ^{14}C-FDG autoradiography and Hoechst images were registered to the ^{18}F-FLT autoradiography.

The distribution of rigid registration error measurements is shown in Figure 10A. The average registration error for the rigid registration of Hoechst microscopy image to ^{18}F-FLT autoradiography image was $E_{\text{rigid,Hoechst}}$ = 30.8 μm ± 20.1 μm image registration. The mode of the distribution was 16.1 μm, while the maximum displacement value was 129.1 μm. The distribution of displacement values for ^{14}C-FDG to ^{18}F-FLT autoradiography image indicated an average registration error of $E_{\text{rigid,autorad}}$ = 26.4 μm ± 17.9 μm. The mode of the distribution was 9.01 μm with a maximum displacement value of 107.4 μm.

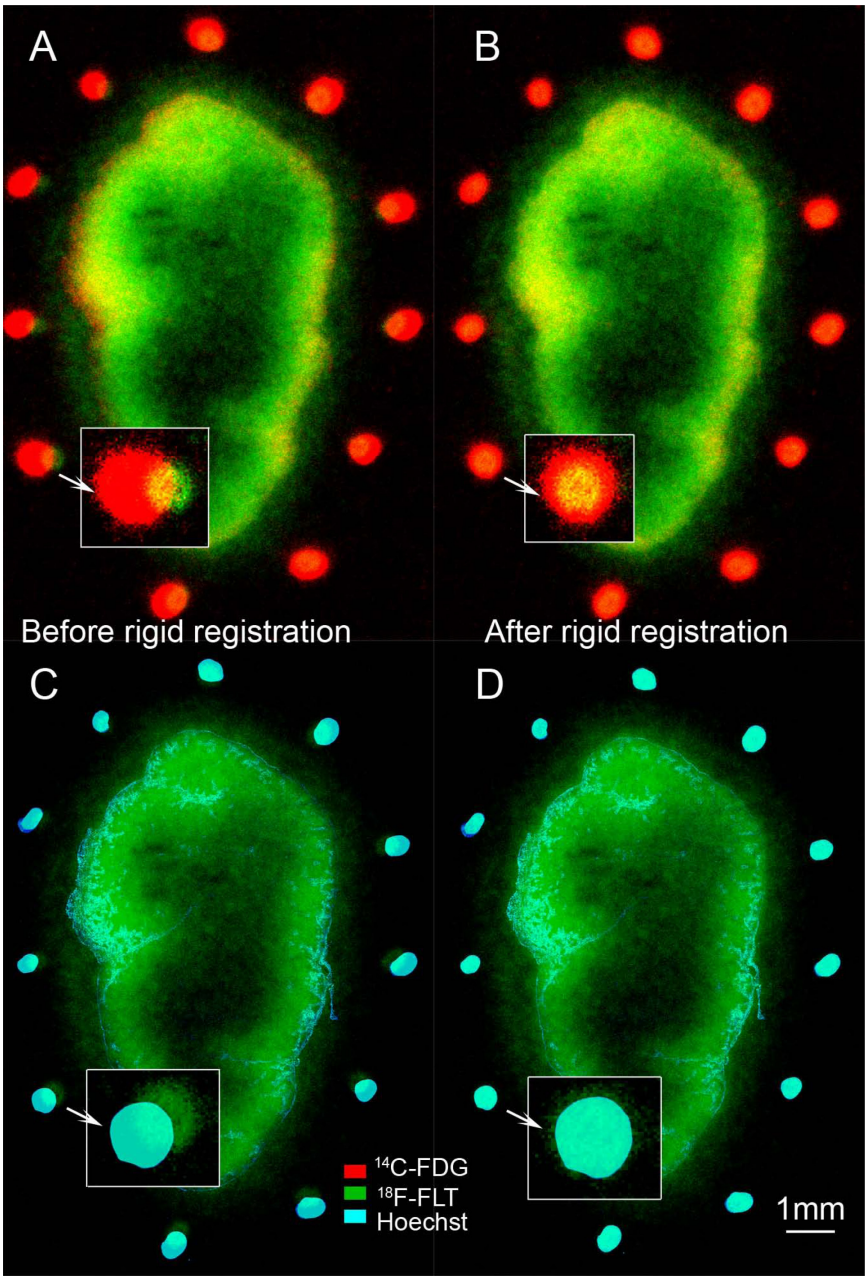

Figure 9. Transparent overlay in false colors of ^{14}C-FDG autoradiography (red), ^{18}F-FLT autoradiography (green), Hoechst (light blue). Panels A and C show images manually registered based on the observed tissue outline. Panels B and D present the same images after rigid point-set registration.

The distribution of deformable registration error measurements is shown in Figure 10B. These registration errors were calculated for 3-5 different pairs of Hoechst images for each of the eight tumor models. The success rate of the deformable registration algorithm was uniform across the utilized tumor models (average error

ranges from 19.73 to 25.66 μm). For each Hoechst non-reference and Hoechst reference image pair, we had a minimum 30 defined corresponding landmarks, for a total of 1057 measurements.

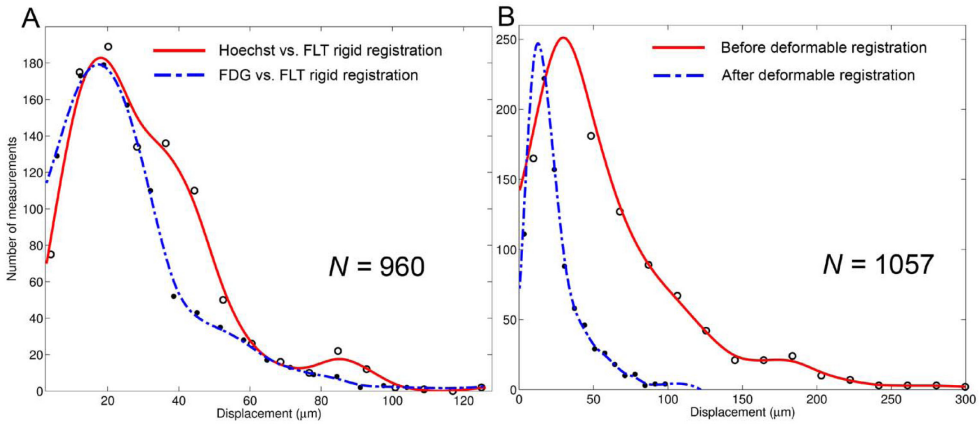

Figure 10. (A) Distribution of displacement values between corresponding landmarks after rigid point-set image registration (Hoechst image registered to ^{18}F-FLT autoradiogram and ^{14}C-FDG autoradiogram registered to ^{18}F-FLT autoradiogram); (B) Distribution of displacement values between corresponding landmarks: before deformable image registration (red dotted line), after deformable image registration (blue continuous line).

Figure 11 presents transparent overlays of images before and after the deformable registration procedure. Specifically, the top row demonstrate the effect of applying the calculated transformation for Hoechst images, while the bottom row reveals the overlay of two complementary aspects of the tumor biology (hypoxia and blood flow), before and after the deformable registration procedure.

The calculated error of the deformable registration was $E_{\text{deformable}}$ = 23.1 μm ± 17.9 μm, which is similar to that reported in three-dimensional tissue reconstruction studies utilizing the same deformable registration algorithm[95]. The distributions of the registration errors before deformable registration (red dashed line, maximum error 308.3 μm) and after (blue line, maximum error 108.4 μm) are shown in Figure 11B.

The total registration error was calculated as the convolution of the two error components: $\sigma_{total} = \sqrt{\sigma_{rigid}^2 + \sigma_{deformable}^2} = 44.86\ \mu m$.

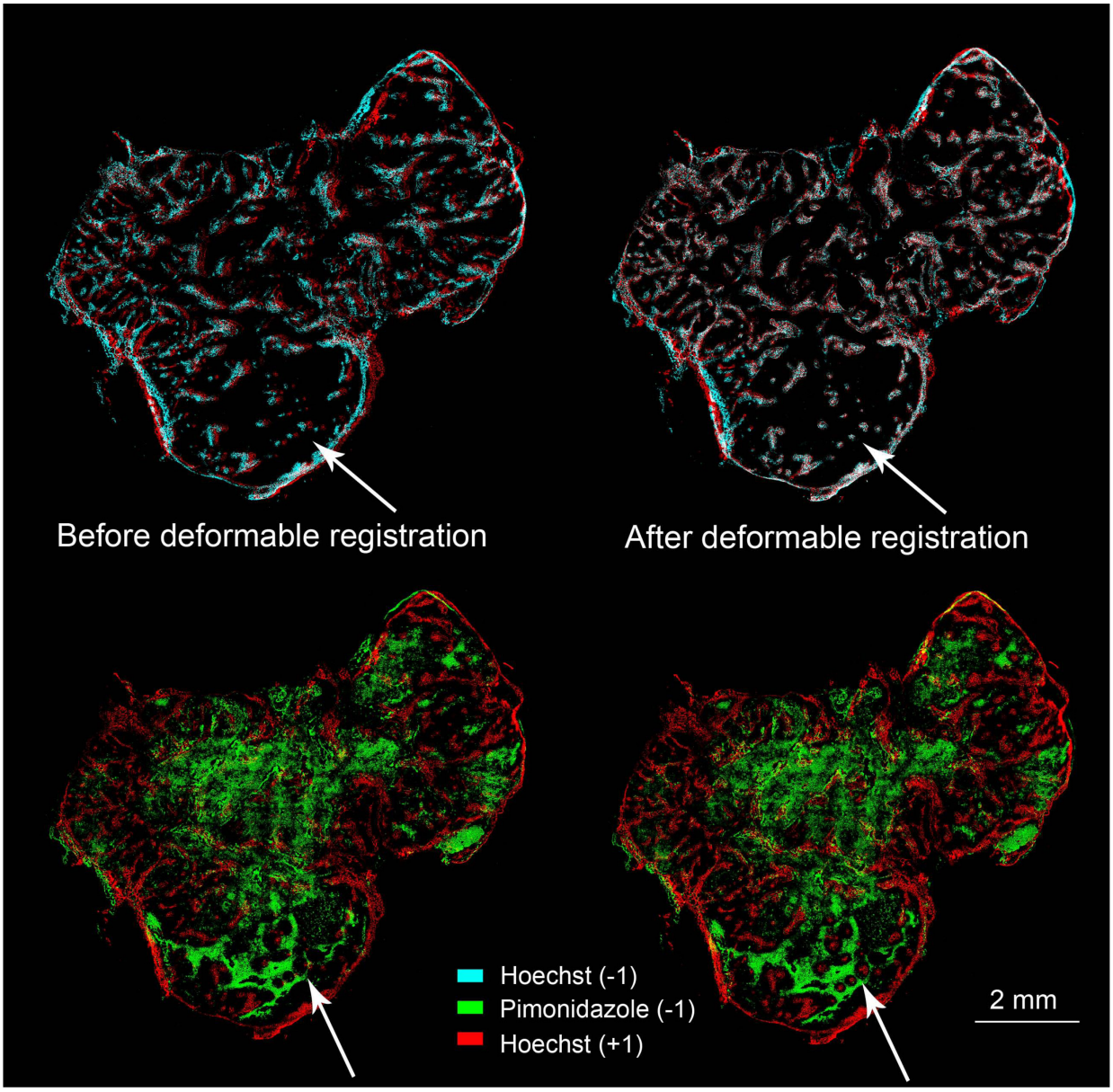

Figure 11. Illustration of deformable registration results using IFM images in semi-transparent overlay. Arrows indicate an area highlighting how initial misalignment was corrected by deformable registration.

2.5 Discussion

The aim of this study was to develop and evaluate a semi-automated approach to multi-modality registration of autoradiography and microscopy images acquired from sequential tissue sections. While this procedure was developed specifically for histopathological validation of PET tracers, it can be used as a tool for any co-localization studies involving various imaging probes, especially when the images of the probe distributions cannot be obtained from a single tissue section.

Earlier studies registering autoradiography and microscopy images utilized manual co-registration, to the observer's best ability. Rigid transforms (translation, rotation, scaling) were applied to images in transparent overlay, followed by convolution with a 200 μm Gaussian kernel to minimize the effect of any remaining misalignment errors, and/or rebinning, where the images were resampled to 200×200 μm grid for pixel-by-pixel analysis[76, 77]. Others have implemented automated rigid registration algorithms, followed by image rebinning to 200×200 μm pixel size to account for the estimated accuracy of image co-registration[78]. While these approaches are considered acceptable, manual registration of images from different modalities even when acquired from a single tissue section may be prone to observer bias and lack in reproducibility[97]. Lower resolution of autoradiography images combined with the background noise can obscure the edges of the tissue sections enough to hinder the manual registration relying on aligning tumor section outlines (Figure 9A, C). Furthermore, rebinning the data to the coarser pixel size with or without blurring can result in a significant loss of information as tumor microenvironment can change significantly on the scale of 200 μm[70, 98, 99]. Image intensity-based registration was also successfully employed using

cross-correlation, mutual information, and minimization of image dissimilarity[97, 100]. Nevertheless, inter-modality image registration cannot rely on image content, as to avoid alignment of regions that have similar content but are not co-localized. Landmark-based registration remains the most objective registration method for multi-modality imaging[73].

To allow for objective three-dimensional registration of in vivo images obtained with MRI and PET, and ex vivo histology and autoradiography images, Humm et al. introduced the stereotactic system employing Teflon fiduciary markers driven into the tumor[73]. Similar to the approach of Humm et al, the present study adopted the principle of creating landmarks visible on all registered images, i.e. autoradiography and microscopy images. However, invasive fiducials were not used in this study, to avoid tumor microenvironment disruption and interference with uptake of the PET tracer[101].

The most direct way to compare the intratumoral distribution of a PET tracer to designated biological aspects on tumor section images would be to obtain all pertinent information from a single representative tissue section. Because this is practically unfeasible most of the time, the images of PET tracer distribution were obtained from one tissue section, while the adjacent sections were utilized to acquire microscopy images to complete the microenvironmental map of the tumor. The novelty of the proposed approach is the use of Hoechst image-based registration, where the features of two Hoechst images acquired from the adjacent tissue sections were used to establish spatial correspondence between these two tissue sections and then obtain the deformation needed to co-register all images acquired from these sections. As a result, even though the images were acquired from adjacent sections, the misregistrations

caused by inevitable deformations that occur during tissue processing were minimized. An additional novel aspect of the co-registration methodology presented here is the elimination of manual registration of images obtained from different tissue sections, or from different modalities. In this study, we have demonstrated the feasibility of the proposed registration procedure and evaluated its accuracy.

The combined registration error of microscopy images to ^{18}F-FLT autoradiography images was 44.86 μm. This registration error is smaller than values previously reported between 100-200 μm in studies using the same general imaging modalities[76-78, 99]. Furthermore, since the registration error is smaller than the inherent resolution of ^{18}F or ^{14}C autoradiography, further studies analyzing the co-localization between radiotracers and targeted biological pathways will be minimally influenced by image registration.

Some aspects of our methodology need discussion. The typical size of the marker dots placed around tissue section using mixture of fluorescent marker (Hoechst 33342) and the ^{14}C ink was about 0.2-0.5 mm. This is similar or larger than the typical size of the structures (microenvironment features) seen in the images. However, it is not the marker dots but rather their weighted centers of mass that were used for registration of autoradiography and microscopy images. Therefore, the actual size of the marker dots was not limiting the accuracy of registration. However, while the autoradiography images are characterized by linear response and wide dynamic range (16-bit), fluorescent Hoechst images do not have the same dynamic ranges. Because the point-set registration is based on aligning the weighted centroids of the masked marker dots, the mentioned difference in dynamic range may potentially induce inaccuracies in

center of mass calculation. However, in the study presented here this issue was mitigated by creating marker dots as close to circular features as possible. We have conducted preliminary tests using a uniform mixture of fluorescent marker and the ^{14}C ink to confirm that the weighted centers of mass calculated for both autoradiography and microscopy images coincide in the majority of cases.

In the deformable registration of distinct Hoechst images, the definition of corresponding landmarks between two images can be inaccurate. Since the landmarks locations are only used as soft constraints in the registration algorithm, this uncertainty does not affect the final registration accuracy. However, during the deformable registration error evaluation, the uncertainty in landmark localization contributes to the final reported registration error. To minimize this effect, the final measurement point sets defined for each Hoechst image pair were manually processed and any observed inconsistencies eliminated by manual removal of the corresponding landmarks.

Finally, the study presented here has been conducted using small animal tumor model specimens. However, the methodology can also be applied at the clinical stages of PET tracer validation to confirm concordance between the pattern of PET tracer uptake and the spatial distribution of its intended target in patient tumor specimens.

In conclusion, a comprehensive, semi-automated method for deformable co-registration of autoradiography and microscopy images acquired from sequential tissue sections was developed and evaluated. The registration method addresses significant non-linear deformations induced by tissue processing, and eliminates the need for potentially subjective manual co-registration of multimodality images acquired from adjacent sections. We demonstrated that this method is more accurate than the other

currently available methods. The improvement in registration accuracy could further advance correlative studies of the microenvironmental factors governing PET tracer intratumoral distribution. Furthermore, it can aid the studies aimed at investigation of spatial co-localization of different aspects of tumor biology that can be revealed by combination of autoradiography and/or microscopy imaging.

3. Analysis of spatial concordance between the intratumoral patterns of cell proliferation and ^{18}F-fluorothymidine uptake at microenvironmental level

3.1 Introduction

Using ex vivo imaging of tumor tissue sections, it is possible to obtain images of the intratumoral distribution of PET tracer and compare them to images of specific molecular markers indicative of the targeted biological pathway. Establishing spatial concordance between these two images provides the experimental confirmation that the spatial pattern of the intratumoral PET tracer distribution correctly represents the spatial pattern of the underlying targeted biological features. This analysis can be conducted utilizing many different approaches. We present one way, specifically addressing the issue of spatial coincidence between segmentation areas defined based on FLT autoradiography and positive staining areas defined on proliferation microscopy images. In the first chapter of this thesis, the details of multi-modality co-registration between DAR and IFM images were presented. Utilizing this co-registration workflow, the geometric misalignments between images of FLT tracer and cell proliferation marker uptake were minimized, allowing for an accurate spatial concordance analysis.

Previous histopathological validation studies that sought to demonstrate the co-localization between intratumoral PET tracer uptake and tumor microenvironmental markers used thin tissue autoradiography and microscopy to image the tumor microenvironment. The resulting images were co-registered and pixel-by-pixel intensity correlation analysis was employed to obtain global indicators of spatial co-localization

(e.g. Pearson coefficient) between the grayscale intensities in the image-pairs[76-78]. However, this type of analysis is sensitive to many factors that could significantly influence the results. Depending on the ratio of the size of the pixels and the inherent resolution of ^{18}F autoradiography[70, 102, 103], local spatial autocorrelation between adjacent autoradiography pixels may occur, invalidating the Pearson correlation assumption of independence between individual pixel values. In addition, the Pearson correlation coefficient is highly sensitive to the presence of noise and non-specific staining/uptake in both considered images (autoradiography and microscopy)[104]. Furthermore, while phosphor plate autoradiography is characterized by linear response over a wide range of signal intensities, the response of the immune-histochemical microscopic imaging is generally non-linear. Therefore, the Pearson correlation coefficient, which tests the strength of a linear functional relationship between the pixel intensities of two co-registered images, may not be the optimal way to measure the spatial co-localization of these two signals.

Threshold-based analysis of spatial co-localization of two image sets provides an alternative and more intuitive approach to demonstrating the spatial concordance between the microscopic pattern of ^{18}F-FLT tracer uptake and the pattern of cell proliferation in images from thin tissue specimens. Since the images sets are accurately co-registered, overlap analysis metrics such as the Dice coefficient and analysis of receiver operating characteristic (*ROC*) curves can be used to directly assess the co-localization of the two signals.

By its definition, a threshold value differentiates between two mutually exclusive target groups within a given population. Therefore, when a threshold is applied to a FLT

uptake image, the result is a binary map containing positive pixels – representative of an area where there should be active cell proliferation, and negative pixels – where there should not be any proliferating tumor cells. This is a classic example of a dichotomous classification problem, widely encountered in computer-aided diagnostic systems[105]. When the classification is conducted with a priori knowledge of where the actively proliferating tumor regions are, then a contingency table or confusion matrix can be determined (Figure 12).

		Gold standard: pixel containing active cell proliferation?	
		YES	NO
Classification output: pixel containing active cell proliferation?	YES	True positive	False positive
	NO	False negative	True negative

Figure 12. Example of contingency table utilized in the dichotomous classification problems presented in this study. The gold standard is defined based on histopathological images of cell proliferation. The classification output is based on the FLT uptake image intensity chosen as a threshold value.

The performance of the classification system, in this case FLT thresholding, can be analyzed using measures for a specific threshold value[105]. For each selected FLT uptake threshold value, the true positive fraction corresponds to the portion of correctly classified pixels containing active cell proliferation. Correspondingly, the true negative fraction represents the portion of the pixel "population" which was correctly classified as

not containing actively proliferating cells. The false positive fraction represents the group of incorrectly classified pixels as containing active cell proliferating, and the false negative fraction, that part of the pixels that were incorrectly classified as not containing cell proliferation.

Since FLT thresholding is not an ideal classification tool for identifying the spatial distribution of cell proliferation, providing representative threshold-based classification performance metrics for single threshold values does not provide a representative indication of the overall performance of the classification method. In many medical applications, *ROC* curves are determined by plotting the true positive fraction (sensitivity) against the true negative fraction (specificity)[106], for all possible threshold values. The calculated area under the *ROC* curve has been used as an estimate of how well the investigated classification method performed, independently of the threshold value.

The Dice coefficient has been used as a similarity measure over pairs of given sets obtained from image segmentation[69, 107, 108]. It can be directly calculated based on the threshold-based metrics defined in the contingency table. By analyzing the Dice coefficient values over all possible threshold values, this measure can be used to detect the optimal threshold values for which the majority of the proliferative tumor subvolumes were detected.

The goal of this study was to investigate the spatial concordance between the pattern of intratumoral ^{18}F-FLT uptake and the spatial distribution of cell proliferation markers using tumor tissue obtained from small animal xenograft tumor models. By using Dice and *ROC* analysis, it can be demonstrated that high FLT uptake values are

within areas of active cell proliferation. Furthermore, analyzing threshold specific measures, the specificity and sensitivity of the proposed classification method can be directly evaluated for any threshold value. As mentioned in Chapter 1, this study will provide the first experimental data set demonstrating in vivo correspondence between areas of high FLT high and areas of active cell proliferation. This spatial correspondence was analyzed based on two-dimensional analysis of images obtained from individual tumor sections from different tumor specimens. The details of this study have been previously published in Radiotherapy and Oncology[109].

3.2 Methods

Experimental design

The detailed description of the experimental procedures used in this study was presented in the chapter 2. Briefly, head and neck tumor xenografts were developed in immune-compromised mice. When the tumors reached approximately 1 cm in diameter, animals were anesthetized. Before sacrifice, the animals were injected i.v. with a bolus containing the ^{18}F-FLT radiotracer. Two consecutive intraperitoneal injections of BrdU, used as a marker of cell proliferation[77], were administered. After sacrifice, the tumors were excised, frozen, and embedded in OCT. From each tumor specimen, several stacks of consecutive 8 μm thick tissue sections were obtained. Using one tumor tissue section selected from each stack, phosphor plate autoradiography was utilized to image the intratumoral distribution of ^{18}F-FLT[76]. ^{14}C standards were simultaneously exposed with the tissue sections. The DAR images were digitized and image intensity values were converted to actual activity concentration (Bq/mm^2).

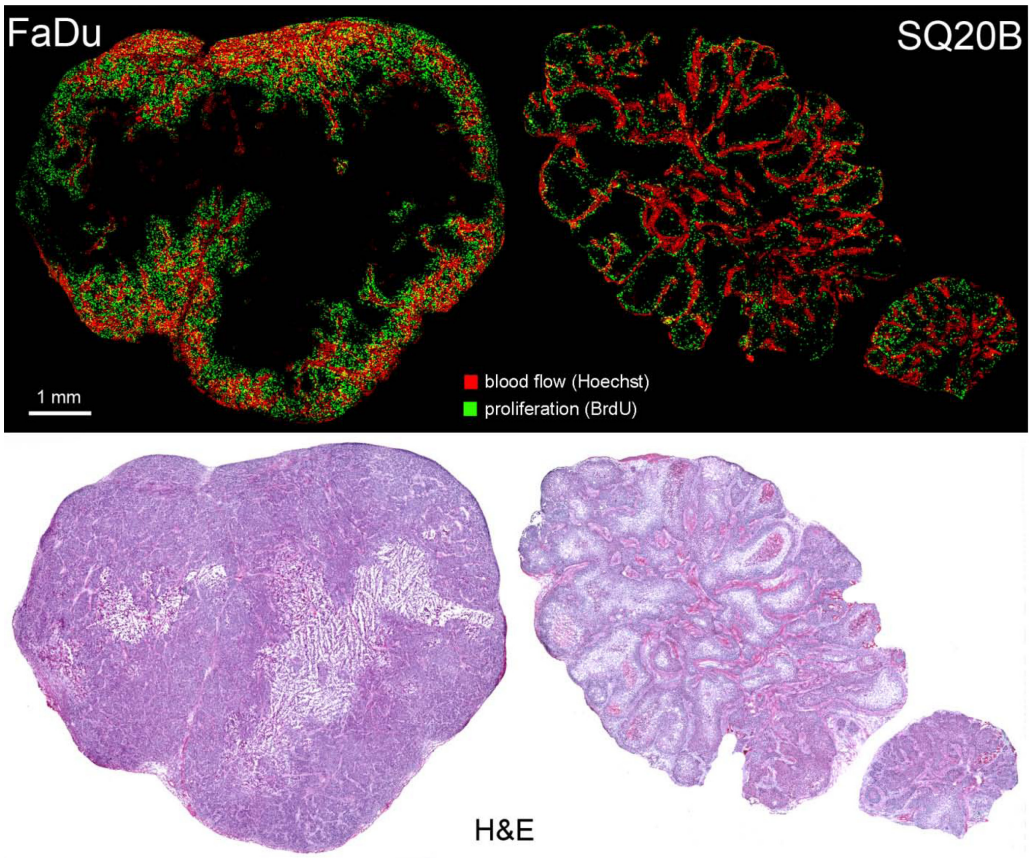

Figure 13. Representative microscopy images sets for the two tumor models used in this study. Top row shows images of blood flow and cell proliferation. Bottom row shows corresponding H&E image.

Following immuno-histochemical processing of the tissue sections, BrdU images of cell proliferation were acquired with fluorescence microscopy (Figure 13). H&E images were acquired.

Image processing

The DAR and IFM images were co-registered using a combination of deformable and rigid registration as presented in the previous chapter, with an overall registration error of less than 45 μm.

To define the regions of interest for the spatial concordance analysis, the extent of the viable tissue was delineated based on H&E images. First, any non-tumor tissue (muscle, lymphatic tissue) and specimen edges were removed using Photoshop CS4 Extended tools. These corrected H&E images were processed in MATLAB, and utilizing color segmentation and morphological processing, the viable tissue masks were obtained as a subset of the whole tissue area (Figure 14).

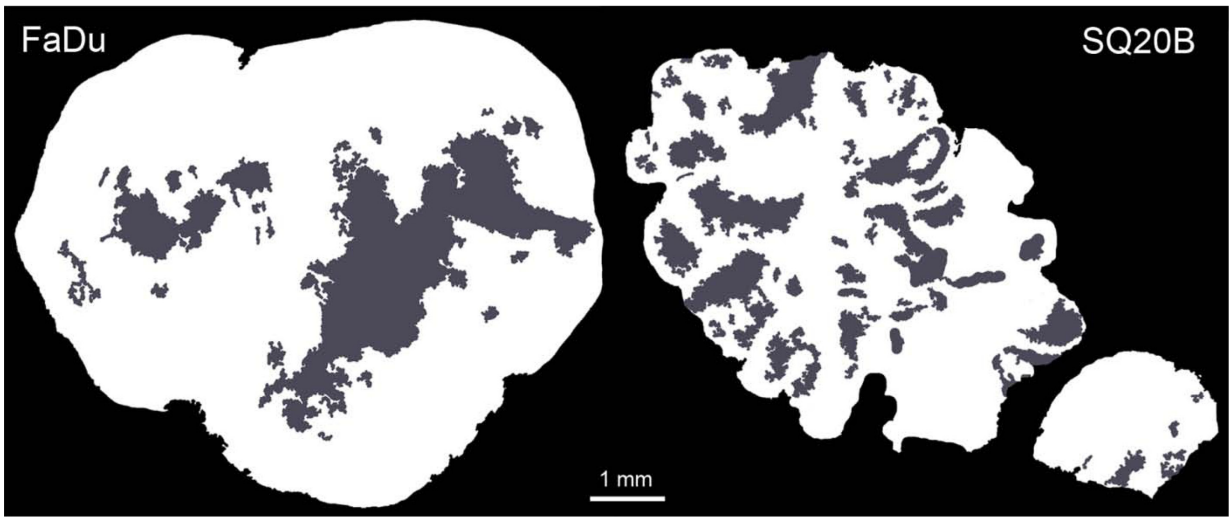

Figure 14. Viable tissue (shown in white) and necrotic areas (shown in grey) obtained from H&E images. Only the viable tissue is utilized for analysis.

To minimize the effect of residual registration misalignments, the DAR images were rebinned to 50 µm per pixel, utilizing the mean intensity value for the resulting pixels. A different approach was adopted for the rebinning of proliferation images. In the first step, all non-specific staining that occurred in necrotic parts of the tissue was masked out using the viable tissue mask. Secondly, the corrected images were binarized utilizing a local Otsu thresholding method[110, 111]. The resulting mask was used to remove

all low-intensity non-specific staining inside the viable tissue, obtaining corrected images of cell proliferation. Since the viable tissue masks were obtained from different (albeit adjacent) tissue sections, manual removal of any remaining high-intensity staining artifacts was performed. In a final step, a global Otsu threshold was applied to the corrected cell proliferation images to obtain only true positive areas of BrdU staining. The resulting binary image was rebinned to 50 μm pixel size, so that the value assigned to each pixel represented the fraction of its area that was positively stained. The resulting image was referred to as the proliferative cell density image throughout the rest of the study. To preserve consistency in the analysis of the regions of interest, the viable tissue masks were also rebinned to 50 μm per pixel. For the purpose of image analysis, the BrdU-based proliferative cell density images obtained as described above were used to establish the ground truth images of cell proliferation. Specifically, a proliferative cell density threshold value was chosen such that the truth set was sensitive enough to include the majority of BrdU positive cells. Therefore, if the 50-by-50 μm unit area contained more than 1% stained surface it was considered a positive. The resulting binary image was defined as the truth set (*T*).

Image analysis and statistical evaluation

An instance of the measurement set (*M*) was obtained by segmenting the FLT DAR image. By varying the segmentation threshold from the minimum to the maximum DAR image intensity levels, a range of measurement sets was obtained. The overlap between the truth set, *T*, and the measurement sets was analyzed as a function of the threshold value. For each FLT threshold value, the intersection sets were calculated as

presented in Figure 12: the true positive set ( ), the true negative set ( ), the false positive set ( ), and the false negative set ( ). Using these intersection sets, the Dice coefficient (*D*) was calculated for each threshold value[107, 108]:

$$D(T,M)=\frac{|T\cap M|}{\frac{1}{2}\left(|T|+|M|\right)}=\frac{|TP|}{\frac{1}{2}\left(|TP|+|FN|+|TP|+|FP|\right)}$$

ROC curve analysis[106] was also carried out. This classic test of diagnostic accuracy was adapted to investigate the reciprocal relationship between the sensitivity and specificity of FLT segmentation correctly classifying the pixels where active cell proliferation occurred. The *ROC* graph depicts on the y-axis the ratio between the number of correctly classified pixels and total number of pixels for each instance of the measurement set, also called sensitivity (or recall):

$$Sensitivity(T,M)=\frac{|TP|}{\left(|TP|+|FN|\right)}$$

The x-axis indicates the ratio between incorrectly classified pixels and the total number of pixels, also mentioned as 1-Specificity (or false positive rate):

$$FPR(T,M)=1-\frac{|TN|}{\left(|FP|+|TN|\right)}$$

To compare the relative efficacy of this classification method for different scenarios, the area under the curve (*AUC*) was obtained. The *AUC* represents a significant single-value indicator of the expected performance of segmented FLT images correctly representing the spatial distribution of BrdU positive cells. The *AUC* values are recoded as values between 0 and 1, where 1 represents an ideal classification result. Areas less than1 occur when significant false positive and false negative fractions are recorded.

Areas of 0.5 stand for random classification result. Good classification performance is indicated by values generally equal or greater than 0.7[105].

While ^{18}F autoradiography is characterized by high imaging spatial resolution, it is nevertheless significantly lower than the resolution necessary to resolve microscopic details such as those visible in the IFM images of BrdU uptake. Therefore, partial volume effect results in lowering of the signal at an arbitrary location and spilling it over into the adjacent regions in the image. To study the influence of image resolution-induced effects on the spatial concordance results, the BrdU images were blurred with a 300 μm Gaussian filter as to create simulated autoradiography images. The size of the blurring kernel was an estimate of the ^{18}F positron autoradiography resolution when imaging with phosphor plates, based on existing literature[102, 103, 112]. Subsequently, these BrdU-based simulated autoradiography images were segmented as was done in the case of the FLT autoradiography, and were used to obtain measurement sets in the threshold-based image analysis as described before.

All statistical tests were done utilizing the Statistical Toolbox offered within the MATLAB R2010a package. Since the data samples were small (8 FaDu tumors, 7 SQ20B tumors), normality of the data could not be clearly demonstrated. Therefore, non-parametric hypothesis testing was utilized, specifically the two-sided rank sum test (Mann-Whitney U test). A *P* value less than or equal to 0.05 was considered statistically significant.

3.3 Results

Tumor characteristics

Whereas both investigated tumor lines were human squamous head and neck cancers, they expressed different rates and patterns of growth (Figure 13). FaDu, a human hypopharyngeal cell line produced tumors at least twice as fast as SQ20B (laryngeal origin) for the same caliper-measured volume. Both tumor models present heterogeneous pattern of BrdU DNA incorporation across the tumor section, with higher uptake generally adjacent to well vascularized areas.

ROC analysis

The *ROC* analysis consists of a two-dimensional representation of classifier performance (FLT-positive pixel correctly classifying BrdU positive pixel) and is visualized within the unit square (Figure 15). Therefore, the *AUC* values were between 0 and 1, with values closer to unity indicating a greater accuracy of the classification method. For FaDu tumors, the median value for the *AUC* was 0.74 with a range of 0.55-0.84, while for SQ20B tumors the *AUC* median value was 0.51 with a range of 0.42-0.69. The difference in medians was significant at 5% level. Higher values of the *AUC* provide direct evidence of the spatial concordance between the areas of increased activity in the FLT DAR images and the areas of increased proliferative cell density.

A sensitivity analysis was also conducted where the variation of the *ROC* curves and *AUC* values was assessed as a function of the threshold value applied to obtain the truth set. Therefore, the measurement sets were compared against more conservative truth sets. These sets were obtained by increasing the minimum proliferative cell density value above which the resulting pixel in the truth set was positive (10% vs. 1%). For

FaDu tumors, the new median *AUC* value was 0.73 with a range of 0.5-0.84, not significantly different from the original value. Similarly, for SQ20B tumors, the new median *AUC* value of 0.48 (0.41-0.6), was not significantly different from the value calculated for 1% proliferative cell density. The *AUC* values were still significantly different between the two tumor lines.

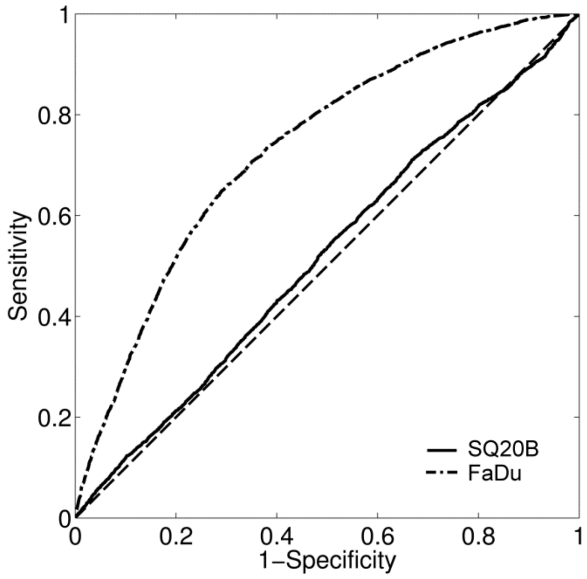

Figure 15. Examples of *ROC* curve analysis for utilizing segmented FLT images to predict the spatial distribution of cell proliferation. Presented results were representative of the two tumor specimens presented in Fig. 2 (AUC_{FaDu} = 0.73; AUC_{SQ20B} = 0.52). The diagonal dashed line (*AUC* = 0.5) represents the random chance line.

Dice coefficient analysis

For each FLT threshold level, a Dice coefficient value was calculated (Figure 16). The Dice coefficient values indicated the fractional amount of overlap between the segmented FLT area and the BrdU truth set. For FaDu tumors, the median value for the maximum Dice coefficient was 0.61 (range: 0.26-0.77), while for SQ20B it was 0.55 (range: 0.44-0.69). The difference in median values was not statistically significant at 5% level (P value = 0.31).

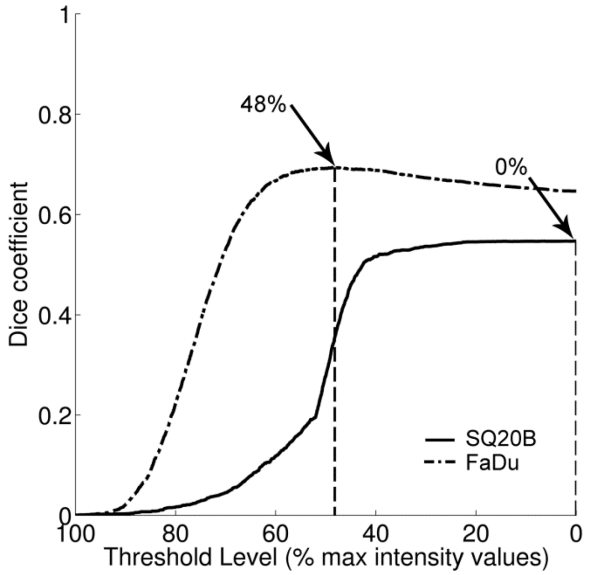

Figure 16. Dice overlap analysis. Presented results were representative of the two tumor specimens presented in Fig. 2 (D_{FaDu} = 0.69; D_{SQ20B} = 0.55). Arrows indicate FLT threshold level for which the maximum Dice coefficient was calculated for the selected tumor sections.

A significant difference between the median values of the FLT thresholds at which the maximum Dice coefficient occurred was recorded. For FaDu tumors, it was 38.5%, while for SQ20B tumors it was 7%. As for *ROC* analysis, the sensitivity of overlap analysis as a function of the proliferative cell density threshold value was assessed. Using a more conservative truth set, the maximum overlap decreased, as indicated by a median Dice value of 0.38 for FaDu tumors and 0.16 for SQ20B tumors. The difference in median threshold value at which maximum overlap occurred remained statistically significant between the two tumor lines, 57% for FaDu tumors, and 24% for SQ20B tumors.

Effect of autoradiography resolution

To study how finite imaging resolution-blurring present in autoradiography images affects the results of the analyses presented above, the BrdU microscopy images were convolved with a Gaussian kernel of the same size as the estimated resolution of ^{18}F autoradiography.

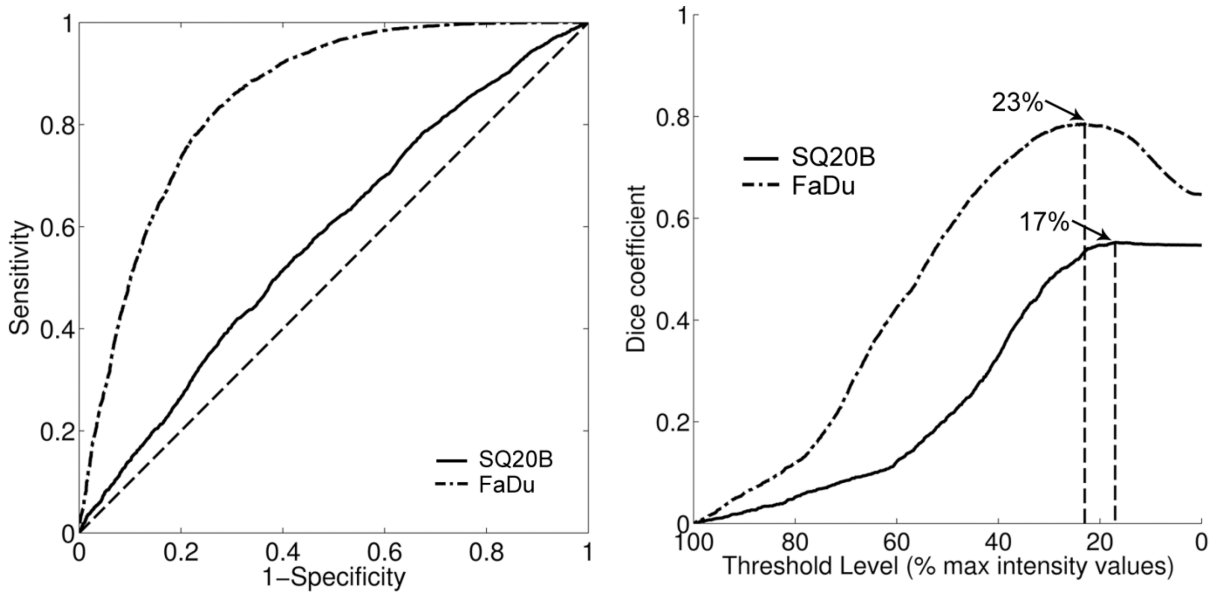

Figure 17. *ROC* and Dice analysis of blurred BrdU image vs. BrdU-derived truth set: top panel – *ROC* analysis (AUC_{FaDu} = 0.86, AUC_{SQ20B} = 0.59), bottom panel – Dice coefficients vs. threshold levels of blurred BrdU image. Arrows point to the threshold values at which the maximum Dice coefficient occurs (D_{FaDu} = 0.79, D_{SQ20B} = 0.56).

These blurred BrdU images were used to create the measurement sets, while the high-resolution BrdU images were used to determine the truth set. Whereas there was perfect spatial co-localization between the images used to produce the two sets used in the analysis, the *ROC* analysis indicated less than perfect spatial concordance between blurred BrdU and proliferative cell density images (Figure 17). FaDu models presented

a median *AUC* of 0.92 (0.82-0.95), while for the SQ20B tumors the *AUC* was 0.7 (0.55-0.82). In addition, the overlap analysis indicated that the median value for the maximum Dice coefficient was 0.77 (0.59-0.85) for FaDu tumors and 0.61 (0.49-0.72) for SQ20B tumors.

3.4 Discussion

The spatial concordance between intratumoral FLT uptake and the distribution of cell proliferation markers was studied using small animal tumors representative of human squamous head and neck cancers. The results presented here complement those of previous studies in which ^{18}F-FLT was investigated as a tracer for PET imaging of cell proliferation without addressing the issue of spatial correspondence between the patterns of FLT uptake and cellular proliferation[41, 46, 55, 113]. While less important for many diagnostic applications of FLT PET imaging, the issue of spatial concordance is of utmost importance in radiation oncology treatment planning, where boundaries of the high PET tracer uptake region are used to define shape and extent of radiation dose distribution used for boosting the patient's high risk GTV subvolume.

Experimental setup

Some of the experimental details need further discussion. In this study, automated immuno-histopathological processing of the tissue and standardized image acquisition protocols allowed consistent results in obtaining the microscopy images. The necessary confidence in the truth set definition was further ensured by careful examination and correction of staining artifacts. In addition, Otsu thresholding has been

shown to be one of the most efficient algorithm for segmentation of fluorescent images[111]. As for the sensitivity of the truth set to the proliferative cell density value used to define the truth set, a preliminary analysis was conducted. *ROC* analysis results were not significantly different, indicating that the specificity of FLT segmentation was consistent in classifying the active proliferation areas indicated by more conservative truth sets. The overlap analysis indicated the expected results for a gradual decrease in extent of the truth set. This study was based on the observations from two tumor lines, utilizing specimens from 15 tumors total. By expanding the study to include more tumor specimens and other cell lines, will allow for further evaluation of FLT images as indicators for determining the spatial distribution of cell proliferation.

FLT for imaging spatial pattern of cell proliferation in FaDu and SQ20B tumors

Thresholding the FLT autoradiography was the investigated method to retrieve the spatial pattern of cell proliferation. As pointed out by the *ROC* analysis of FaDu tumor data, the median *AUC* value of 0.74 indicated that FLT segmentation was a good method for identifying proliferating subvolumes. In addition, this finding is a direct indicator that FLT high-uptake regions in the FaDu tumors are spatially concordant with areas of increased proliferation. Dice coefficient values varied across the range of FLT threshold values selected for particular instances of the measurement sets. The presence of a peak Dice value revealed that there were FLT segmentation values for which there was a maximum amount of overlap between the thresholded FLT image and the BrdU-defined truth set, and the true positive fraction was greater than the false positives. For FaDu tumors, this was achieved at a median threshold value of 38.5%.

For the SQ20B tumors, the maximum amount of overlap between FLT-segmented areas and the truth set was similar, as indicated in the median value of the Dice coefficient (0.55). While not significantly different from FaDu data, these values consistently occurred for very low FLT threshold values (median of 7%). This indicates that for SQ20B tumors, FLT-segmented areas include a maximum amount of the truth set only when the majority of the intensity values were included into the segmented set (large false positive fraction). Since it is expected that higher intensity values be co-localized with the areas of active proliferation, this result provides direct evidence of the lack of specificity in retrieving the spatial pattern of cell proliferation. *ROC* analysis also supported this finding, where the median *AUC* value was 0.51. The low *AUC* value (representative of random chance in *ROC* analysis) indicates that for this tumor type, the areas of increased FLT uptake were not spatially concordant with the areas of increased proliferation.

Tumor morphology

The results obtained for the SQ20B tumor model were unexpected. The experimental methodology was identical for the both head-and-neck tumor models. The only fundamental difference between them that could explain the observed differences was in their pattern of growth and the resulting distribution of microenvironmental features. The faster growing FaDu tumors, presented a highly compartmentalized spatial pattern of cell proliferation (Figure 13). There was uniform BrdU uptake all throughout the well-vascularized area, creating a proliferating rim surrounding hypoxic

and necrotic tumor regions. In contrast, a slow, lobular type of growth induced a dispersed uptake pattern of BrdU in the SQ20B models.

Imaging resolution

Since the microscopic features observed in the cell proliferation images were on a smaller scale than the autoradiography resolution, it was necessary to investigate the direct effect of finite imaging resolution on the spatial concordance results. This was done with the aid of the BrdU images blurred with the kernel simulating the resolution limitation of autoradiography images. Thresholding of the blurred BrdU image was less specific at retrieving the spatial pattern of original BrdU staining distribution in SQ20B tumor xenografts, than in the FaDu tumors (Figure 17). Since the same blurring kernel was applied to both tumor models, this effect could only be caused by the degree of heterogeneity in the spatial distribution of cell proliferation. The SQ20B tumor models had a more dispersed distribution of proliferation markers. Correspondingly, blurring affected these tumors more so than the FaDu tumors, which had a more compartmentalized distribution of cell proliferation. For the latter tumor model, the typical size of the actively proliferating ‘‘compartments’’ was similar or larger than the resolution of autoradiography, therefore blurring did not affect their general spatial distribution. On the other hand, for the SQ20B model, there was no clear compartmentalization of proliferation. After blurring, the typical size of the observed features was significantly larger than of those seen in the original BrdU microscopy image.

FLT-based delineation of actively proliferating tumor subvolumes

When applying the tumor-specific median value for the FLT threshold that produced the maximum overlap between areas of increased proliferation and segmented FLT area, the results were indicative of the difference between the two tumor lines. As emphasized with the blue contour line (Figure 18), the regions delineated on SQ20B tumors coincided with the whole tissue section area in the majority of cases, while for the FaDu tumors the actively proliferating “compartment” was correctly delineated. To visualize the possibility of misinterpretation of segmented FLT regions, the 50% of maximum intensity threshold value was utilized for images from both tumor lines (red contour, Figure 18), as a global threshold that is commonly utilized for FLT PET segmentation[35, 114]. There were distinct areas delineated on both tumors. This threshold value resulted in segmented areas that were more conservative, but which were still spatially concordant with areas of increased cell proliferation in FaDu tumors. At the same time, the segmented areas significantly underestimated the extent of the cell proliferation in the SQ20B tumors.

Spatial concordance of FLT uptake and cell proliferation

As illustrated by the xenograft tumor data presented above, tissue morphology and the resulting spatial heterogeneity of cell proliferation, together with finite imaging resolution, significantly affect the feasibility of using ^{18}F-FLT DAR images to specifically predict the spatial distribution of cell proliferation, as imaged with BrdU. This directly affected the study conclusions about the generality of FLT spatial concordance with cell proliferation. While for FaDu tumors spatial concordance was clearly supported by the

data acquired, the same cannot be said about SQ20B tumors. However, this does not imply that there is no spatial concordance between FLT uptake and cell proliferation in both of the tumor models at a cellular level. The experiment with the blurred BrdU image confirmed that the spatial concordance analysis for SQ20B tumors is inconclusive due to the mentioned combined effect of imaging resolution and spatial proliferation pattern heterogeneity. The dispersed pattern of cell proliferation imaged in these tumor samples could not be resolved by autoradiography with ^{18}F. As a result, the overall high tracer uptake across the tumor section correctly indicated the ubiquitous presence of active cell proliferation throughout the tissue section specimen. Nevertheless, the noise associated with ^{18}F autoradiography and the overlap of the “spill-off” regions corresponding to each cell containing the tracer, made it such the high-activity regions recorded in the autoradiographic image did not coincide with the location or the extent of the imaged spatial pattern of cell proliferation. Depending on the tumor-to-background uptake ratio while imaging in vivo, FLT PET may correctly determine that for tumors such as SQ20B, the whole tumor is actively proliferating. Nevertheless, this aspect needs further analysis.

Conclusion

In this study, autoradiography images were utilized for the delineation of distinct tumor subvolumes of increased cell proliferation. The results indicate the difficulties in this process present even when utilizing autoradiography imaging, which is characterized by the resolution superior to that of any small-animal PET or clinical PET scanners. In PET imaging, the averaging effect induced by positron travel alone can

significantly reduce the ability of FLT uptake images to correctly reproduce any map of cell proliferation. It seems that as long as the compartmentalization of the tumor microenvironment presents features that can be resolved with the employed imaging modality, subvolume delineation is feasible.

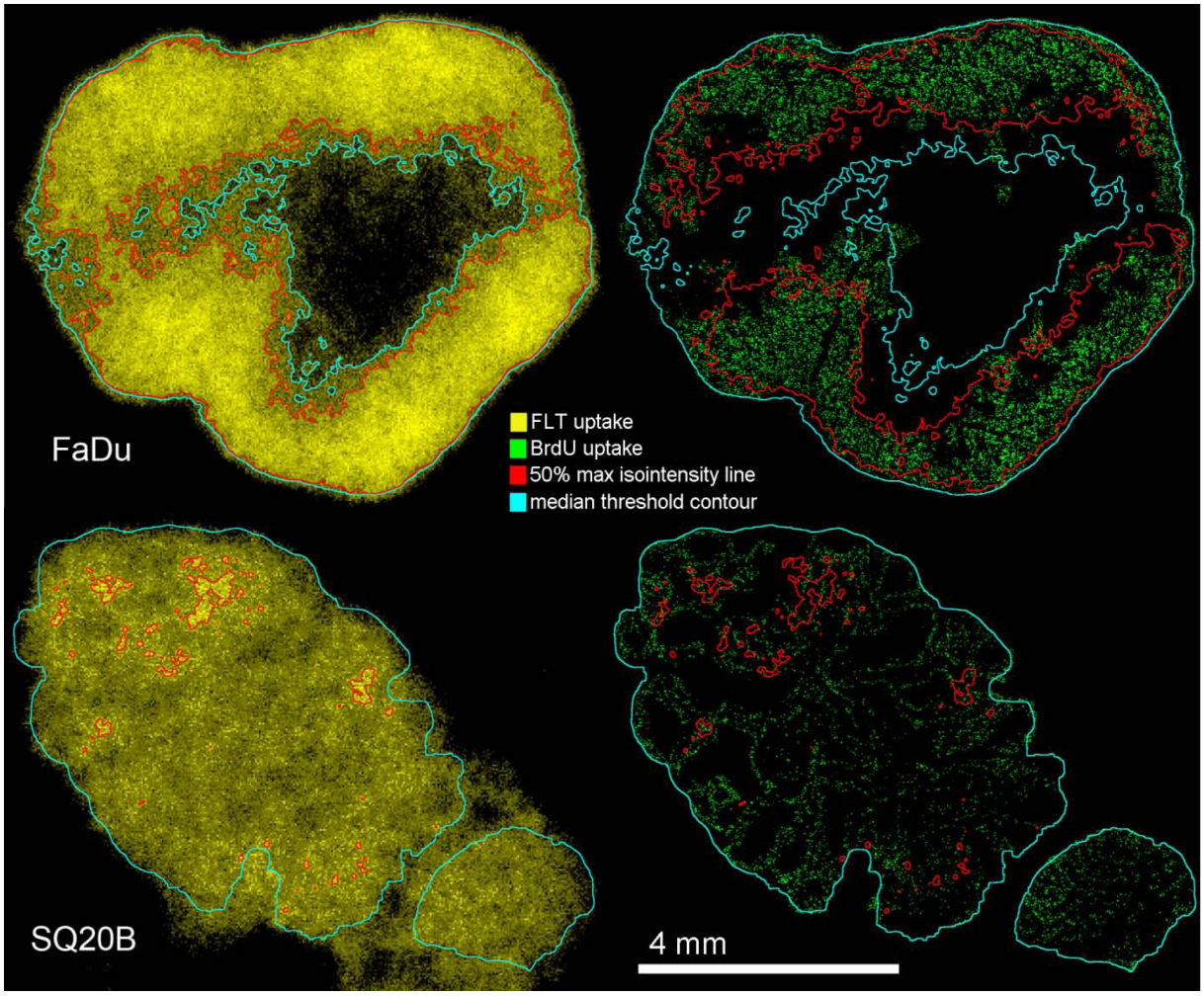

Figure 18. Tumor subvolumes delineated based on thresholding ^{18}F-FLT autoradiography. FLT threshold contour (iso-intensity) lines were then superimposed on BrdU microscopy images.

These observations agree to other studies investigating the ability of ^{18}F-FDG[69] or ^{18}F-FAZA[70] to reproduce the intratumoural distribution of their intended biological target. Further studies of the spatial concordance between the actual intratumoural

pattern of FLT uptake in PET images and the spatial distribution of cell proliferation in human pathological samples could elucidate the situations in which imaging with this particular tracer could provide useful information on the spatial distribution of actively proliferating cells.

4. PET simulation

4.1 Introduction

In chapters 2 and 3, the first specific aim was addressed. Specifically, the spatial concordance between FLT uptake pattern and the spatial distribution of cell proliferation was analyzed at a microenvironmental level. The microscopic uptake of FLT was imaged with DAR, while the pattern of BrdU uptake represented a surrogate for the spatial distribution of active cell proliferation. It was observed that when tumors present a pattern of cell proliferation that is highly dispersed throughout the tumor, even high-resolution imaging modalities such as DAR could produce incorrect predictions about the extent and spatial distribution of proliferative tumor subvolumes. While spatial coincidence between high FLT uptake regions and actively proliferative subvolumes was demonstrated in tumors with highly compartmentalized/aggregated features of cell proliferation, there were no conclusive results across the utilized tumor lines. This emphasized the need for histopathological validation of FLT PET imaging for image-guidance applications in radiotherapy.

In most diagnostic applications of PET imaging in oncology, PET data is used to extract metrics such as $SUV_{average}$, SUV_{MAX}, or SUV_{peak} that allow to test for the presence of disease or to predict characteristics of the tumor as a whole. Validation of such PET imaging application can be done by establishing the correlation between single-value SUV-based metrics characterizing in vivo PET tracer uptake and ex vivo pathological indices representative of the target biology (e.g. proliferation index) over a population of patients[46].

However, when PET imaging is used for radiation therapy guidance, e.g. to identify aggressive tumor subvolumes that can be targeted with selective dose escalation, it is the spatial characteristics of the PET images that are used to define the treatment dose distribution. Correspondingly, validation of PET imaging for radiation treatment planning requires an approach that allows testing the spatial coincidence of the region of high tracer uptake, as imaged with PET, and the biological/morphological features of interest. The gold standard for validating PET imaging for radiotherapy image guidance is histopathological validation, whereby non-invasive PET images are registered to ex vivo histopathological images enabling the analysis of their spatial association. Unfortunately, the required registration of PET and histopathological data is a subjective process that is prone to error. Furthermore, the registration is not always feasible due to the significant deformation of the specimen after the surgical excision. Several groups have reported experimental methods for high-precision co-registration of histopathological images with in vivo PET images from small-animal models achieving a registration error of less than 0.3 mm. However, these methods either necessitate invasive fiducials that can alter the tracer uptake[73], or require embedding the animal in liquid molds[72, 115], which can potentially interfere with normal animal physiology and prohibit their adaptation to human validation studies.

Various surrogate histopathological validation techniques involving human specimens have been developed to test the accuracy of PET-based gross tumor volume delineation. In these studies, in vivo PET images are segmented utilizing selected thresholding protocols and either segmentation volumes or their largest diameter is compared to those of surgically resected tumor specimens[116-118]. While good

correspondences were reported between PET-derived metrics and those obtained from ex-vivo imaging, the methodology used in these studies does not provide the spatial information necessary for the analysis of the spatial correspondence between the PET tracer distribution in tissue and corresponding biology[119, 120].

In this study, an alternative method for histopathological validation of PET imaging for radiotherapy image-guidance applications is presented. This method circumvents the problems associated with the registration of in vivo PET images with microscopic histopathological images. The approach is demonstrated using small-animal tumor models. However, the method is equally applicable to the clinical PET imaging validation using whole-tumor specimens of human origin.

Utilizing whole tissue specimen sections, autoradiography was used to obtain images of the microscopic distribution of the PET tracer. Tumor microenvironment and morphology images were obtained from the same locations. Using the reconstructed tracer 3D distribution, realistic synthetic PET (sPET) images were obtained. Monte-Carlo models of clinical and research PET scanners exist in literature[121-124] and they can be used to perform accurate simulations of all physical processes contributing to PET image formation and to arrive to sPET images that are representative of a given 3D microscopic tracer distribution. However, as a proof of principle, a simplified approach to PET image simulation was utilized in this study, where sPET images were obtained by convolution of the intratumoral tracer distribution with a 3D kernel representative of the spatial resolution of a small-animal PET scanner.

By virtue of their generation, sPET images are perfectly registered to the underlying autoradiography data that in turn can be precisely registered to the

histopathological images of tumor microenvironment[79]. Therefore, the resulting sPET image sets can be used to study the spatial concordance between the pattern of the tracer uptake as depicted in PET images and underlying microenvironment, without the confounding effects of registration uncertainties.

4.2 Methods

Tumor Models and Radiotracer

As before, human head and neck tumor xenografts (SQ20B) were developed in male athymic mice (NCr-nu/nu; National Cancer Institute), from bilateral flank subcutaneous inoculation of 10^6 cells/site. Animals were maintained according to the protocol approved by the Institutional Animal Care and Use Committee at Virginia Commonwealth University. The PET simulation and tracer validation process was demonstrated using a different tracer from FLT, as to demonstrate its versatility. ^{14}C-labeled 2'-Deoxy-2'-[F]fluoroglucose (American Radiolabeled Chemicals, Inc.) was utilized as the investigated tracer. This compound is chemically identical to the clinically utilized ^{18}F-FDG, and it was utilized for the autoradiography resolution advantage that the 14C β^- low-energy decay particle offers.

Tumor Tissue Collection

After the tumors reached 1 cm in diameter as measured by caliper, the animals were anesthetized with a mixture of oxygen and isoflurane. At 80 min before planned animal euthanasia, a bolus injection containing Hoechst (0.4 mg/20-g mouse), and 925 kBq of ^{14}C-FDG was administered by tail-vein injection. After animal sacrifice, tumors

were immediately excised. The entire surface of the exposed tissue was coated with Davidson Marking System black ink (Bradley Products, Inc.), and then embedded in OCT.

For embedding, a special jig was built (Figure 19A), which was similar to a previously reported prototype. Specifically, parallel holes were drilled in two rigid plastic boards (6 mm thickness). Their spacing and diameter was chosen such that they would fit 18G needles (BD Biosciences) in such a way as to allow a tumor specimen to fit in between the needles. The needles were first inserted into the bottom plastic plate, then through a disposable plastic mold used for specimen freezing. The excised tumor was positioned in the mold containing the OCT, between the needles. Then, the top plate was placed on top of the mold, allowing the needles to go through. After the assembly was tightened with screws, it was placed on dry ice for freezing. After the OCT solidified, the needles were retracted and the tumor specimens were sectioned with a Leica CM1850 UV cryostat (Leica Microsystems) at 8-μm tissue section thickness and mounted on glass microscope slides.

During cutting, a stack of 3-4 consecutive tissue sections was collected every 120 μm throughout the specimen. In addition, for every sequential stack of tissue sections, a digital image of the cutting plane was acquired utilizing a Pentax Optio S7 digital camera in macro mode employing a remote trigger. The camera was mounted on a custom-built plastic frame that fitted the cryostat work-window (Figure 19B). The double ball-in-socket adjustable locking mount (Ram Mounts Cat# RAM-B-202AU, RAM-B-201U, RAM-B-202U, National Products, Inc.) allowed for an accurate alignment of the camera optical axis with the axis of the specimen holder, perpendicular to the

cutting plane. Once camera position was selected, the joints were locked in place, ensuring the reproducibility of the position from which the digital image of the tissue block was taken (Figure 19C).

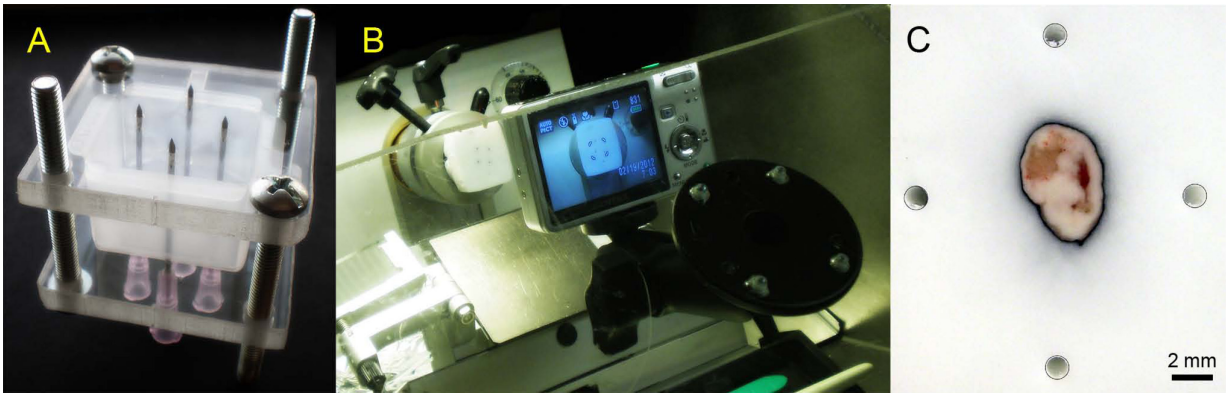

Figure 19. A. Freezing jig for tissue specimen. B. Cryostat setup with mounted camera on double-jointed adaptor. C. Example of the tissue specimen digital photo with hollow columns as registration fiducials. The margins of the tissue were inked to increase the contrast of the tissue boundary.

Tissue Imaging

One section from each image stack obtained at every sampling location was used for autoradiography. The sections covered with a thin plastic wrap (<20 μm) were placed in contact with the phosphor plates in light-tight cassettes for 5 days at room temperature. The imaging plate was read with Typhoon 9410 Variable Mode Imager (GE Healthcare) to obtain images of the FDG distribution (Figure 20B). The reader output was digitized in grayscale TIFF images with 25 μm pixel size. The grayscale intensities were converted to activity concentration based on the images of ^{14}C standards that were co-exposed with the tissue sections to the same imaging plates.

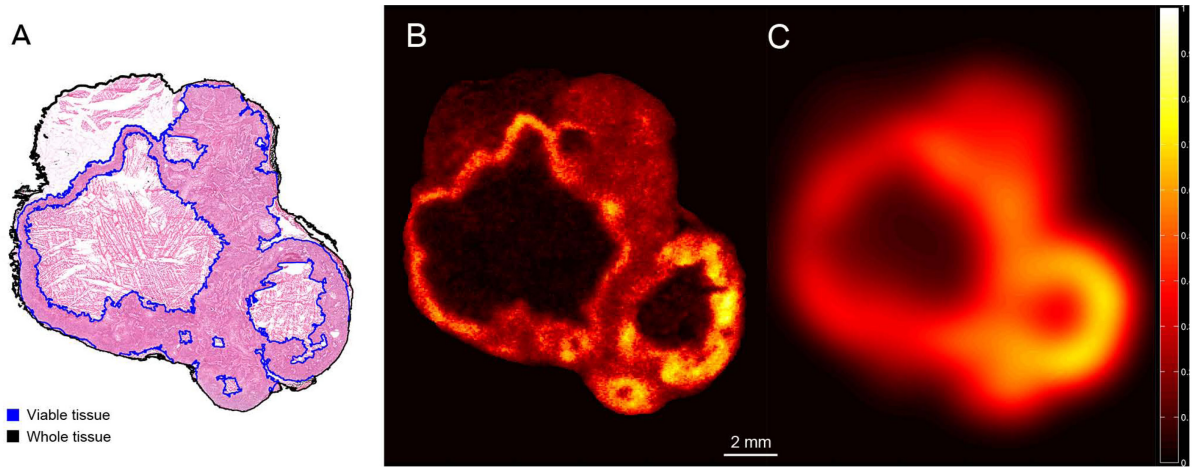

Figure 20. Tumor B images. A. Microscopy image of hematoxylin and eosin staining. Image was acquired at 20x using a motorized research Olympus BX61 microscope. B. Autoradiography image. C. Simulated PET image slice. Both B and C images were normalized to the maximum activity value in the whole tumor. All images are at the same scale.

Since the tissue utilized for autoradiography becomes dehydrated and can be damaged during plastic film removal, adjacent tissues were utilized to image the desired aspects of tumor morphology and/or microenvironment. For this study, H&E staining was performed on the tissue section adjacent to the section used for autoradiography. Any other relevant stain (e.g. hypoxia, proliferation, apoptosis, vasculature, etc.) can be carried out as well. The H&E microscopy image was deformably registered to the autoradiography image from the same stack using the methods described in chapter 2. The H&E images were utilized to define the extent of the tumor tissue (whole tissue mask) and the subset corresponding to the viable tumor tissue (viable tissue mask) (Figure 20A). This was done via MATLAB R2010a script utilizing the Image Processing and Statistical Toolboxes. The script was an adaptation of a color-based segmentation algorithm using K-means clustering, presented on the MathWorks site (http://www.mathworks.com/products/image/demos.html). The results of the viable tissue segmentation were reviewed by a pathologist to confirm validity.

3D reconstruction

In order to reconstruct the 3D spatial distribution of the intratumoral FDG uptake along with the 3D distribution of the viable tissue, a two-step process was utilized. First, the digital photo images of the cutting plane containing the inked tissue specimen (Figure 19C) were rigidly registered using the visible hollow needle tracks. The photographic images were then re-binned as to match the pixel size of the autoradiography images. In the second step, the pairs of already registered autoradiography and the viable tissue images from each sampling location were co-registered to their corresponding aligned digital photos. Since non-linear deformations occur during tissue cutting and mounting, it was necessary to use deformable registration for this step. Both autoradiography and H&E images are very different from the digital photos of the tissue. Therefore, intensity-driven or internal landmark-based registration strategies were not feasible. A contour-based deformable registration was utilized instead. The contours, represented by point-sets corresponding to the tissue boundaries (which remained intact during tissue section transfer onto the glass slide), were extracted from both digital photo and H&E microscopy image. A deformable transformation was obtained by aligning the contours, which was then applied to the autoradiography and viable tissue mask. Both registration steps were implemented in MATLAB R2010a using the rigid and non-rigid applications of the coherent point drift algorithm[88].

At the end of the registration process, all images were stacked into three-dimensional matrices, and rebinned at 50×50×120 μm per voxel utilizing the mean

values, in order to eliminate any residual misalignments after image registration. The resulting autoradiography stacked volume was analyzed for three-dimensional consistency. Consistency was defined in terms of smoothness the signal between consecutive slices[101]. Specifically a normalized correlation coefficient was calculated between each pair of consecutive slices, and the mean and standard deviation of the correlation coefficients was reported as a measure of the 3D consistency of the reconstructed volumes.

The error of the rigid registration of the digital photo images was measured in a separate experiment. Instead of a tumor specimen, a suture filament was tensioned in the tumor mold and embedded as presented above. The block was sectioned and the digital photo images were obtained and registered as before. The 3D coordinates of the suture filament in each section were detected. Utilizing linear regression, a line was fitted through the points such that the perpendicular distances from the data to the fitting model were minimized. The mean and standard deviation of the residual projection distances between fit model and data points were reported as the registration error.

PET simulation

The simulated PET image was obtained by convolving 3D autoradiographic data sets with the 3D point-spread-function kernel of the Siemens Inveon small-animal PET scanner (Siemens Medical Solutions, Inc.) using MATLAB R2010a (Figure 20C). The line-spread-function was measured utilizing a custom-built water-equivalent phantom containing a line source. The line source was a mouse tail-vein catheter (Braintree Scientific, Inc.), with an inner diameter of 0.17 mm, filled with 26.6 MBq/ml of 18F

solution. The PET scan setup was replicated according to NEMA recommendations for spatial resolution measurement[125]. The point-spread-function in each dimension was derived from the Gaussian fits of the line profile[126]. The results obtained in-house were consistent with previously published data[127, 128].

Spatial concordance analysis

For this study, FDG was chosen as an example of a PET tracer under validation. The spatial coincidence between the areas of high FDG uptake in the sPET images and the spatial distribution of the viable tissue, as defined based on H&E segmentation (Figure 20A), was analyzed utilizing overlap analysis (10). For each activity value found inside the volume defined by the whole tumor mask, the sPET image was thresholded obtaining a distinct segmentation 3D volume. These 3D tumor subvolumes were compared to the H&E-based viable tissue delineation (ground truth), and different intersection sets were obtained: true positive, true negative, false positive and true negative sets[108]. Based on these, Dice coefficient values were calculated to determine the spatial overlap between segmented volumes from sPET images and the viable tumor tissue at each threshold value. Receiver-operating-characteristic (*ROC*) curves were utilized to evaluate the overall performance of FDG segmentation at classifying pixels as viable or non-viable. The area under the curve was used as a measure of how well FDG thresholding determines the spatial extent of the tumor viable tissue. As the purpose of this study was to introduce a novel methodology for PET imaging validation for image-guidance in radiotherapy, the ability of FDG sPET to identify viable tumor tissue was used as an illustration only.

4.3 Results

Comprehensive sampling of the tumor tissue throughout the specimen is essential to the presented methodology. For the two SQ20B tumors (denoted A and B) that were utilized in this experiment, the total number of 4-section stacks were 41 and 48. The recorded time stamps on the digital photos indicated that for an experienced user, one 4-section stack could be consistently obtained every two minutes (120 μm inter-stack distance).

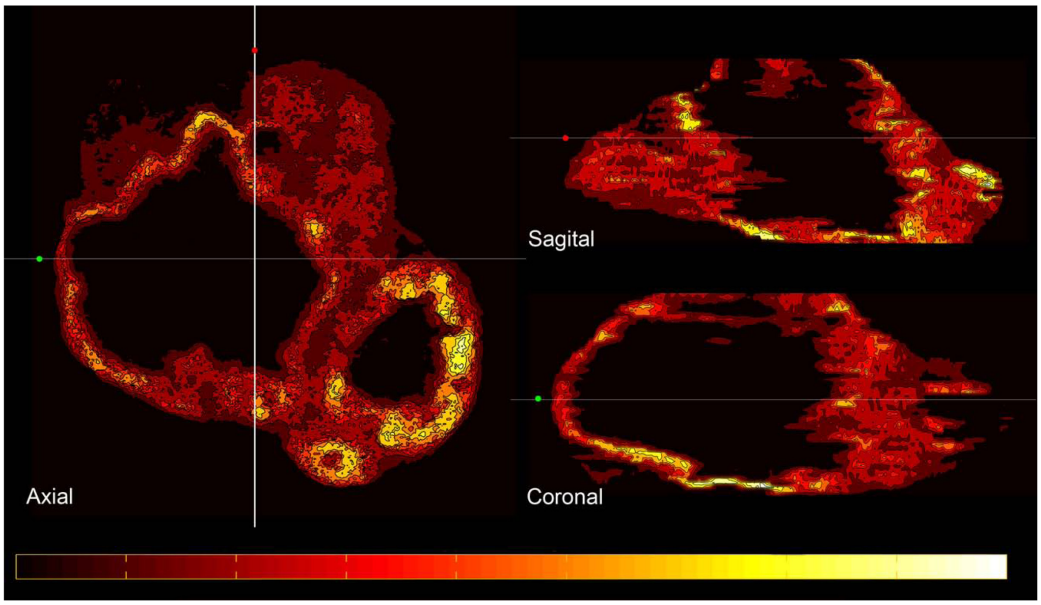

Figure 21. Orthoslices through tumor B. All images are normalized to the maximum tumor activity registered in the aligned autoradiography stack. Color bar indicates [0, 1] range.

3D reconstruction and PET simulation

The registration error of the rigid registration step in the reconstruction procedure was 6.56 ± 4.78 μm. Figure 21 depicts orthogonal slices though the reconstructed 3D FDG

autoradiography image-set, confirming the three-dimensional coherence of the set. This was also confirmed by an analytic measure of 3D consistency of the analyzed sets. The mean and standard deviation of the normalized intensity correlation between pairs of successive slices in the restacked autoradiography volume presented high correlation values 0.84 ± 0.05 (range: 0.73-0.91) and 0.94 ± 0.02 (0.86-0.97).

The sPET images were obtained by direct convolution of the reconstructed 3D autoradiography data was with a 3D Gaussian kernel representative of the point spread function of the Siemens Inveon small-animal PET scanner, as measured at the center of the scanner's field of view: 1.56 mm tangential FWHM, 1.62 mm radial FWHM, and 2.12 mm axial FWHM. Figure 20C presents a slice through the resulting sPET image set at the location corresponding to the autoradiography image presented in Figure 20B. As can be seen from the image, application of the 3D blurring kernel changes the image of the tracer uptake dramatically. The Dice overlap between the volumes obtained by thresholding of both sPET data set and the actual activity map reconstructed from autoradiography (the threshold set at 70% of maximum activity in both cases) was 0.0 and 0.1 as measured using Dice coefficients for tumor A and tumor B, respectively. These values increased to 0.02 and 0.34 for the threshold set at 50% of the maximum activity; 0.28 and 0.47 at 30% threshold, and 0.87 and 0.79 for 10% threshold. The difference between sPET and 3D autoradiography is illustrated in Figure 22, which shows 3D rendering of the thresholded volumes.

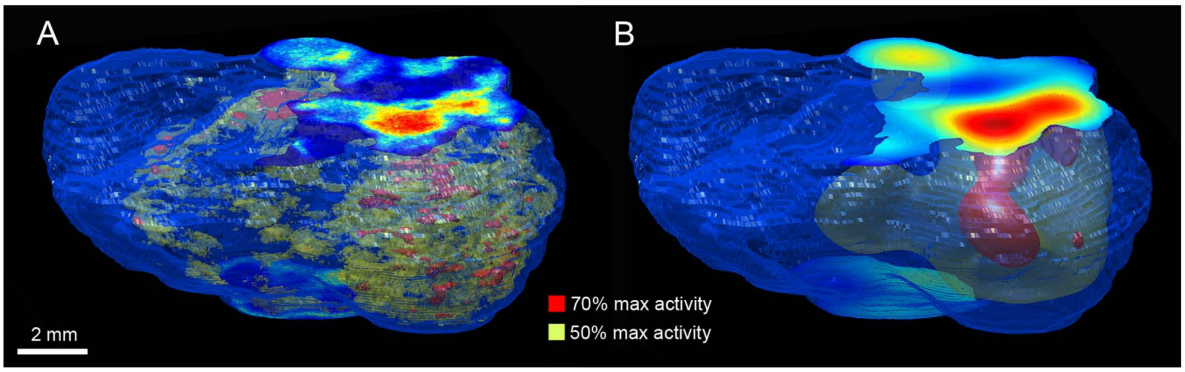

Figure 22. Rendered tissue outline with segmentation volumes. A. 3D reconstructed autoradiography. B. sPET. Threshold values represent percent of maximum intensity.

Spatial concordance between the FDG uptake pattern and viable tissue distribution

Figure 22B depicts the distinct tumor segmentation subvolumes resulting from sPET image thresholding performed using different activity values. To evaluate the classification performance of the thresholding operation performed on FDG sPET images as a method of viable tissue delineation, the area under the *ROC* curve (*AUC*) was computed as a single metric indicative of the performance of the investigated classification method. The results show that FDG segmentation is a good classifier for voxels containing viable tissue: $AUC_A = 0.74$ and $AUC_B = 0.81$, confirming that regions of higher FDG uptake are spatially co-localized with regions of viable tissue within the tumor.

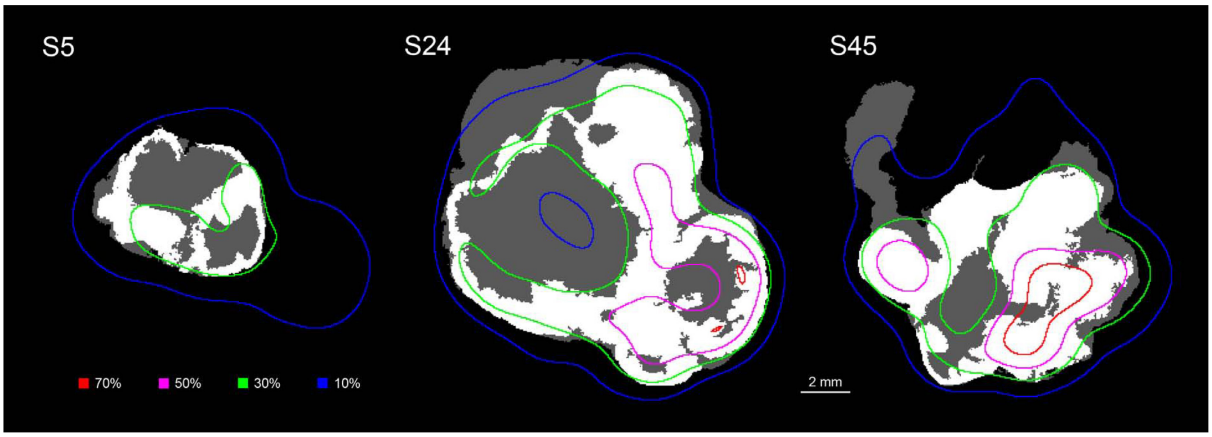

Figure 23. Three sequential sections through tumor B, presenting viable tumor tissue (white) as a subset of the whole observable tissue (gray). The colored lines present iso-intensity lines from the sPET image sequence. Thresholds are percent of maximum intensity. All images are at the same scale.

The maximum overlap between the FDG segmented volumes and the viable tissue subvolume as indicated by Dice coefficient values, was 0.8 for tumor A (at 22% of max intensity) and 0.88 for tumor B (at 14% of max intensity). FDG segmentation was highly sensitive at determining the extent of the viable tissue at these thresholds (true positive fraction, tumor A: 0.94, tumor B: 0.99), but it was not specific (true negative fraction, tumor A: 0.17, tumor B: 0.36). Figure 23 presents a sequence of viable tissue masks from tumor B, with overlaid iso-intensity lines obtained from the corresponding sPET image set. The segmentation volumes from which the iso-intensity lines were extracted covered the viable tissue for tumor A and tumor B respectively: 5.8% and 3.4% at 70% of maximum intensity, 39.6% and 27.9% at 50%, 84.2% and 81.4% at 30%, and 99.8 and 100% at 10% of maximum intensity.

4.4 Discussion

Our novel method of histopathological PET imaging validation does not require registration of in vivo PET data with histopathological images, a step prone to error and

subjectivity. Instead, the whole tumor specimen is used to obtain both histopathological data and the intratumoral distribution of the tracer that is subsequently used to generate a synthetic PET image. In this manner, all confounding factors associated with the registration of PET images to histopathological images are bypassed. Therefore, the only registration errors with potential effects on the spatial concordance analysis are the residual misalignments encountered between autoradiography and microscopy images obtained at each tumor sampling location (less than 45 μm).

Currently, a number of PET tracers targeting different aspects of tumor biology are being developed[38], and new PET-based dose escalation clinical trials [20, 22] have been proposed and conducted.

3D reconstruction

The tissue processing workflow is highly adaptable and inexpensive to implement for a wide range of microtomes, for frozen specimens. Different jigs can be built for different tumor sizes using readily available materials. Similarly, the camera mount can be adapted to multiple microtome geometries, and any compact digital camera with remote trigger can be utilized. While there are institutions with highly specialized infrastructure for 3D tissue reconstruction[94], the method presented in this study meets the demands of the validation goal: to obtain a 3D intratumoral distribution of a PET tracer that can be used to generate sPET images precisely registered to histopathological data. The 3D morphology of FDG uptake demonstrated good spatial correlation between neighboring slices, even though a non-negligible inter-slice distance was utilized

Histology studies have demonstrated that tumor vascular tree is the main factor affecting the shape and location of spatial gradients of the tumor microenvironment functional aspects such as hypoxia or cell proliferation[65, 82-84, 98]. Consequently, tumor microenvironmental architecture is characterized by a typical spatial scale between 50 μm and 250 μm. Therefore, the chosen distance of 120 μm between sampling locations ensured that all major spatial features of different aspects of the tumor microenvironment were properly sampled, allowing for a coherent representation of 3D spatial distributions of tracer activity (Figure 21) and viable tissue, as well as any other tumor microenvironmental parameter (e.g. hypoxia, cell proliferation, etc.).

PET simulation

The most accurate approach for creating sPET images would be a Monte Carlo simulation of the PET image formation starting with a 3D autoradiography microscopic tracer uptake map as a heterogeneous source and using readily available models for clinical and research PET scanners. These models allow comprehensive simulations of the physical performance of a particular PET scanner model and generate the raw data that can be used to reconstruct realistic PET image corresponding to any given heterogeneous source of activity. To illustrate the validation methodology, a simplified approach was used in this study. The 3D map of the intratumoral activity distribution, as imaged with autoradiography, was convolved with a 3D Gaussian kernel representative of the point spread function measured in the center of the field of view of the Siemens Inveon small-animal PET scanner. The FWHM size of the adopted convolution kernel was considered appropriate since the reconstructed tumors were generally small (≤1 cm

in largest diameter) and the size of the point spread function was shown to be constant between the center of the field of view and approximately 15 mm radial offset[127, 128] for the scanner in question. For larger tumors tumor specimens, convolution with a spatially variable Gaussian kernel would have to be implemented.

The sPET images are based on 3D stacks of autoradiography data. Therefore, the accuracy of autoradiography in describing the microscopic uptake of the tracer is very important. In this study, ^{14}C-labeled FDG was used to maximize the resolution and to simplify the experimental procedures. The effective resolution for thin tissue autoradiography with this β^- emitter was reported at 100 μm FWHM[129]. When utilizing higher energy positron emitters (e.g. ^{18}F), the resolution of the microscopic tracer uptake map may degrade. However, the estimated resolution for ^{18}F autoradiography (~200-300 μm) would induce an uncertainty in the actual source position that is less than the uncertainty induced by positron travel in PET imaging with a clinical scanner (~1.76 mm)[68].

The obvious effect of convolving/blurring autoradiography activity maps is the dramatic change in spatial heterogeneity of the tracer uptake (Figure 22). As indicated by the overlap analysis between sPET and 3D autoradiography there is little to no overlap between segmented volumes for higher activity values. This result is similar to previous studies illustrating the averaging effects of PET imaging with FDG[69]. Clinical PET imaging resolution (^{18}F and a 80 cm bore scanner) is about 4-5 mm currently and theoretically limited at about 2 mm FWHM because of positron travel and annihilation photon non-colinearity{{}}. The inherent blurring effect introduced only by these physical properties of PET image acquisition will have a profound effect on the spatial

concordance between tracer uptake on PET images and the actual microscopic intratumoral uptake, emphasizing the need for experimental validation of PET imaging for the purpose of radiotherapy image guidance.

Spatial concordance analysis between FDG uptake and viable tissue

Based on the illustration involving the analysis of the co-localization between FDG high uptake regions and the spatial distribution of viable tissue, it was demonstrated that distinct subvolumes indicative of the location of viable tissue can be accurately delineated (Figure 23). For example, if the FDG PET image would be segmented with a 30% of maximum uptake threshold, more than 80% of the viable tissue would be included in the delineated subvolumes. By extending this type of analysis over a population of patients, the delineation uncertainty associated with clinical segmentation protocols can be directly quantified. This would give a clear indication of the efficacy with which biologically targeted radiotherapy can be implemented.

5. Analysis of spatial concordance between the intratumoral patterns of cell proliferation and ^{18}F-fluorothymidine uptake in simulated PET images

5.1 Introduction

The use of PET imaging for biologically guided radiotherapy has been proposed before[8]. There are different approaches to PET image-guided radiotherapy[37, 38]. The clinical feasibility of ^{18}F-FDG PET-based dose escalation has already been demonstrated in clinical trials[20, 22]. Similarly, ^{18}F-FLT PET image data can be potentially utilized to design biologically-adaptive treatments, where subvolumes characterized by active cancer proliferation are targeted with higher doses[35-38].

As reported in previous chapters, there is no current published data demonstrating that the intratumoral pattern of FLT uptake as imaged with PET is representative of the underlying spatial distribution of active cell proliferation. Furthermore, it has been shown that partial volume effect associated with PET imaging can potentially degrade the spatial correspondence between in vivo PET images and the distribution of the targeted biological pathway[69, 70]. In chapter 3, it was demonstrated that subvolumes delineated on high-resolution DAR images may not accurately localize the areas of active cell proliferation[109]. To understand the potential of ^{18}F-FLT PET for guiding radiation therapy and improving the clinical outcomes of patients treated with FLT-based dose escalation, it is necessary to investigate the spatial correspondence between the FLT PET signal and cell proliferation spatial distributions.

In chapter 4 a novel PET imaging histopathological validation method for image-guidance applications was introduced. This method was designed such that it circumvents the difficulties associated with registering in vivo PET images with ex vivo histopathological images. Using the proposed validation methodology, it was demonstrated that while the tracer uptake as seen in sPET image was not as spatially heterogeneous as the actual microscopic uptake map, it still provided valuable spatial information about the topography of the targeted tumor biological aspect. In this chapter, a similar analysis was conducted between a synthetic PET image of FLT uptake and the distribution of cell proliferation markers from a whole small-animal tumor specimen.

5.2 Methods

Tumor model and radiotracer

Human head and neck tumor xenografts (FaDu, SQ20B) were developed in male athymic mice as before. This study presents the analysis for a single SQ20B tumor. The size of the tumor as measured by caliper was 9.2 mm by 7.3 mm by 6.9 mm.

^{14}C-labeled 3'-deoxy-3'-F-fluorothymidine was the investigated tracer. It was synthesized by Moravek Biochemicals, Inc. (Brea, CA), utilizing an established protocol, utilizing 5´-benzoyl-2,3´-anhydrothymidine as a precursor[80, 81]. The specific activity of the compound is 55.7 mCi/ml, and the radiochemical purity is 99.1% as tested with high performance liquid chromatography. The 2'-position on the thymidine ring was labeled with the ^{14}C isotope. The ^{14}C-labelled FLT compound is chemically identical to the previously used ^{18}F-FLT, hence it will be referred to as FLT for the rest of the study

(Figure 24). As in chapter 4, the long-lived isotope was utilized for the autoradiography resolution advantage that the ^{14}C low-energy decay β^- particle offers.

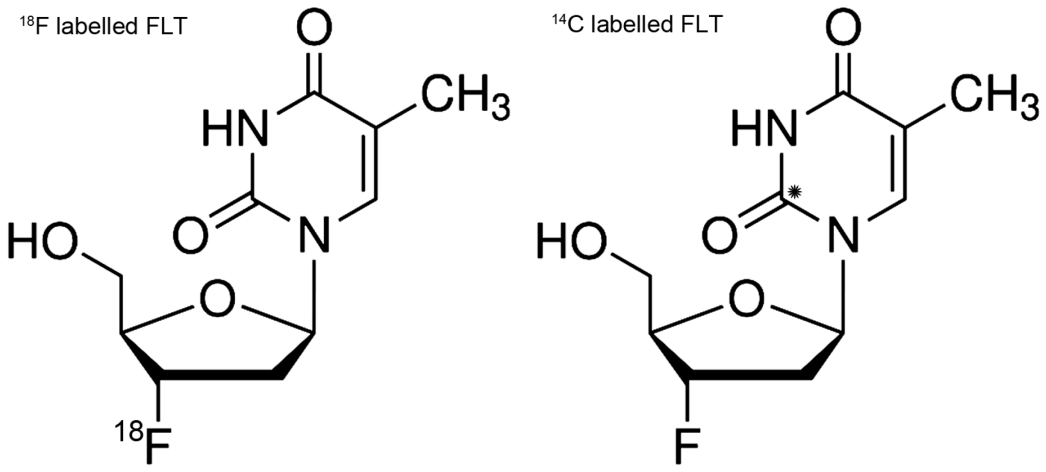

Figure 24. Structural similarity between utilized tracers. Left: tracer tagged with ^{18}F FLT, with the positron emitter on the ribose ring at position 3'. Right: tracer tagged with ^{14}C at position 2' on the thymine ring. A stable fluorine atom was placed at 3' position to maintain the biochemical properties of the tracer.

Experimental procedure

The experimental procedures were replicated as presented in chapter 4. The single difference was that the bolus injection contained Hoechst (0.4 mg/20-g mouse), and at most 1.11 MBq of ^{14}C-FLT. The tissue was embedded utilizing the special freezing jig described in the previous chapter. Tissue histochemical processing and imaging was conducted as presented before[79]. From each sampling location, stacks of four sequential tissue sections (8 μm) were obtained. All sections were imaged for Hoechst staining, images utilized for image registration[79]. One image was used for DAR imaging, while the adjacent sections were utilized to obtain tissue morphology information (H&E staining) and the distribution of active cell proliferation (BrdU uptake) (Figure 25). There were 56 stacks of 4-sections each obtained from the studied tumor.

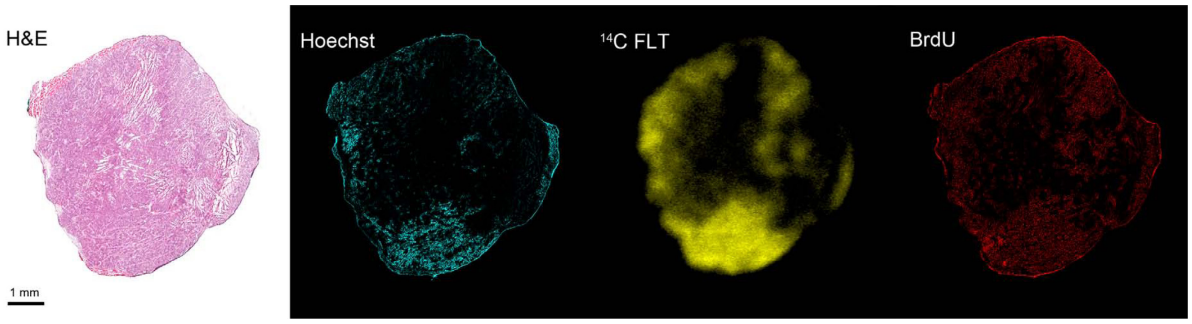

Figure 25. Images obtained from sampling location 45 out of 56. H&E for tissue morphology. Hoechst for blood flow and diffusion. DAR image of ^{14}C FLT distribution. BrdU uptake as a surrogate for active cell proliferation. All images are on the same scale.

As presented before, H&E images were utilized to delineate the extent of the viable tissue as a subset of the entire tissue section[109]. Since there is no a priori information about the location and distribution of viable tissue versus necrosis during in vivo PET imaging, the region of interest for testing spatial concordance in this project was the entire tumor specimen, a union of both viable and non-viable tissue (Figure 26).

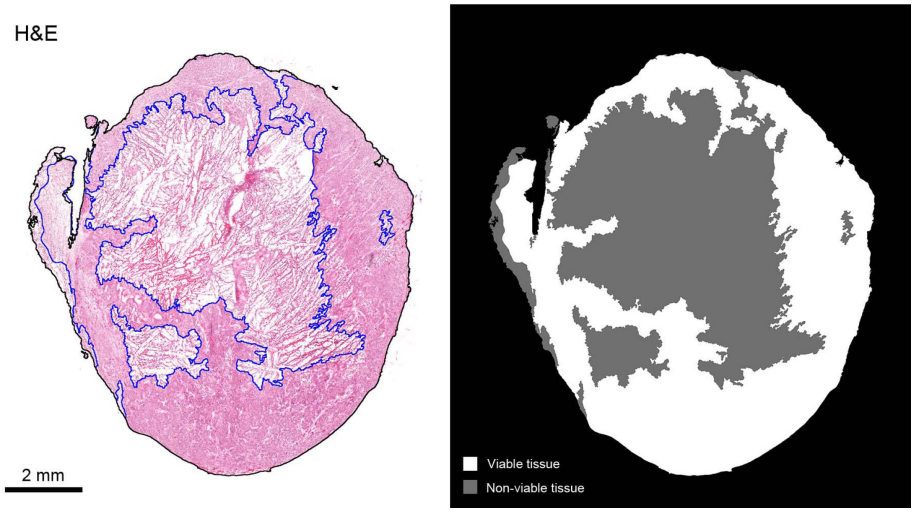

Figure 26. Section 30 out of 56. Left, H&E and superimposed contours for delineated viable tissue (blue) and the outline of the entire tissue section (black). Right, corresponding regions of interest for viable and non-viable tumor tissue. Images are on the same scale.

Based on the available BrdU images, proliferative cell density images were obtained as described in chapter 3. Specifically, the areas of BrdU positive staining were extracted

from the image as a binary mask. The proliferative cell density images were obtained by rebinning these masks to 50 μm per pixel, where the fraction of the Brdu positively stained area in each rebinned pixel was assigned as the new pixel value. To obtain a binary mask of the extent and spatial distribution of cell proliferation, a proliferative cell density threshold value was selected such that the resulting set included the majority of actively proliferative tumor regions. The maximum proliferative cell density in the studied tumor specimen was 40% as defined by the stained area per 50 μm pixel. The threshold that was most sensitive to the extent of cell proliferation as imaged with BrdU was 1%. To present the variation of the results in the presence of more conservative truth sets, 5% and 10% thresholds on proliferative cell density were included in the study (Figure 27).

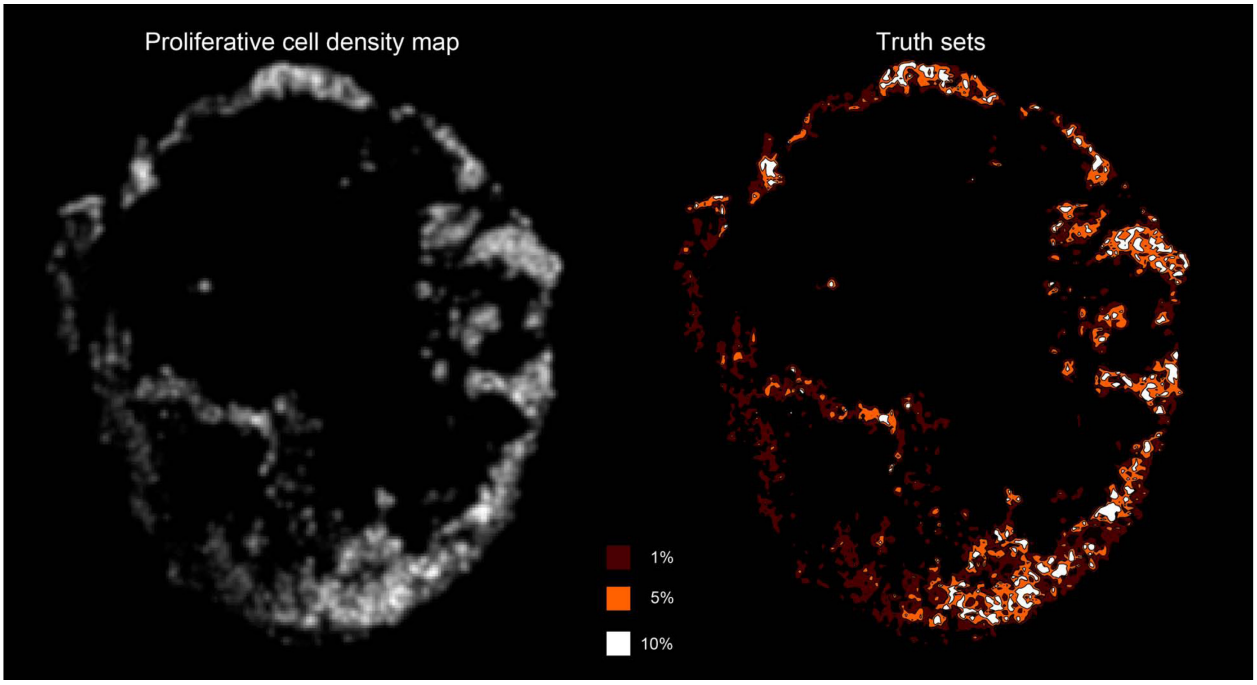

Figure 27. Obtaining truth sets. Left panel: section 30 proliferative cell density grayscale image. Right panel: truth sets based on the proliferative cell density image thresholded at different levels.

3D reconstruction and PET simulation

The three-dimensional reconstruction of the intratumoral FLT uptake was conducted as presented in the previous chapter. Specifically, all registered images from each stack obtained at each sampling location were co-registered to their corresponding digital photos of the tissue in the OCT block (Figure 19).

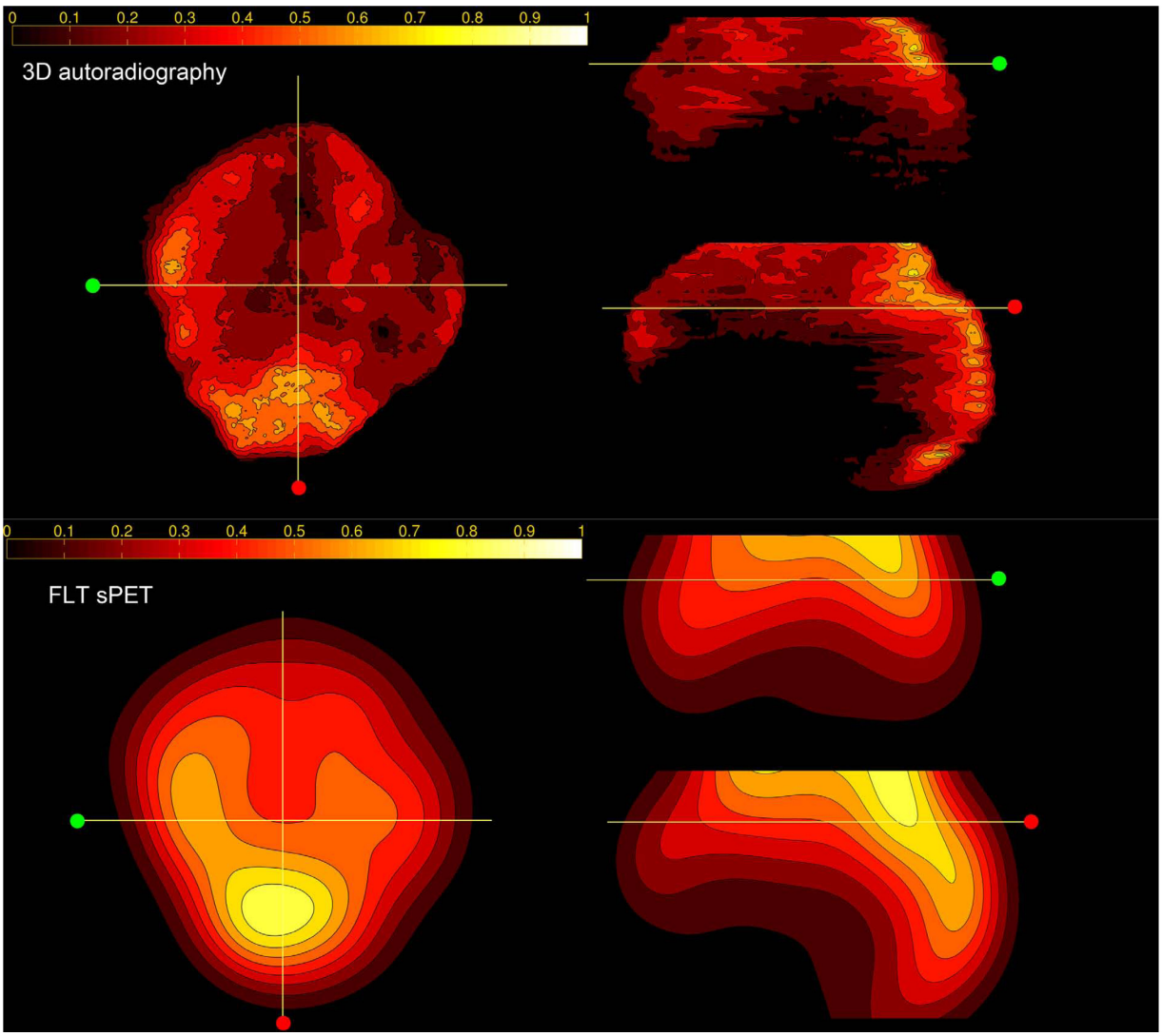

Figure 28. Orthoslices sets. All images were normalized to maximum activity and present values between [0, 1]. All images are at the same scale.

The consistency of the three-dimensional activity pattern of the reconstructed autoradiography stack was evaluated by measuring the normalized intensity correlation

between neighboring slices throughout the tumor volume (mean ± standard deviation = 0.93 ± 0.04). The sPET images were obtained by convolving the 3D stacked autoradiography with a 3D Gaussian kernel representative of the Siemens Inveon small-animal PET scanner spatial resolution (Figure 28). The spatial correspondence between sPET activity map and the original microscopic FLT uptake was evaluated.

Spatial concordance analysis

Threshold-based and threshold-independent metrics of spatial concordance between FLT uptake pattern as seen on the sPET image and the Brdu-defined proliferation truth sets were adapted from the 2D analysis presented in chapter 3 to three-dimensional analysis. To conduct a spatial concordance analysis based on continuous classifiers such as the FLT 3D DAR and sPET images, a binary gold standard needs to be established, which will define the classification truth for each observation in terms of two mutually exclusive classes: actively proliferating tumor versus non-proliferating tumor.

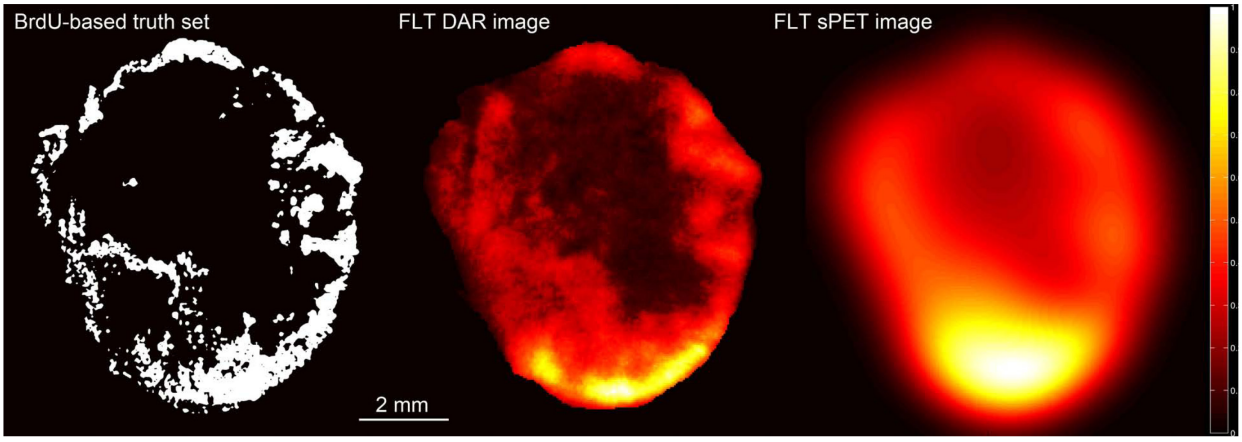

Figure 29. Image set at section 30 level. Left panel: Brdu-based truth set (1% proliferative cell density threshold). Middle panel: autoradiography. Right panel: synthetic PET image. The autoradiography and sPET images were normalized to the maximum value in the 3D volume. All images are on the same scale.

As mentioned before, the gold standard for the extent and spatial distribution of cell proliferation are the BrdU-defined truth sets (Figure 29). Both DAR and sPET images of FLT uptake were thresholded to obtain instances of measurement sets (observations). Varying threshold values were applied to these image sets and the resulting segmentation measurement sets were directly compared to the gold standard. For each observation, i.e. for each threshold level applied to either the 3D DAR or sPET image, a contingency table was created as in chapter 3 (Figure 12). By varying the threshold values over all the available activity levels in the FLT uptake images, the sensitivity and specificity of the classification method could be determined as a function of threshold level [109]. The *ROC* curves were plotted and the area under the curve was measured as presented before. Furthermore, for each instance of the measurement sets, the Dice coefficients were also calculated based on the contingency table metrics. Both *ROC* curve analysis and Dice coefficient curves were plotted for truth sets obtained for 1%, 5%, and 10% proliferation cell density.

Based on the Dice curves a threshold level was established for which the Dice coefficient reached a maximum value, indicating maximum amount of spatial information retrieved by the FLT-based segmentation volume about the truth set shape and extent. For this particular threshold value, the following metrics were computed based on the corresponding contingency table (Figure 12): sensitivity, specificity, accuracy. All these metrics will be discussed in the following sections in terms of the studied classification problem: FLT thresholding classifying actively proliferating or non-proliferative pixels within the volume of interest.

5.3 Results

Correspondence between FLT uptake in 3D autoradiography data and sPET image set

As illustrated by the orthoslices in Figure 28, the convolution process significantly affects the spatial heterogeneity of the FLT uptake. In order to investigate the correspondence between the pattern of FLT uptake as recorded in the 3D autoradiography and sPET, the image sets were normalized to maximum activity and thresholded at different thresholds across the [0, 1] range (Figure 30).

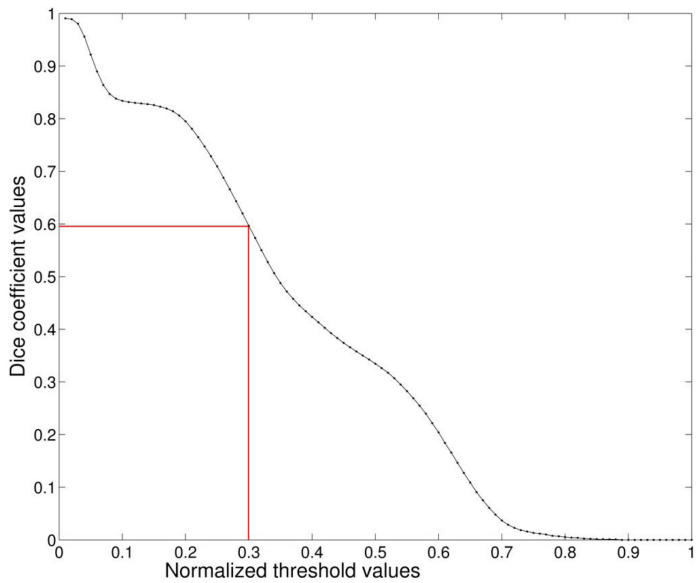

Figure 30. Plot of Dice coefficient values as a function of threshold values applied to normalized FLT uptake (DAR and sPET) images. The red line emphasizes the overlap between DAR and sPET segmentation volumes for 30% of max activity threshold. This threshold produces a sPET segmentation volume that best represents the spatial extent of cell proliferation.

Since the sPET image is inherently registered to the autoradiography set from which it was created, the discrepancies between sPET images and the underlying microscopic uptake of FLT were directly attributed to the finite resolution of PET imaging. While distinct tumor subvolumes can be delineated in both image sets (Figure 31), the

mentioned difference becomes important when regions of high tracer uptake of the tumor are considered for targeting. It is at these conservative threshold values where the overlap between the segmented volumes on FLT and DAR coincide the least (Figure 30), as indicated by Dice coefficient values: 0.037 at 70% of maximum activity, 0.33 at 50%, 0.6 at 30%, and 0.83 at 10%.

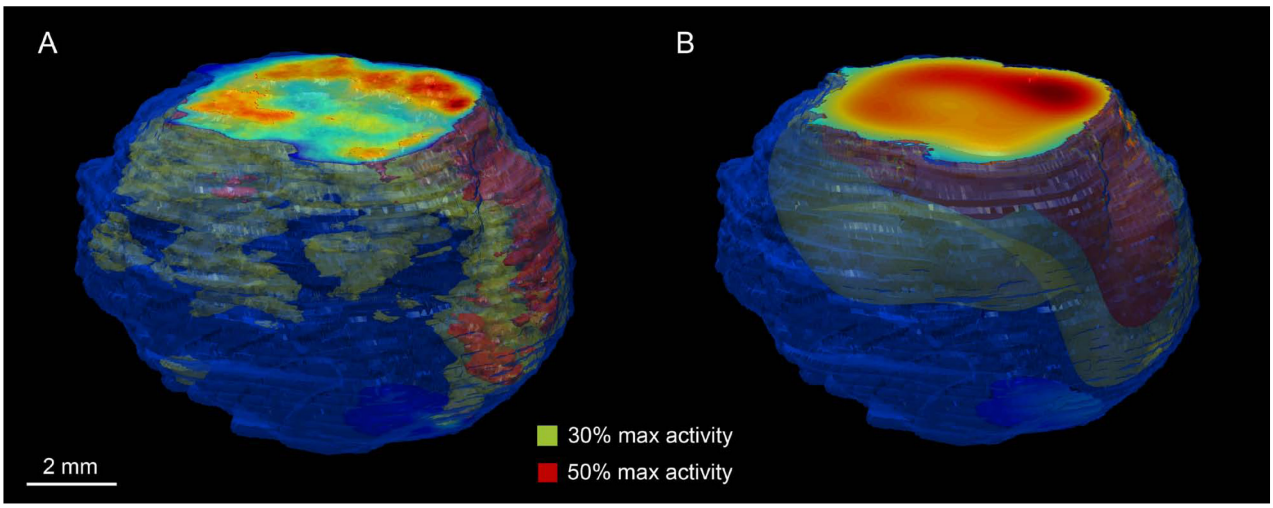

Figure 31. Rendered tissue outline with segmentation volumes. A. 3D reconstructed autoradiography. B. sPET. Threshold values represent percent of maximum intensity. Images are at the same scale.

Spatial concordance analysis between FLT uptake and cell proliferation

The observable loss in spatial heterogeneity of the FLT uptake pattern imaged with sPET vs. the 3D autoradiography was consistent with the *ROC* analysis results. Since the 3D DAR imaging resolution is higher, smaller details of the spatial distribution of cell proliferation could be resolved. Therefore, when thresholding FLT 3D DAR images to retrieve the spatial extent of active cell proliferation, the *AUC* values were higher than when sPET thresholding was utilized (Figure 32). This result was consistent over all the utilized truth sets. The high *AUC* values in both cases are a direct

confirmation that higher uptake values coincide spatially with actively proliferating tumor subvolumes, for both DAR and sPET image sets.

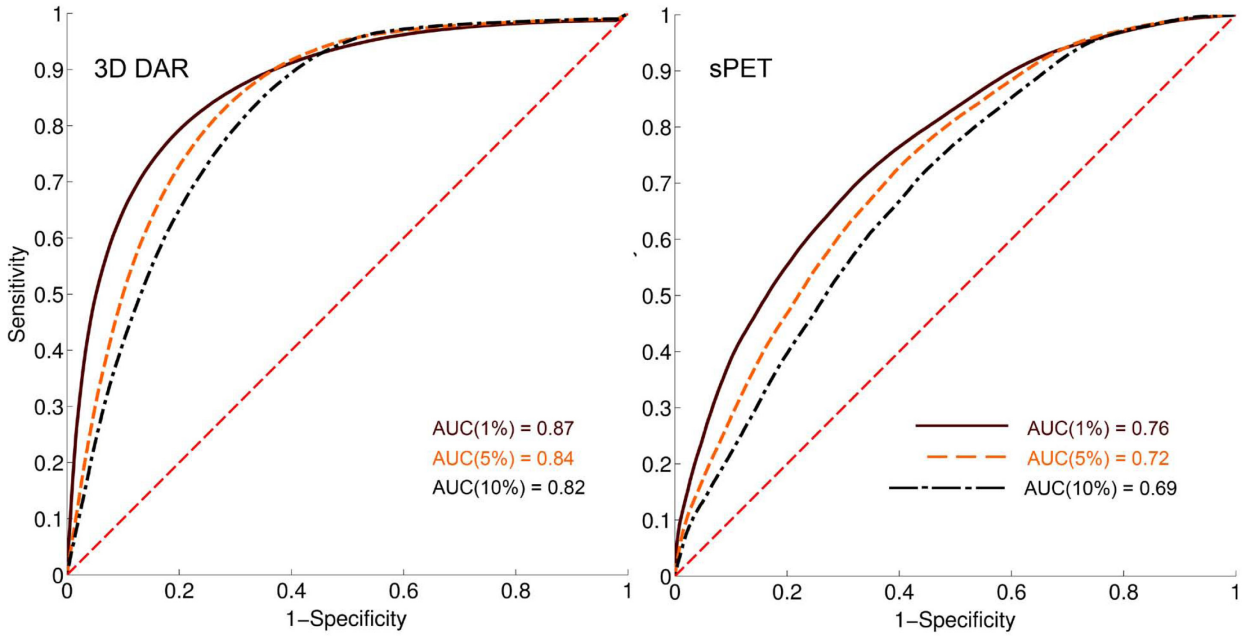

Figure 32. *ROC* analysis of FLT uptake image segmentation as a classifier of the extent and spatial distribution of cell proliferation. Different truth sets were used as gold standard for classification results: 1%, 5%, and 10% proliferative cell density. Red dotted line is indicative of random chance. An *AUC* value closing unity is indicative of perfect sensitivity and specificity of the investigated classification method given a defined truth set.

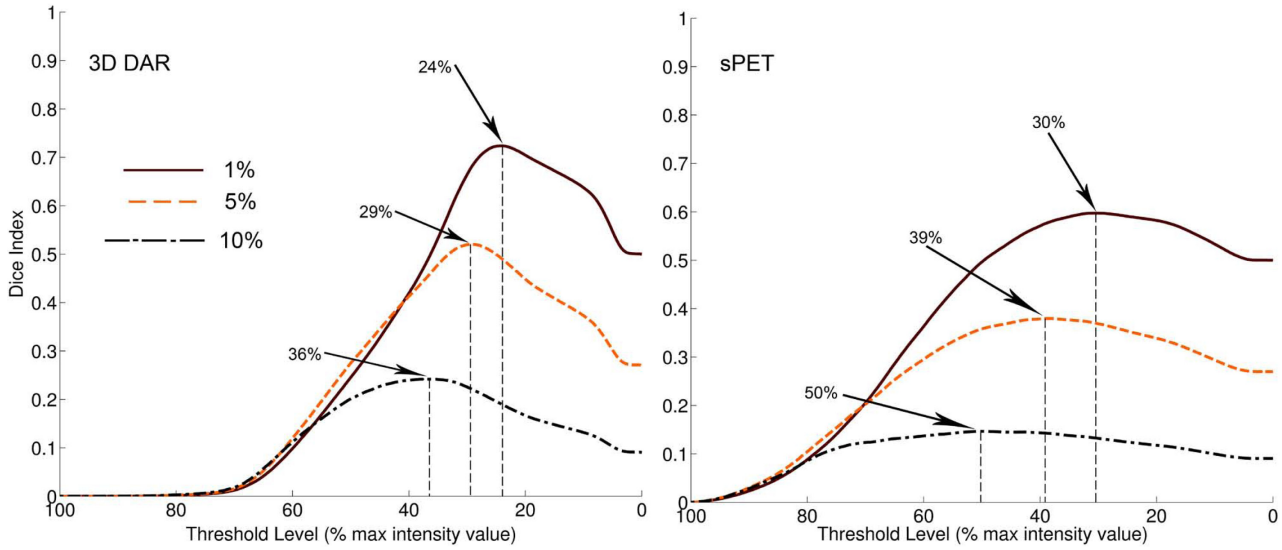

Figure 33. Dice overlap analysis between segmented volumes on FLT uptake images and the BrdU-defined truth set, as a function of utilized FLT threshold value. Different arrows indicate the threshold value for which a maximum Dice coefficient value occurred. Different truth sets were used as gold standard for classification results: 1%, 5%, and 10% proliferative cell density.

The spatial concordance between tumor regions with high FLT uptake and actively proliferative subvolumes was also evident from the Dice analysis. While creating increasingly conservative truth sets, the FLT uptake threshold at which the maximum spatial information about the underlying cell proliferation pattern was retrieved was also increasingly higher (Figure 33), for both DAR and sPET image sets. The values of the maximum Dice coefficients for the 1%, 5%, and 10% were: 0.72, 0.52, and 0.24 for 3D DAR, and 0.6, 0.38, and 0.15 for sPET respectively.

FLT based delineation of actively proliferating subvolumes

As indicated in Figure 33, thresholding the sPET image at 30% of maximum intensity creates a segmentation volume that was most accurate in describing the underlying spatial distribution of cell proliferation for the BrdU-based truth set. The resulting subvolume covered 74% of the truth set obtained with 1% proliferative cell density threshold, presenting good sensitivity to the extent of active cell proliferation.

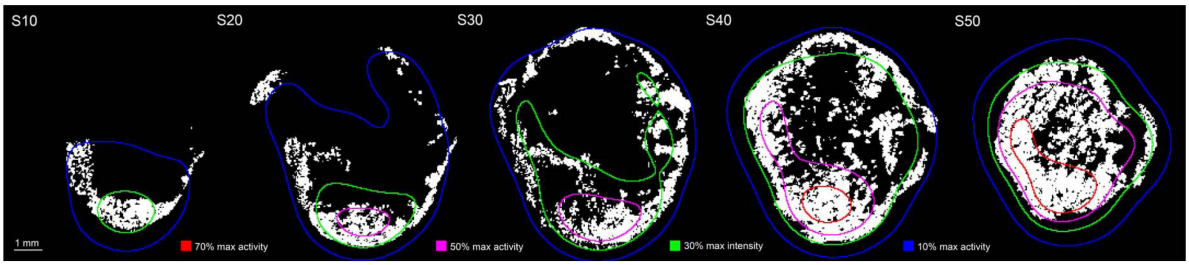

Figure 34. Sequential sections through tumor specimen, presenting BrdU-based truth set obtained with 1% proliferative cell density threshold. The colored lines present activity iso-lines from the sPET image sequence. Thresholds are percent of maximum activity. All images are at the same scale.

The overall specificity with which the delineated subvolume identified positive pixels in the truth set was 0.62, indicating average ability to identify the negative pixels in the

truth set. This aspect was also emphasized by a classification accuracy of 0.66 for the utilized truth set. Figure 34 presents the 1% truth set at different locations throughout the tumor volume. The illustrated overlap between the 30% threshold iso-line and the truth set provides for a visual confirmation of the sensitivity and specificity of the method.

5.4 Discussion

Non-invasive imaging of active cell proliferation has been proposed for radiotherapy guidance. Taking advantage of the biochemical properties of FLT and the long half-life of ^{18}F, PET imaging with this tracer has been receiving a lot of attention for treatment adaptation in biologically guided radiotherapy[37]. Nevertheless, the potential impact of PET imaging resolution limitations may compromise the accuracy of delineating tumor subvolumes that are to be targeted with increased doses. Each image voxel may contain independent regions of active cell proliferation, and an unaccounted combination of necrotic tissue, viable non-proliferating and viable actively proliferating subvolumes (Figure 4).

In this study, the spatial concordance between FLT uptake pattern as imaged with PET and microenvironmental distribution of active cell proliferation was assessed. Synthetic PET images were obtained from the reconstructed microscopic pattern of FLT uptake (Figure 28) as described in chapter 4. The extent and spatial distribution of active cell proliferation were defined based on the uptake of BrdU, an acknowledged exogenous marker of cell proliferation (Figure 27) as described in chapter 3. The two

data sets were accurately co-registered using techniques previously described in this work.

The spatial concordance analysis was conducted on imaging data obtained from tumor xenografts developed in immuno-compromised mice. Since animal tumor models are characterized by growth dynamics, morphology and vascularization different from those encountered in human tumors, the FLT uptake images utilized throughout this validation study are not likely to be representative of the FLT uptake images from human patients. However, this study is not aimed at making inferences about the differences between FLT uptake in animal and human tumors. The animal tumors utilized in this study were characterized by highly heterogeneous microenvironments consisting of a wide range of physiological states. Correspondingly, the FLT uptake pattern of observed in DAR imaging as well as that of BrdU nuclear incorporation observed in IFM imaging from these tumors were spatially heterogeneous (Figure 25). Hence, they were valid experimental platforms for assessing spatial concordance between the two imaging sets. Furthermore, they were perfect tools to develop and optimize PET tracer validation methodologies that may be readily translated to human specimens.

Another important consideration is that there are physiological differences between animal and human tumors that directly affect the absolute levels of FLT intratumoral uptake. The levels of endogenous thymidine are significantly higher in rodents[51-53]. Correspondingly, FLT competes with the serum thymidine for all stages in the cellular incorporation mechanisms. Therefore, it is expected that the FLT uptake is

less than the levels encountered in human tumors. However, these factors do not affect the investigation of spatial characteristics of intratumoral uptake of FLT.

Furthermore, FLT is metabolized in human tumors via glucoronidation (liver metabolism) within 60 minutes post tracer injection. This does not occur in rodents which may influence the absolute uptake levels of FLT in rodents. However, this study aims at analyzing the spatial pattern of FLT entrapment in the studied tumors and its correspondence to the spatial pattern of cell proliferation. Related to the FLT metabolism problem, another potential contention with the presented validation methodology would be that the sPET images are representative of static PET imaging. While it has been shown that kinetic analysis of dynamic FLT PET data is needed in some cases to accurately quantify FLT uptake[53, 130], good agreement has been demonstrated between dynamic PET uptake data and the standard uptake value obtained 45-60 minutes after injection using static PET acquisition[55, 131]. Furthermore, FLT standard uptake value has been shown to be stable between 55 and 100 minutes post injection[132]. These studies suggest that static FLT PET imaging can provide accurate uptake data in a less logistically demanding approach compared to dynamic scanning. Therefore, the synthetic PET images developed from the intratumoral FLT microscopic uptake after 80 minutes of uptake are representative of actual static PET images corresponding to the investigated tumor specimen.

For the single tumor specimen utilized in this study, the microscopic FLT uptake pattern as imaged with 3D DAR is spatially concordant with actively proliferative tumor subvolumes. Furthermore, the macroscopic pattern of FLT uptake imaged with sPET, while significantly different than the 3D DAR pattern, it still provides spatial information

about the underlying spatial distribution of cell proliferation. By expanding the analysis over a larger set of tumor specimens, the delineation uncertainty associated with different segmentation protocols could be quantified and optimal cell-line specific threshold values could be determined to delineate subvolume characterized by active cell proliferation.

Dice coefficient curve analysis presented a distinct feature, consistent over all the utilized truth sets, for both DAR and sPET image sets. The presence of a peak in the Dice coefficient variation over the given thresholds values, a value that was distinct from the all-inclusive minimum threshold, indicated the existence of a specific sPET/DAR threshold value that maximized the number of correctly classified voxels (Figure 33). When introducing more conservative BrdU-defined truth sets (5%, 10%), the Dice peak moved towards higher threshold levels, confirming that areas that contained higher FLT uptake values, also contained more actively proliferating cells. This result is a direct confirmation of the spatial concordance between the pattern of FLT uptake and the spatial distribution of cell proliferation for the specimen used in this illustrative example. The flatter Dice curves recorded for sPET images are a result of the lower resolution of the imaging modality. The large features in the sPET FLT uptake pattern could not accurately resolve all proliferation spatial features (Figure 28). The fraction of incorrectly classified pixels was always greater in the case of the sPET image set due to the mismatch in imaging resolution, affecting the slope of the Dice curve before and after the maximum value. This effect was also evident when more conservative truth sets were utilized within the same imaging modality. Since the same set of segmentation volumes were utilized to determine increasingly more conservative truth sets, a larger

fraction of incorrectly classified pixels were included in the delineated subvolumes, creating a flatter Dice curve and lower values for the maximum.

The high *AUC* values obtained for the single investigated tumor specimen, suggest that segmenting images of FLT uptake is an accurate method of distinguishing between proliferating and non-proliferating voxels, as defined by the BrdU truth sets. In Figure 32, the *ROC* curves and corresponding *AUC* values were presented. While not as high as when the 3D DAR FLT uptake image set was utilized for determination of the extent and spatial distribution of cell proliferation, the sPET *AUC* values were still indicative of a good classification method[105]. As in the Dice analysis, the averaging effect of PET imaging decreased the specificity with which the spatial pattern of active cell proliferation was retrieved, increasing the false positive pixel rate of detection, and decreasing the overall *AUC* value.

The threshold-based analysis for 30% of maximum activity sPET threshold indicated good sensitivity, average specificity, and a resulting mediocre accuracy of FLT sPET segmentation in retrieving the spatial extent and spatial distribution of the given truth. Figure 34 illustrates those aspects, as the 30% iso-line includes some of the truth set at all times, while it does not manage to resolve the disseminated non-proliferating regions. If the tumor subvolume delineated based on the 30% iso-line would be used in biologically adaptive radiotherapy (Figure 2), it would contain the majority of the defined actively proliferating area (74%), while encompassing only 50% of the total delineated tumor volume. Depending on the shape of the resulting subvolume, an escalated dose could be accurately delivered to this subvolume while limiting the surrounding normal tissue exposure[133]. In conclusion, while the tracer uptake as seen in FLT sPET image

was not as spatially heterogeneous as the actual microscopic uptake map, it still provided valuable spatial information about the topography of the targeted biological feature.

6. Conclusions

The dissertation research presented herein was focused on histopathological validation of FLT PET imaging for biologically-guided radiotherapy. Two specific aims were set to reach the thesis goal. First, the spatial concordance between the FLT uptake pattern and the spatial distribution of cell proliferation was analyzed at a microscopic level. The results of the study presented in chapter 3 provided the first set of experimental data validating that in vivo FLT microscopic uptake coincide with areas of active cell proliferation as imaged with conventional immuno-fluorescence methods. In addition, this study emphasized the need for histopathological validation of FLT PET for image-guidance applications since it demonstrated that even high-resolution imaging modalities such as DAR could not consistently and accurately retrieve the extent and spatial distribution of proliferative tumor subvolumes when cell proliferation is highly dispersed throughout the tumor.

The second specific aim of the thesis addressed the development and implementation of new histopathological validation tools to analyze spatial concordance between volumes segmented on FLT simulated PET images and the three dimensional spatial distribution of cell proliferation markers. Since there were no standardized methods applicable towards the goals of this thesis, a novel approach of histopathological validation of PET imaging for image-guidance in radiotherapy was developed and tested in chapter 4. By relying on autoradiography-based simulated PET images generated in such a way as to correctly represent 3D tracer distributions, the validation workflow was reversed, circumventing problems associated with registration of non-invasive in vivo PET images and ex vivo histopathological images. Furthermore,

this methodology was developed with the end-goal of direct translation to validation studies utilizing human tumor specimens, and for any combination of PET tracer vs. targeted tumor biology. Chapter 2 presented a novel multimodality image co-registration workflow that minimized the geometrical misalignments between autoradiography and microscopy images acquired from sequential tissue sections. By utilizing deformable image registration and histopathological images of blood flow as inter-section spatial correspondences, the images acquired from up to four different sequential tissue sections could be presented as if obtained from the same location. The improvement in registration accuracy could further advance correlative studies of the microenvironmental factors governing PET tracer intratumoral distribution as well as the studies aimed at investigation of spatial co-localization of different aspects of tumor biology that can be revealed by combination of autoradiography and/or microscopy imaging.

The research work described here as a whole, was aimed at filling a major gap in data supporting the use of FLT PET for the purpose of imaging the spatial pattern of cancer cell proliferation. While much work remains to be done, the advancements introduced by this thesis will hopefully press forward the research in this aspect of biologically adaptive radiotherapy and open new and improved opportunities for cancer patient care.

7. List of References

1. Vaupel P. Tumor microenvironmental physiology and its implications for radiation oncology. *Semin Radiat Oncol*. 2004;14:198-206.

2. Thomlinson RH, Gray LH. The histological structure of some human lung cancers and the possible implications for radiotherapy. *Br J Cancer*. 1955;9:539-549.

3. Hockel M, Schlenger K, Aral B, Mitze M, Schaffer U, Vaupel P. Association between tumor hypoxia and malignant progression in advanced cancer of the uterine cervix. *Cancer Res*. 1996;56:4509-4515.

4. Weichselbaum RR, Beckett MA, Schwartz JL, Dritschilo A. Radioresistant tumor cells are present in head and neck carcinomas that recur after radiotherapy. *Int J Radiat Oncol Biol Phys*. 1988;15:575-579.

5. Weichselbaum RR, Beckett MA, Vijayakumar S, et al. Radioresistant tumor cell lines derived from head and neck radiation failures. *Head Neck*. 1989;11:343-348.

6. Bentzen S, Atasoy B, Daley F, et al. Epidermal growth factor receptor expression in pretreatment biopsies from head and neck squamous cell carcinoma as a predictive factor for a benefit from accelerated radiation therapy in a randomized controlled trial. *Journal of clinical oncology*. 2005;23:5560-5567.

7. Bentzen S. Theragnostic imaging for radiation oncology: dose-painting by numbers. *Lancet oncology*. 2005;6:112-117.

8. Ling CC, Humm J, Larson S, et al. Towards multidimensional radiotherapy (MD-CRT): biological imaging and biological conformality. *Int J Radiat Oncol Biol Phys*. 2000;47:551-560.

9. Kim Y, Tomé W. Dose-painting IMRT optimization using biological parameters. *Acta Oncol*. 2010;49:1374.

10. Kim Y, Tomé W. Risk-adaptive optimization: selective boosting of high-risk tumor subvolumes. *Int J Radiat Oncol Biol Phys*. 2006;66:1528.

11. Kim Y, Tomé W. Is it beneficial to selectively boost high-risk tumor subvolumes? A comparison of selectively boosting high-risk tumor subvolumes versus homogeneous dose escalation of the entire tumor based on equivalent EUD plans. *Acta Oncol*. 2008;47:906-916.

12. Tomé WA, Fowler JF. Selective boosting of tumor subvolumes. *Int J Radiat Oncol Biol Phys*. 2000;48:593-599.

13. Brahme A. Dosimetric precision requirements in radiation therapy. *Acta radiologica.Oncology*. 1984;23:379-391.

14. Webb S, Nahum AE. A model for calculating tumour control probability in radiotherapy including the effects of inhomogeneous distributions of dose and clonogenic cell density. *Physics in medicine biology*. 1993;38:653-666.

15. Webb S, Evans PM, Swindell W, Deasy JO. A proof that uniform dose gives the greatest TCP for fixed integral dose in the planning target volume. *Physics in medicine biology*. 1994;39:2091-2098.

16. Gonzlez S, Carando D. A general tumour control probability model for non-uniform dose distributions. *Mathematical medicine and biology*. 2008;25:171-184.

17. Stewart R, Li XA. BGRT: biologically guided radiation therapy-the future is fast approaching! *Med Phys*. 2007;34:3739-3751.

18. Duprez F, Bonte K, De Neve W, Boterberg T, De Gersem W, Madani I. Regional relapse after intensity-modulated radiotherapy for head-and-neck cancer. *Int J Radiat Oncol Biol Phys*. 2011;79:450-458.

19. Chao KS, Bosch WR, Mutic S, et al. A novel approach to overcome hypoxic tumor resistance: Cu-ATSM-guided intensity-modulated radiation therapy. *Int J Radiat Oncol Biol Phys*. 2001;49:1171-1182.

20. Madani I, Duthoy W, Derie C, et al. Positron emission tomography-guided, focal-dose escalation using intensity-modulated radiotherapy for head and neck cancer. *Int J Radiat Oncol Biol Phys*. 2007;68:126-135.

21. Troost EGC, Schinagl DAX, Bussink J, et al. Innovations in radiotherapy planning of head and neck cancers: role of PET. *The Journal of Nuclear Medicine*. 2010;51:66.

22. Duprez F, De Neve W, De Gersem W, Coghe M, Madani I. Adaptive dose painting by numbers for head-and-neck cancer. *Int J Radiat Oncol Biol Phys*. 2011;80:1045-1055.

23. Cooper J, Porter K, Mallin K, et al. National Cancer Database report on cancer of the head and neck: 10-year update. *Head Neck*. 2009;31:748-758.

24. Dinshaw KA, Agarwal JP, Ghosh Laskar S, Gupta T, Shrivastava SK. Radical radiotherapy in head and neck squamous cell carcinoma: an analysis of prognostic and therapeutic factors. *Clin Oncol*. 2006;18:383-389.

25. Denis F, Garaud P, Bardet E, et al. Final results of the 94-01 French Head and Neck Oncology and Radiotherapy Group randomized trial comparing radiotherapy alone with concomitant radiochemotherapy in advanced-stage oropharynx carcinoma. *Journal of clinical oncology*. 2004;22:69-76.

26. Nutting C, Morden J, Harrington K, et al. Parotid-sparing intensity modulated versus conventional radiotherapy in head and neck cancer (PARSPORT): a phase 3 multicentre randomised controlled trial. *Lancet oncology*. 2011;12:127-136.

27. Studer G, Luetolf U, Glanzmann C. Locoregional failure analysis in head-and-neck cancer patients treated with IMRT. *Strahlentherapie und Onkologie*. 2007;183:417.

28. Bonner J, Harari P, Giralt J, et al. Radiotherapy plus cetuximab for locoregionally advanced head and neck cancer: 5-year survival data from a phase 3 randomised trial, and relation between cetuximab-induced rash and survival. *Lancet oncology*. 2010;11:21-28.

29. Miah A, Bhide S, Guerrero Urbano MT, et al. Dose-escalated intensity-modulated radiotherapy is feasible and may improve locoregional control and laryngeal preservation in laryngo-hypopharyngeal cancers. *Int J Radiat Oncol Biol Phys*. 2012;82:539-547.

30. Wang J, Li XA. Impact of tumor repopulation on radiotherapy planning. *Int J Radiat Oncol Biol Phys*. 2005;61:220-227.

31. Lauve A, Morris M, Schmidt Ullrich R, et al. Simultaneous integrated boost intensity-modulated radiotherapy for locally advanced head-and-neck squamous cell carcinomas: II--clinical results. *Int J Radiat Oncol Biol Phys*. 2004;60:374.

32. Skladowski K, Maciejewski B, Golen M, et al. Continuous accelerated 7-days-a-week radiotherapy for head-and-neck cancer: long-term results of phase III clinical trial. *Int J Radiat Oncol Biol Phys*. 2006;66:706.

33. Eisbruch A, Ship JA, Dawson LA, et al. Salivary Gland Sparing and Improved Target Irradiation by Conformal and Intensity Modulated Irradiation of Head and Neck Cancer. *World Journal of Surgery.* Springer New York; 2003;27:832-837.

34. Shields A. Positron emission tomography measurement of tumor metabolism and growth: its expanding role in oncology. *Molecular imaging and biology*. 2006;8:141-150.

35. Troost EGC, Bussink J, Hoffmann A, Boerman O, Oyen WJG, Kaanders JHAM. 18F-FLT PET/CT for early response monitoring and dose escalation in oropharyngeal tumors. *The Journal of Nuclear Medicine*. 2010;51:866-874.

36. Daşu A. Treatment planning optimisation based on imaging tumour proliferation and cell density. *Acta Oncol*. 2008;47:1221-1228.

37. Bussink J, van Herpen CML, Kaanders JHAM, Oyen WJG. PET-CT for response assessment and treatment adaptation in head and neck cancer. *Lancet oncology*. 2010;11:661-669.

38. Bussink J, Kaanders JHAM, van der Graaf,Winette T A., Oyen WJG. PET-CT for radiotherapy treatment planning and response monitoring in solid tumors. *Nature Reviews Clinical Oncology*. 2011;8:233-242.

39. Chen J, Mehta RS, Baek H, et al. Clinical characteristics and biomarkers of breast cancer associated with choline concentration measured by 1H MRS. *NMR Biomed*. 2011;24:316-324.

40. Buck A, Herrmann K, Shen C, Dechow T, Schwaiger M, Wester H. Molecular imaging of proliferation in vivo: positron emission tomography with [18F]fluorothymidine. *Methods*. 2009;48:205-215.

41. Shields AF, Grierson JR, Dohmen BM, et al. Imaging proliferation in vivo with [F-18]FLT and positron emission tomography. *Nat Med*. 1998;4:1334-1336.

42. Sherley JL, Kelly TJ. Regulation of human thymidine kinase during the cell cycle. *The Journal of biological chemistry*. 1988;263:8350-8358.

43. Grierson J, Schwartz J, Muzi M, Jordan R, Krohn K. Metabolism of 3'-deoxy-3'-[F-18]fluorothymidine in proliferating A549 cells: validations for positron emission tomography. *Nucl Med Biol*. 2004;31:829-837.

44. Barthel H, Cleij M, Collingridge D, et al. 3'-deoxy-3'-[18F]fluorothymidine as a new marker for monitoring tumor response to antiproliferative therapy in vivo with positron emission tomography. *Cancer Res*. 2003;63:3791-3798.

45. Barthel H, Perumal M, Latigo J, et al. The uptake of 3'-deoxy-3'-[18F]fluorothymidine into L5178Y tumours in vivo is dependent on thymidine kinase 1 protein levels. *European Journal of Nuclear Medicine and Molecular Imaging*. 2005;32:257-263.

46. Troost EGC, Bussink J, Slootweg P, et al. Histopathologic validation of 3'-deoxy-3'-18F-fluorothymidine PET in squamous cell carcinoma of the oral cavity. *The Journal of Nuclear Medicine*. 2010;51:713-719.

47. Brockenbrough JS, Souquet T, Morihara J, et al. Tumor 3'-Deoxy-3'-18F-Fluorothymidine (18F-FLT) Uptake by PET Correlates with Thymidine Kinase 1 Expression: Static and Kinetic Analysis of 18F-FLT PET Studies in Lung Tumors. *The Journal of Nuclear Medicine*. 2011;52:1181-1188.

48. Paproski R, Ng AML, Yao SYM, Graham K, Young J, Cass C. The role of human nucleoside transporters in uptake of 3'-deoxy-3'-fluorothymidine. *Mol Pharmacol*. 2008;74:1372-1380.

49. Paproski R, Wuest M, Jans H, et al. Biodistribution and uptake of 3'-deoxy-3'-fluorothymidine in ENT1-knockout mice and in an ENT1-knockdown tumor model. *The Journal of Nuclear Medicine*. 2010;51:1447-1455.

50. Plotnik D, Emerick L, Krohn K, Unadkat J, Schwartz J. Different modes of transport for 3H-thymidine, 3H-FLT, and 3H-FMAU in proliferating and nonproliferating human tumor cells. *The Journal of Nuclear Medicine*. 2010;51:1464-1471.

51. Nottebrock H, Then R. Thymidine concentrations in serum and urine of different animal species and man. *Biochem Pharmacol*. 1977;26:2175-2179.

52. Zhang C, Yan Z, Li W, et al. [(18)F]FLT-PET imaging does not always "light up" proliferating tumor cells. *Clinical cancer research*. 2012;18:1303-1312.

53. Shields A. PET imaging of tumor growth: not as easy as it looks. *Clinical cancer research*. 2012;18:1189-1191.

54. Muzi M, Spence A, O'Sullivan F, et al. Kinetic analysis of 3'-deoxy-3'-18F-fluorothymidine in patients with gliomas. *The Journal of Nuclear Medicine*. 2006;47:1612-1621.

55. Vesselle H, Grierson J, Muzi M, et al. In vivo validation of 3'deoxy-3'-[(18)F]fluorothymidine ([(18)F]FLT) as a proliferation imaging tracer in humans: correlation of [(18)F]FLT uptake by positron emission tomography with Ki-67 immunohistochemistry and flow cytometry in human lung tumors. *Clinical cancer research*. 2002;8:3315-3323.

56. Kenny L, Vigushin D, Al-Nahhas A, et al. Quantification of cellular proliferation in tumor and normal tissues of patients with breast cancer by [18F]fluorothymidine-positron emission tomography imaging: evaluation of analytical methods. *Cancer Res*. 2005;65:10104-10112.

57. Institute of Medicine (US) Forum on Drug Discovery, Development, and Translation. *Accelerating the Development of Biomarkers for Drug Safety: Workshop Summary.* Washington DC: National Academies Press (US); 2009.

58. Kenny L, Coombes RC, Vigushin D, Al Nahhas A, Shousha S, Aboagye E. Imaging early changes in proliferation at 1 week post chemotherapy: a pilot study in breast cancer patients with 3'-deoxy-3'-[18F]fluorothymidine positron emission tomography. *European journal of nuclear medicine and molecular imaging*. 2007;34:1339-1347.

59. Herrmann K, Wieder H, Buck A, et al. Early response assessment using 3'-deoxy-3'-[18F]fluorothymidine-positron emission tomography in high-grade non-Hodgkin's lymphoma. *Clinical cancer research*. 2007;13:3552-3558.

60. de Langen A, Klabbers B, Lubberink M, et al. Reproducibility of quantitative 18F-3'-deoxy-3'-fluorothymidine measurements using positron emission tomography. *European journal of nuclear medicine and molecular imaging*. 2009;36:389-395.

61. Schiepers C, Dahlbom M, Chen W, et al. Kinetics of 3'-deoxy-3'-18F-fluorothymidine during treatment monitoring of recurrent high-grade glioma. *The Journal of Nuclear Medicine*. 2010;51:720-727.

62. Yap C, Czernin J, Fishbein M, et al. Evaluation of thoracic tumors with 18F-fluorothymidine and 18F-fluorodeoxyglucose-positron emission tomography. *Chest*. 2006;129:393-401.

63. Wagner M, Seitz U, Buck A, et al. 3'-[18F]fluoro-3'-deoxythymidine ([18F]-FLT) as positron emission tomography tracer for imaging proliferation in a murine B-Cell lymphoma model and in the human disease. *Cancer Res*. 2003;63:2681-2687.

64. Francis DL, Freeman A, Visvikis D, et al. In vivo imaging of cellular proliferation in colorectal cancer using positron emission tomography. *Gut*. 2003;52:1602-1606.

65. Konerding MA, Malkusch W, Klapthor B, et al. Evidence for characteristic vascular patterns in solid tumours: quantitative studies using corrosion casts. *Br J Cancer*. 1999;80:724-732.

66. Hanahan D, Weinberg RA. The hallmarks of cancer. *Cell*. 2000;100:57-70.

67. Hanahan D, Weinberg R. Hallmarks of cancer: the next generation. *Cell*. 2011;144:646-674.

68. Levin CS, Hoffman EJ. Calculation of positron range and its effect on the fundamental limit of positron emission tomography system spatial resolution. *Phys Med Biol*. 1999;44:781-799.

69. Christian N, Lee J, Bol A, De Bast M, Jordan B, Grégoire V. The limitation of PET imaging for biological adaptive-IMRT assessed in animal models. *Radiotherapy and oncology*. 2009;91:101-106.

70. Busk M, Horsman M, Overgaard J. Resolution in PET hypoxia imaging: voxel size matters. *Acta Oncol*. 2008;47:1201-1210.

71. Soret M, Bacharach S, Buvat I. Partial-volume effect in PET tumor imaging. *The Journal of Nuclear Medicine*. 2007;48:932-945.

72. Christian N, Lee J, Bol A, De Bast M, Gallez B, Grégoire V. Immobilization device for in vivo and in vitro multimodality image registration of rodent tumors. *Radiotherapy and oncology*. 2008;87:147-151.

73. Humm JL, Ballon D, Hu YC, et al. A stereotactic method for the three-dimensional registration of multi-modality biologic images in animals: NMR, PET, histology, and autoradiography. *Med Phys*. 2003;30:2303-2314.

74. Christian N, Deheneffe S, Bol A, et al. Is (18)F-FDG a surrogate tracer to measure tumor hypoxia? Comparison with the hypoxic tracer (14)C-EF3 in animal tumor models. *Radiotherapy and oncology*. 2010;97:183-188.

75. Pugachev A, Axente M, Humm J. On autoradiographic studies comparing the distributions of ^{18}F- and ^{14}C-labeled compounds in tumor tissue specimens. *Radiotherapy and oncology*. 2010;97:609-609.

76. Carlin S, Pugachev A, Sun X, et al. In vivo characterization of a reporter gene system for imaging hypoxia-induced gene expression. *Nucl Med Biol*. 2009;36:821-831.

77. Pugachev A, Ruan S, Carlin S, et al. Dependence of FDG uptake on tumor microenvironment. *Int J Radiat Oncol Biol Phys*. 2005;62:545-553.

78. Hoeben BAW, Kaanders JHAM, Franssen G, et al. PET of hypoxia with 89Zr-labeled cG250-F(ab')2 in head and neck tumors. *The Journal of Nuclear Medicine*. 2010;51:1076-1083.

79. Axente M, He J, Bass C, et al. Comprehensive approach to coregistration of autoradiography and microscopy images acquired from a set of sequential tissue sections. *The Journal of Nuclear Medicine*. 2011;52:1621-1629.

80. Smyczek-Gargya B, Fersis N, Dittmann H, et al. PET with [18F]fluorothymidine for imaging of primary breast cancer: a pilot study. *European Journal of Nuclear Medicine and Molecular Imaging*. 2004;31:720-724.

81. Machulla H-, Blocher A, Kuntzsch M, Piert M, Wei R, Grierson JR. Simplified Labeling Approach for Synthesizing 3′-Deoxy-3′-[18F]fluorothymidine ([18F]FLT). *Journal of Radioanalytical and Nuclear Chemistry*. 2000;243:843-846.

82. van Laarhoven HWM, Kaanders JHAM, Lok J, et al. Hypoxia in relation to vasculature and proliferation in liver metastases in patients with colorectal cancer. *Int J Radiat Oncol Biol Phys*. 2006;64:473-482.

83. Rijken PF, Bernsen HJ, Peters JP, Hodgkiss RJ, Raleigh JA, van der Kogel AJ. Spatial relationship between hypoxia and the (perfused) vascular network in a human glioma xenograft: a quantitative multi-parameter analysis. *Int J Radiat Oncol Biol Phys*. 2000;48:571-582.

84. Rijken PFJW, Peters JPW, Van der Kogel AJ. Quantitative analysis of varying profiles of hypoxia in relation to functional vessels in different human glioma xenograft lines. *Radiat Res*. 2002;157:626-632.

85. Schlter C, Duchrow M, Wohlenberg C, et al. The cell proliferation-associated antigen of antibody Ki-67: a very large, ubiquitous nuclear protein with numerous repeated elements, representing a new kind of cell cycle-maintaining proteins. *J Cell Biol*. 1993;123:513-522.

86. Gerdes J, Lemke H, Baisch H, Wacker HH, Schwab U, Stein H. Cell cycle analysis of a cell proliferation-associated human nuclear antigen defined by the monoclonal antibody Ki-67. *The journal of immunology*. 1984;133:1710-1715.

87. Muskhelishvili L, Latendresse J, Kodell R, Henderson E. Evaluation of cell proliferation in rat tissues with BrdU, PCNA, Ki-67(MIB-5) immunohistochemistry and in situ hybridization for histone mRNA. *The journal of histochemistry and cytochemistry*. 2003;51:1681-1688.

88. Myronenko A, Song X. Point set registration: coherent point drift. *IEEE Trans Pattern Anal Mach Intell*. 2010;32:2262-2275.

89. McLachlan G. *Mixture Models.* New York, NY: Marcel Dekker; 1988.

90. Arganda-Carreras I, Sorzano COS, Thvenaz P, et al. Non-rigid consistent registration of 2D image sequences. *Phys Med Biol*. 2010;55:6215-6242.

91. Schormann T, Dabringhaus A, Zilles K. Statistics of deformations in histology and application to improved alignment with MRI. *IEEE Trans Med Imaging*. 1995;14:25-35.

92. Brown M, Szeliski R, Winder S. Multi-image matching using multi-scale oriented patches. *Computer Vision and Pattern Recognition, 2005 CVPR 2005 IEEE Computer Society Conference on.* 2005;1:510-517 vol. 1.

93. Sorzano COS, Thévenaz P, Unser M. Elastic registration of biological images using vector-spline regularization. *IEEE Trans Biomed Eng*. 2005;52:652-663.

94. Sieren J, Weydert J, Namati E, et al. A process model for direct correlation between computed tomography and histopathology application in lung cancer. *Acad Radiol*. 2010;17:169.

95. Capek M, Bruza P, Jancek J, Karen P, Kubnov L, Vagnerov R. Volume reconstruction of large tissue specimens from serial physical sections using confocal microscopy and correction of cutting deformations by elastic registration. *Microsc Res Tech*. 2009;72:110.

96. Lowe DG. Distinctive Image Features from Scale-Invariant Keypoints. *International Journal of Computer Vision*. 2004;60:91-110.

97. Flynn AA, Green AJ, Boxer G, Pedley RB, Begent RH. A comparison of image registration techniques for the correlation of radiolabelled antibody distribution with tumour morphology. *Phys Med Biol*. 1999;44:N151-N159.

98. Ljungkvist ASE, Bussink J, Rijken PFJW, Kaanders JHAM, van der Kogel A, Denekamp J. Vascular architecture, hypoxia, and proliferation in first-generation xenografts of human head-and-neck squamous cell carcinomas. *Int J Radiat Oncol Biol Phys*. 2002;54:215-228.

99. Busk M, Horsman M, Jakobsen S, et al. Imaging hypoxia in xenografted and murine tumors with 18F-fluoroazomycin arabinoside: a comparative study involving microPET, autoradiography, PO2-polarography, and fluorescence microscopy. *Int J Radiat Oncol Biol Phys*. 2008;70:1202-1212.

100. Bruechner K, Bergmann R, Santiago A, et al. Comparison of [18F]FDG uptake and distribution with hypoxia and proliferation in FaDu human squamous cell carcinoma (hSCC) xenografts after single dose irradiation. *Int J Radiat Biol*. 2009;85:772-780.

101. Palm C, Vieten A, Salber D, Pietrzyk U. Evaluation of registration strategies for multi-modality images of rat brain slices. *Phys Med Biol*. 2009;54:3269-3289.

102. Noguchi J. Imaging plate characteristics of positron emiters: ^{11}C, ^{13}N, ^{15}O, ^{18}F and ^{38}K. . 2001:437.

103. Strome EM, Jivan S, Doudet DJ. Quantitative in vitro phosphor imaging using [3H] and [18F] radioligands: the effects of chronic desipramine treatment on serotonin 5-HT2 receptors. *J Neurosci Methods*. 2005;141:143-154.

104. Bolte S, Cordelires FP. A guided tour into subcellular colocalization analysis in light microscopy. *J Microsc*. 2006;224:213.

105. Scheipers U, Perrey C, Siebers S, Hansen C, Ermert H. A tutorial on the use of ROC analysis for computer-aided diagnostic systems. *Ultrason Imaging*. 2005;27:181-198.

106. van Erkel AR, Pattynama PM. Receiver operating characteristic (ROC) analysis: basic principles and applications in radiology. *Eur J Radiol*. 1998;27:88.

107. Dice LR. Measures of the Amount of Ecologic Association Between Species. *Ecology*. 1945;26:pp. 297-302.

108. Shattuck D, Prasad G, Mirza M, Narr K, Toga A. Online resource for validation of brain segmentation methods. *Neuroimage*. 2009;45:431-439.

109. Axente M, He J, Bass CP, et al. Tumour microenvironment heterogeneity affects the perceived spatial concordance between the intratumoural patterns of cell proliferation and ^{18}F-fluorothymidine uptake. *Radiotherapy and oncology*. 2012.

110. Otsu N. A Threshold Selection Method from Gray-Level Histograms. *IEEE Transactions on Systems, Man and Cybernetics*. 1979;9:62-66.

111. Du X, Dua S. Segmentation of fluorescence microscopy cell images using unsupervised mining. *The Open Medical Informatics Journal*. 2010;4:41-49.

112. Cabello J. The spatial resolution of silicon-based electron detectors in ???²-autoradiography. *Phys Med Biol*. 2010;55:1677.

113. Salskov A, Tammisetti V, Grierson J, Vesselle H. FLT: measuring tumor cell proliferation in vivo with positron emission tomography and 3'-deoxy-3'-[18F]fluorothymidine. *Semin Nucl Med*. 2007;37:429-439.

114. Frings V, de Langen A, Smit E, et al. Repeatability of metabolically active volume measurements with 18F-FDG and 18F-FLT PET in non-small cell lung cancer. *The Journal of Nuclear Medicine*. 2010;51:1870-1877.

115. Zanzonico P, Campa J, Polycarpe Holman D, et al. Animal-specific positioning molds for registration of repeat imaging studies: comparative microPET imaging of F18-labeled fluoro-deoxyglucose and fluoro-misonidazole in rodent tumors. *Nucl Med Biol*. 2006;33:65-70.

116. Brændengen M, Hansson K, Radu C, Siegbahn A, Jacobsson H, Glimelius B. Delineation of gross tumor volume (GTV) for radiation treatment planning of locally advanced rectal cancer using information from MRI or FDG-PET/CT: a prospective study. *Int J Radiat Oncol Biol Phys*. 2011;81:e439-e445.

117. Caldas Magalhaes J, Kasperts N, Kooij N, et al. Validation of imaging with pathology in laryngeal cancer: accuracy of the registration methodology. *Int J Radiat Oncol Biol Phys*. 2012;82:e289-e298.

118. Yu W, Fu X, Zhang Y, et al. GTV spatial conformity between different delineation methods by 18FDG PET/CT and pathology in esophageal cancer. *Radiotherapy and oncology*. 2009;93:441-446.

119. Devic S, Tomic N, Faria S, Menard S, Lisbona R, Lehnert S. Defining radiotherapy target volumes using 18F-fluoro-deoxy-glucose positron emission tomography/computed tomography: still a Pandora's box? *Int J Radiat Oncol Biol Phys*. 2010;78:1555-1562.

120. Stroom J, Blaauwgeers H, van Baardwijk A, et al. Feasibility of pathology-correlated lung imaging for accurate target definition of lung tumors. *Int J Radiat Oncol Biol Phys*. 2007;69:267-275.

121. Jan S, Santin G, Strul D, et al. GATE: a simulation toolkit for PET and SPECT. *Physics in medicine biology*. 2004;49:4543-4561.

122. Taschereau R, Chatziioannou A. Compressed voxels for high-resolution phantom simulations in GATE. *Molecular imaging and biology*. 2008;10:40-47.

123. Schmidtlein CR, Kirov A, Nehmeh S, et al. Validation of GATE Monte Carlo simulations of the GE Advance/Discovery LS PET scanners. *Med Phys*. 2006;33:198-208.

124. Merheb C, Petegnief Y, Talbot JN. Full modelling of the MOSAIC animal PET system based on the GATE Monte Carlo simulation code. *Phys Med Biol*. 2007;52:563-576.

125. Performance characterization of the Inveon preclinical small-animal PET/SPECT/CT system for multimodality imaging. *European Journal of Nuclear Medicine and Molecular Imaging*. 2010.

126. Marchand EW. Derivation of the Point Spread Function from the Line Spread Function. *J Opt Soc Am*. 1964;54:915-919.

127. Kemp B, Hruska C, McFarland A, Lenox M, Lowe V. NEMA NU 2-2007 performance measurements of the Siemens Inveon preclinical small animal PET system. *Phys Med Biol*. 2009;54:2359-2376.

128. Constantinescu C, Mukherjee J. Performance evaluation of an Inveon PET preclinical scanner. *Phys Med Biol*. 2009;54:2885-2899.

129. Schmidt K, Smith C. Resolution, sensitivity and precision with autoradiography and small animal positron emission tomography: implications for functional brain imaging in animal research. *Nucl Med Biol*. 2005;32:719-725.

130. Spence A, Muzi M, Link J, et al. NCI-sponsored trial for the evaluation of safety and preliminary efficacy of 3'-deoxy-3'-[18F]fluorothymidine (FLT) as a marker of proliferation in patients with recurrent gliomas: preliminary efficacy studies. *Molecular imaging and biology*. 2009;11:343-355.

131. Shields A, Briston D, Chandupatla S, et al. A simplified analysis of [18F]3'-deoxy-3'-fluorothymidine metabolism and retention. *European journal of nuclear medicine and molecular imaging*. 2005;32:1269-1275.

132. Boles Ponto L, Menda Y, Dornfeld K, et al. Stability of 3'-deoxy-3'-[18F]fluorothymidine standardized uptake values in head and neck cancer over time. *Cancer biotherapy radiopharmaceuticals*. 2010;25:361-363.

133. Rødal J, Waldeland E, Sövik A, Malinen E. Dosimetric verification of biologically adapted IMRT. *Med Phys*. 2011;38:2586-2594.

134. Kim JJ, Tannock IF. Repopulation of cancer cells during therapy: an important cause of treatment failure. *Nat Rev Cancer.* 2005;5:516-525.

Vita

Marian Axente was born on January 27th, 1982 in Galați, Romania. He received his Bachelor of Science in 2007 in Physics from the University of Tennessee at Chattanooga. He received his Doctor of Philosophy in Medical Physics from Virginia Commonwealth University in 2012.